US Army Corps of Engineers

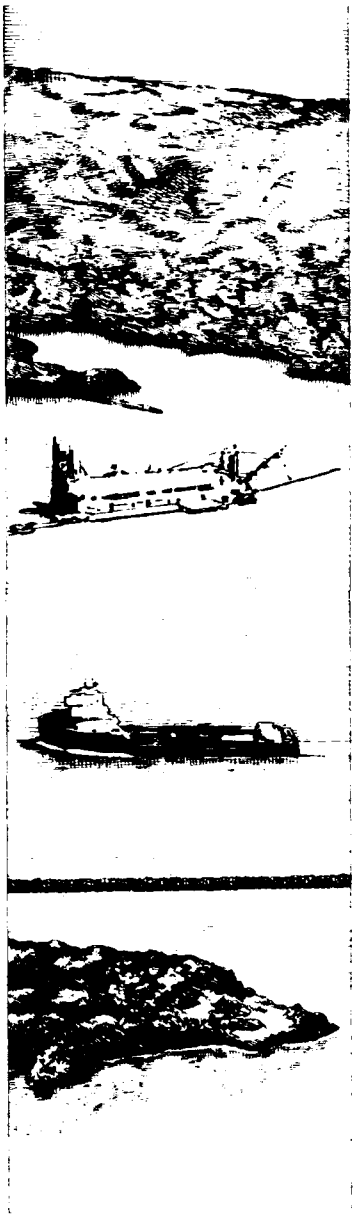

DREDGING RESEARCH PROGRAM

CONTRACT REPORT DRP-91-1

SIMPLE MODELS FOR TURBULENT WAVE-CURRENT BOTTOM BOUNDARY LAYER FLOW

by

Ole Secher Madsen, Palitha Nalin Wikramanayake

Ralph M. Parsons Laboratory
Massachusetts Institute of Technology
Cambridge, Massachusetts 02139

December 1991
Final Report

Prepared for DEPARTMENT OF THE ARMY
US Army Corps of Engineers
Washington, DC 20314-1000

Monitored by Coastal Engineering Research Center
US Army Engineer Waterways Experiment Station
3909 Halls Ferry Road, Vicksburg, Mississippi 39180-6199

Under Work Unit 32463

The Dredging Research Program (DRP) is a seven-year program of the US Army Corps of Engineers. DRP research is managed in these five technical areas:

Area 1 - Analysis of Dredged Material Placed in Open Waters

Area 2 - Material Properties Related to Navigation and Dredging

Area 3 - Dredge Plant Equipment and Systems Processes

Area 4 - Vessel Positioning, Survey Controls, and Dredge Monitoring Systems

Area 5 - Management of Dredging Projects

REPORT DOCUMENTATION PAGE

Form Approved
OMB No. 0704-0188

1. AGENCY USE ONLY (Leave blank)	2. REPORT DATE	3. REPORT TYPE AND DATES COVERED
	December 1991	Final report

4. TITLE AND SUBTITLE
Simple Models for Turbulent Wave-Current Bottom Boundary Layer Flow

5. FUNDING NUMBERS
WU 32463

6. AUTHOR(S)
Ole Secher Madsen
Palitha Nalin Wikramanayake

7. PERFORMING ORGANIZATION NAME(S) AND ADDRESS(ES)
Ralph M. Parsons Laboratory
Massachusetts Institute of Technology
Cambridge, MA 02139

8. PERFORMING ORGANIZATION REPORT NUMBER

9. SPONSORING/MONITORING AGENCY NAME(S) AND ADDRESS(ES)
See reverse

10. SPONSORING/MONITORING AGENCY REPORT NUMBER
Contract Report
DRP-91-1

11. SUPPLEMENTARY NOTES
Available from National Technical Information Service, 5285 Port Royal Road, Springfield, VA 22161

12a. DISTRIBUTION/AVAILABILITY STATEMENT
Approved for public release; distribution is unlimited

12b. DISTRIBUTION CODE

13. ABSTRACT *(Maximum 200 words)*

The application of simple eddy viscosity models to the interaction between the turbulent wave and current boundary layer is studied. A comparison of the results of some recent models from the literature with data from laboratory experiments and numerical models shows that none of these models reproduced the data satisfactorily. An improved model, which did not involve any additional fitting parameters, was developed and found to fit the data well for the case of waves and current in the same direction.

The inability of the improved model to represent some features of the results of higher order turbulence models for the case of waves at an angle to the current was found to be due to the assumption of a time-invariant eddy viscosity. Therefore, a model that allowed the eddy viscosity to vary with time was developed and solved for the case of a weak current. This time-varying model was found to improve the agreement with the numerical model for the case of waves at an angle to the current. Simple, accurate, analytic

(Continued)

14. SUBJECT TERMS		15. NUMBER OF PAGES
Bottom boundary layer Eddy viscosity	Wave-current interaction	158
		16. PRICE CODE

17. SECURITY CLASSIFICATION OF REPORT	18. SECURITY CLASSIFICATION OF THIS PAGE	19. SECURITY CLASSIFICATION OF ABSTRACT	20. LIMITATION OF ABSTRACT
UNCLASSIFIED	UNCLASSIFIED		

9. (Concluded).

US Army Corps of Engineers
Washington, DC 20314-1000

USAE Waterways Experiment Station
Coastal Engineering Research Center
3909 Halls Ferry Road
Vicksburg, MS 39180-6199

13. (Concluded).

approximations were developed that allow the solution of practical problems with this model using no more powerful a tool than a hand calculator.

PREFACE

This study was conducted at the Ralph M. Parsons Laboratory, Department of Civil Engineering (DCE), Massachusetts Institute of Technology, under contract with the Coastal Engineering Research Center (CERC), US Army Engineer Waterways Experiment Station (WES). The work described herein was authorized as part of the Dredging Research Program (DRP), sponsored by Headquarters, US Army Corps of Engineers (HQUSACE), and was performed under Work Unit 32463, "Calculation of Boundary Layer Properties (Non-Cohesive Sediments)." Messrs. Glenn R. Drummond, Rixie J. Hardy, Vince Montante, and John H. Parez are HQUSACE Technical Monitors for the DRP. The HQUSACE Technical Advisors are Messrs. M. K. Miles, Ben I. Kelly, and Don Pommer. Mr. E. Clark McNair, Jr., CERC, is Program Manager (PM) for the DRP, and Dr. Lyndell Z. Hales, CERC, is Assistant PM. Dr. Nicholas C. Kraus, Senior Scientist, CERC, is the Manager of DRP Technical Area 1, "Analysis of Dredged Material Placed in Open Waters."

This study was performed and the report prepared over the period 1 October 1988 through 30 September 1989 by Dr. Ole Secher Madsen, Professor, and Mr. Palitha Nalin Wikramanayake, Research Assistant, both of DCE. Dr. Kraus was Principal Investigator of Work Unit 32463 and provided review of the report. The work was performed under the general supervision of Dr. James R. Houston, Chief, CERC, and Mr. Charles C. Calhoun, Jr., Assistant Chief, CERC, and under the direct supervision of Mr. H. Lee Butler, Chief, Research Division, CERC. Ms. Lee T. Byrne, Information Technology Laboratory, WES, edited the final report.

Commander and Director of WES was COL Larry B. Fulton, EN. Technical Director was Dr. Robert W. Whalin.

For further information on this report or on the Dredging Research Program, please contact Mr. E. Clark McNair, Jr., Program Manager, at (601) 634-2070.

CONTENTS

LIST OF TABLES

LIST OF FIGURES

SUMMARY

The goal of this study was to develop a simple, yet realistic, model of the interaction between the turbulent wave and current boundary layers. Closure of the turbulence problem by an assumed eddy viscosity model was selected in order to permit analytic solution of the governing equations.

A review of previously proposed eddy viscosity models revealed that many of them had not been tested against experimental data. Therefore, three of the more recent models were selected and compared with data from laboratory experiments and the results of a higher order turbulence model. The comparison revealed that the model of Grant and Madsen (1979 and 1986) was the most successful of the existing models. However, the physically unrealistic, discontinuous eddy viscosity used in this model resulted in a poor representation of the velocity at the top of the wave boundary layer. The above deficiency was removed by the development of an improved model, with a continuous eddy viscosity, that resulted in a greatly improved fit to the data. While the new model had a more complicated solution, it used just one fitting parameter, as did all the existing models. However, the new model was unable to represent adequately the effect of a change in the angle between the waves and the current. This drawback was due to the assumption of a time-invariant eddy viscosity made in all the above models.

Therefore, a model that allowed the eddy viscosity to vary in time was developed. The assumption of a weak current relative to the waves was made to simplify the governing equation and an approximate solution obtained for the wave and current velocity profiles. While this model involved much more algebra than before, the solution for the wave problem was found to be very similar to that from the time-invariant model. The solution for the current problem, which involved numerical integration, was simplified by the development of an accurate analytic approximation.

Finally, the concepts of the modified wave friction factor and excursion amplitude were used to develop analytic approximations to the friction factor curves. These simplifications allowed the development of a procedure whereby practical problems could be solved efficiently using no more powerful a tool than a hand calculator.

SIMPLE MODELS FOR TURBULENT WAVE-CURRENT BOTTOM BOUNDARY LAYER FLOW

PART I: INTRODUCTION

Background

1. As periodic waves propagate from deep to shallower waters, they reach a depth beyond which the waves feel the presence of the bottom; i.e., the waves experience finite-depth effects. Conversely, the bottom which generally consists of a movable sediment will from some point on feel the presence of the waves; i.e., the bottom sediments will respond to the agitation associated with the waves.

2. Finite-depth effects on waves—such as shoaling and depth-refraction—are generally considered for water depths less than half the wavelength and are quantified through the use of potential wave theory, i.e., a theory which, among other things, assumes the fluid to be inviscid. While the use of potential wave theory is adequate for the prediction of gross features, such as wave height transformations caused by finite-depth effects, and the detailed local flow structure, e.g., wave orbital velocities, over most of the water depth, it fails in predicting the flow characteristics immediately above the bottom.

3. The reason for the failure of potential wave theory to accurately predict the near-bottom flow characteristics of a wave motion is associated with potential theory's treatment of the fluid as ideal (inviscid). Thus, potential theory allows for (and predicts) a finite slip-velocity to exist immediately above the bottom, whereas a real (viscous) fluid must satisfy a no-slip condition at a solid boundary. To obtain a realistic solution for the flow characteristics in the immediate vicinity of the bottom, it is therefore necessary to account for real fluid effects and impose the no-slip condition on the solution.

4. Because of the oscillatory nature of the near-bottom wave motion, the viscous effect (vorticity) associated with the satisfaction of the no-slip condition has only a limited time, of the order half a wave period, to be transmitted (diffuse) away from the boundary. For this reason, the extent to which viscous, real fluid effects affect a wave motion is limited to a thin layer—the wave boundary layer—immediately above the bottom,

while the motion farther away from the bottom is adequately described by potential wave theory.

5. The existence of a thin wave boundary layer across which the fluid velocity varies from zero (at the boundary) to its free stream value (predicted by potential wave theory) gives rise to a very pronounced velocity gradient, or velocity shear, within the wave boundary layer. Since a high velocity shear within the wave boundary layer is associated with large shear stresses, energy dissipation rates, and turbulence intensities when the flow turns turbulent, it is evident that an ability to quantify any coastal process which directly or indirectly is influenced by near-bottom flow characteristics requires an adequate understanding of and ability to quantify the processes taking place within the wave boundary layer.

Wave-current interaction

6. In the coastal environment, waves and currents are more often than not present at the same time; e.g., local winds produce waves and give rise to wind-induced slowly varying currents, or swell associated with distant storms arrive in shallow waters where they encounter slowly varying tidal currents. Thus, a motion characterized as the combined motion of waves and currents may be considered the most commonly encountered flow condition in near-coastal waters.

7. While the simultaneous presence of waves and currents in coastal waters has been recognized in terms of the effect of currents on waves, i.e., current-refraction, only recently has the potentially important effect of waves on currents been recognized. The physics of the latter wave-current interaction, i.e., the effect of the presence of waves on the characteristics of a slowly varying current, is intimately related to the processes taking place within the wave boundary layer.

8. To more fully appreciate this interaction, consider the near-bottom flow associated with a constant forcing, expressed in terms of a constant shear stress acting on planes parallel to the bottom. For a turbulent shear flow, the shear stress is supported through the vertical mixing of high-velocity fluid from "far above" the bottom and low-velocity fluid from the immediate vicinity of the bottom. The effectiveness of the mixing process depends on the turbulent intensities and the velocity shear, i.e., the scale of the velocity some distance above the bottom. Since the

turbulence intensities immediately above the bottom increase in the presence of a wave motion, at least within the wave boundary layer, a smaller velocity shear is required to support the same shear stress when waves are present than that required in the absence of waves.

9. As a consequence of near-bottom wave-current interaction, the prediction of the near-bottom current velocity profile is sensitive to the presence of waves. Similarly, the bottom resistance experienced by a current of a given magnitude is affected by the presence of waves. In physical terms, the near-bottom wave-current interaction may be interpreted as an apparent increase in bottom roughness experienced by a current in the presence of waves relative to the physical bottom roughness experienced by the same current in the absence of waves.

Wave-sediment interaction

10. For a bottom consisting of a movable sediment, the response of the sediment to the fluid flow above the bottom depends on the forcing, i.e., the bottom shear stress, exerted on the bottom sediments by the flow. Realizing that the vertical scale characteristic for a slowly varying current is of the order of meters while the corresponding scale for a wave motion, the wave boundary layer thickness, is of the order of centimeters, it is evident that the velocity shear and hence the bottom shear stress associated with a given near-bottom wave orbital velocity are far greater than that associated with a current of comparable magnitude. For this reason, waves, rather than currents, dominate fluid-sediment interaction in the coastal environment.

11. While waves feel and respond to the presence of a bottom when the depth is less than about half the wavelength, the bottom does not respond to the presence of a wave motion above until this motion is sufficiently strong, in terms of the bottom shear stress, to mobilize the bottom sediments.

12. Once the critical condition for mobilization of the bottom sediments has been reached or slightly exceeded, an originally flat bottom becomes unstable. In the case of sediments characterized as fine sands and coarser, this instability results in the appearance of bedforms, ripples, on the bottom. For flow conditions exceeding only slightly the critical condition for initiation of sediment movement, the ripples are quite steep, sharp-crested, and essentially two-dimensional features aligned with the

wave crests. As the flow intensity, i.e., the bottom shear stress, is increased, a point is reached when the sharp-crested ripples become rounded, three-dimensional features of smaller steepness. Eventually, the ripples are completely washed out and the bottom is again flat; however, in contrast to flow conditions below critical, a "sheet" of sediment is now moving back and forth above the bottom.

13. From a purely hydrodynamic point of view, the result of wave-sediment interaction in terms of the formation of ripples means that the flow in the immediate vicinity of the bottom must be treated either as a flow over a wavy bottom, including the effect of flow separation over ripple crests, or as a flow over a plane bottom for which a uniform roughness, reproducing the flow resistance of the rippled bottom, is assumed. In either case, the formation of ripples on the bottom significantly complicates the analysis and requires knowledge of the bottom bedform geometry or its equivalent roughness scale.

14. From the point of view of establishing a sediment transport model, it may be argued that an ability to quantify sediment transport mechanics for a pure wave motion is of minor importance. The argument would be that the net sediment transport associated with a linear wave, for which the motion back and forth is completely symmetrical, would consist of equal amounts of sediment being moved back (under the wave trough) and forth (under the wave crest) and therefore result in a vanishing net transport. This argument pinpoints the major problem associated with the prediction of net sediment transport rates in the wave-dominated coastal environment as the prediction of a small difference between two large quantities. Thus, any effect producing an asymmetry in the motion, e.g., wave nonlinearity, wave-induced mass transport, a sloping bottom, or superposition of a current, potentially results in a net sediment transport. In order to establish a model for the mechanics of sediment transport in the coastal environment, it is therefore necessary to first establish a sediment transport model for a pure wave motion.

Wave-current-sediment interaction

15. From the preceding discussions of wave-current and wave-sediment interactions, it is evident that the physical bottom roughness experienced by a combined wave-current flow is a dependent variable in that it depends on the characteristics of predominantly wave-generated bottom bedforms.

Thus, in a purely hydrodynamic sense, wave-current-sediment interaction manifests itself through the production of a physical bottom roughness resulting from bottom sediment response to the near-bottom flow above.

16. From the point of view of sediment transport mechanics in the coastal environment, the presence of waves acts primarily as an agitating agent, which mobilizes the bottom sediment and makes it available for transport by currents superimposed on the waves. Because of the high turbulence intensities within the wave boundary layer, sediment, in particular fine sediments, will be put into suspension and made available for suspension by the turbulence associated with the current outside the wave boundary layer. In this respect, the increased flow resistance experienced by a current in the presence of waves results in an increase in turbulence intensities associated with the current. Thus, waves not only make bottom sediment available for transport by a current but also increase the current's ability to transport through their generation of bottom bedforms, i.e., an increased physical bottom roughness, and through turbulent near-bottom wave-current interaction corresponding to an increased apparent bottom roughness.

17. In addition to the effects of wave-current interaction on turbulent mixing processes and thereby its effect on the vertical distribution of sediment concentration, wave-current interaction also affects the velocity with which the suspended sediment is advected through the wave-current interaction's effect on the current velocity profile. In this respect, the extent of wave-current-sediment interaction—described above as a one-way street in which interaction affects hydrodynamics which, in turn, affects sediment transport—potentially may be further complicated by the suspended sediment producing a vertical density gradient of sufficient strength to necessitate the treatment of the fluid-sediment mixture as a "stratified fluid."

Objective

18. The overall objective of the present research is to develop a comprehensive model of wave-current-sediment interaction consisting of the elements identified and briefly discussed in the subsections of the preceding section.

19. The emphasis is on the development of a model which is internally consistent and based on physically sound principles. In addition, simplicity of model formulation and application is required in its development so long as simplicity does not sacrifice the overall accuracy of the model.

20. The requirement of internal consistency may be illustrated by recognizing that the wave-current interaction model component ultimately is to form the basis for the sediment transport model component. Since the state of the art of sediment transport mechanics unfortunately is far from being regarded as an "exact science," it is therefore not internally consistent to seek an exact solution to the wave-current interaction problem—even if this were possible. Combining this with the requirement of simplicity of application rules out the appropriateness of elaborate, sophisticated numerical models and justifies an emphasis on the development of analytical model components whenever possible.

21. Thus the overall objective of this research is to provide a comprehensive, computationally simple model for rapid solution of sediment transport processes associated with dredging operations, e.g., prediction of the fate of dredged material placed on the sea bottom in disposal operation and infilling rates of dredged navigation channels.

Scope of This Report

22. The scope of this report is to present a simple, yet realistic and accurate model for the calculation of the near-bottom turbulent flow properties associated with the combined action of waves and currents.

23. Following a discussion of the basic physical principles underlying a hydrodynamic model of near-bottom turbulent boundary layer flows (Part II), some previous eddy viscosity models used in these flows are reviewed in Part III. The results of the selected models are compared with available experimental data—both physical and numerical—and their strengths and weaknesses are discussed.

24. An improved model based on a time-invariant eddy viscosity model is presented in Part IV. This model represents an improvement over currently available simple wave-current interaction models in that it removes a physically unrealistic discontinuous eddy viscosity and extends

the model applicability to any reasonable magnitude of the current velocity relative to that of the wave orbital velocity. The former of these improvements should remove some unrealistic features of discontinuous eddy viscosity models when these are applied as the basis for sediment transport calculations. The latter removes the limitation of the current being either weak or strong relative to the wave motion; i.e., it makes the resulting model generally applicable. The results of this model are also compared with the same data used in Part III.

25. In Part V, the lack of physical realism of a time-invariant eddy viscosity applied to the wave-current interaction problem is removed by treating it as time-varying. Despite the added mathematical complexity introduced by this assumption, an approximate analytical solution has been obtained. The wave part of this solution is adequately represented by the solution obtained in Part IV; i.e., the time-invariant eddy viscosity solution of Part IV serves the dual purpose of being an approximate model in its own right and forming part of the improved solution presented in Part V. The significant feature of the time-varying eddy viscosity formulation is a much more pronounced and physically realistic dependency of the current velocity characteristics on the angle between wave and current motion than found in the time-invariant eddy viscosity formulation.

26. In Part VI, a simple procedure is outlined whereby the time-varying model of Part V is applied to calculate the current velocity profile for specified wave and current parameters using a no more powerful tool than a hand calculator. Finally, the result of the wave-current interaction models developed in this report are summarized and discussed in Part VII.

PART II: DERIVATION OF THE GOVERNING EQUATIONS

27. In this chapter, the linearized equation of motion for the bottom boundary layer associated with waves is developed. The specification of the bottom properties by a single equivalent roughness height is discussed along with its use in determining the level of application of the no-slip boundary condition. Various methods of closure for the problem of turbulent flow are discussed. Finally, the assumption of a time-invariant eddy viscosity is used to separate the problem into a wave component and a current component that can be solved for any assumed distribution of the eddy viscosity.

Boundary Layer Approximation

28. The equations governing a two-dimensional flow of an incompressible, homogeneous fluid over a plane boundary may be written

$$\frac{\partial u}{\partial t} + u\frac{\partial u}{\partial x} + w\frac{\partial u}{\partial z} = -\frac{1}{\rho}\frac{\partial p}{\partial x} + \frac{\partial(\tau_{xx}/\rho)}{\partial x} + \frac{\partial(\tau_{zx}/\rho)}{\partial z} \tag{1}$$

$$\frac{\partial w}{\partial t} + u\frac{\partial w}{\partial x} + w\frac{\partial w}{\partial z} = -\frac{1}{\rho}\frac{\partial p}{\partial z} - g + \frac{\partial(\tau_{xz}/\rho)}{\partial x} + \frac{\partial(\tau_{zz}/\rho)}{\partial z} \tag{2}$$

$$\frac{\partial u}{\partial x} + \frac{\partial w}{\partial z} = 0 \tag{3}$$

where

u = the horizontal (x) velocity components

w = the vertical (z) velocity components

ρ = fluid density

p = pressure

g = acceleration due to gravity

$\tau_{ij} = \tau_{ji}$ = turbulent or viscous stresses

29. To simplify this set of equations, an order-of-magnitude analysis is performed in which it is assumed that

$$u = O(U) \quad \text{and} \quad \frac{\tau_{ij}}{\rho} = O(U_*^2) \tag{4}$$

while time and horizontal distances are scaled by the wave motion, $\omega = 2\pi/T$ = radian frequency and $k = 2\pi/L$ = wave number , and the vertical length scale is the wave boundary layer thickness, δ , so that

$$\frac{\partial}{\partial t} = O(\omega) \quad , \quad \frac{\partial}{\partial x} = O(k) \quad , \quad \frac{\partial}{\partial z} = O(1/\delta) \tag{5}$$

30. Introducing these scales in the continuity Equation 3 gives

$$O\left[\frac{\partial u}{\partial x}\right] + O\left[\frac{\partial w}{\partial z}\right] = kU + W/\delta = 0 \tag{6}$$

From Equation 6 the order of magnitude of the vertical velocity

$$W = O(w) = (k\delta)U \ll U \tag{7}$$

is obtained, and its smallness relative to U is a consequence of the boundary layer assumption, $k\delta \ll 1$.

31. Comparison of the orders of magnitude of the nonlinear convective acceleration terms on the left-hand sides of Equations 1 and 2 with the leading linear terms, e.g.,

$$O\left[u\frac{\partial u}{\partial x}\right] = kU^2 \quad ; \quad O\left[\frac{\partial u}{\partial t}\right] = \omega U \tag{8}$$

shows that the order of magnitude of the nonlinear terms relative to the linear terms is given by

$$O\left[\frac{u\partial u/\partial x}{\partial u/\partial t}\right] = \frac{kU}{\omega} = \frac{U}{c} \ll 1 \tag{9}$$

which is identified as the small parameter, U/c , $c = \omega/k$ is the phase velocity of the wave, used in the Stokes expansion of a water-wave problem, e.g., Ippen (1966).

32. Introducing the order-of-magnitude estimates obtained above in the vertical momentum equation, Equation 2, this may be written as

$$\frac{\partial(p/\rho - \tau_{zz}/\rho + gz)}{\partial z} = O(\omega W + kU_*^2) \tag{10}$$

which may be integrated from some level z, within the wave boundary layer, to the outer edge of the wave boundary layer, $z = \delta$ where $p = p_\infty$ and $\tau_{zz} = 0$, to produce an expression

$$\frac{p}{\rho} = \frac{p_\infty}{\rho} + \frac{\tau_{zz}}{\rho} + g(\delta - z) + O[(\omega W + kU_*^2)(\delta - z)] \tag{11}$$

for the pressure within the wave boundary layer.

33. Differentiation of Equation 11 with respect to x, recalling that $\delta \neq \delta(x)$ and $\partial/\partial x = O(k)$, results in

$$\frac{1}{\rho}\frac{\partial p}{\partial x} = \frac{1}{\rho}\frac{\partial(p_\infty + \tau_{zz})}{\partial x} + O[(\omega W + kU_*^2)k\delta] \tag{12}$$

34. Inspection of the last terms in this equation in conjunction with the order-of-magnitude estimate provided by Equation 7 shows that

$$\frac{1}{\rho}\frac{\partial p}{\partial x} = \frac{1}{\rho}\frac{\partial(p_\infty + \tau_{zz})}{\partial x} + O\left[\omega U(k\delta)^2 + \omega U_* \frac{U_*}{c}(k\delta)\right] \tag{13}$$

35. When this expression is introduced in the horizontal momentum equation, its components should be compared with the terms in this equation. This comparison shows that the first term neglected by discarding the last term in Equation 13 is at most of order $(k\delta)^2$ relative to the leading term $\partial u/\partial t = O(\omega U)$ in Equation 1, while the second term is of order $k\delta$ relative to the convective acceleration terms, $u\partial u/\partial x = O[\omega U(U/c)]$, so long as $U_* \leq U$, which may safely be assumed. Thus, a boundary layer approximation to the governing equations is obtained as

$$\frac{\partial u}{\partial t} + u\frac{\partial u}{\partial x} + w\frac{\partial u}{\partial z} = -\frac{1}{\rho}\frac{\partial p_x}{\partial x} + \frac{1}{\rho}\frac{\partial \tau_{xz}}{\partial z} + \frac{1}{\rho}\frac{\partial(\tau_{xx} - \tau_{zz})}{\partial x} \tag{14}$$

with an order of accuracy of $(k\delta)^2$; i.e., the largest terms neglected are of the order $(k\delta)^2$ relative to the leading terms retained.

36. Although the last term in Equation 14 involves the difference between two terms of the same magnitude, cf. Equation 4, this term must be

considered of order kU_*^2 . This, however, is of order $k\delta$ relative to the preceding term, $\partial(\tau_{zx}/\rho)/\partial z = O(U_*^2/\delta)$, so within the accuracy of linear wave theory, i.e., dropping the convective acceleration terms, the *linearized boundary layer approximation* is

$$\frac{\partial u}{\partial t} = -\frac{1}{\rho}\frac{\partial p_\infty}{\partial x} + \frac{\partial(\tau/\rho)}{\partial z} \tag{15}$$

where the subscript notation on the turbulent or viscous stress on horizontal planes has been omitted, since this distinction no longer is necessary.

37. At the outer edge of the wave boundary layer, shear stresses vanish and therefore

$$\frac{\partial u_\infty}{\partial t} = -\frac{1}{\rho}\frac{\partial p_\infty}{\partial x} \tag{16}$$

where the subscript ∞ denotes conditions at the outer edge of the wave boundary layer, $z = \delta$. This equation is identical to the equation governing the near-bottom orbital velocity in linear, potential wave theory, e.g., Ippen (1966)

$$u_\infty = \frac{a\omega}{\sinh(kh)}\cosh(k\delta)\cos(\omega t - kx) \tag{17}$$

where a is wave amplitude and h is water depth. At first, it may appear that the value of δ needs to be specified in order to determine the pressure gradient driving the flow within the wave boundary layer. However, expanding $\cosh(k\delta)$ around $z = 0$ results in

$$\cosh(k\delta) = 1 + \tfrac{1}{2}(k\delta)^2 + \cdots \tag{18}$$

and to the same order of accuracy as the boundary layer approximation itself, recall terms of order $(k\delta)^2$ were neglected in order to obtain Equation 14, it is therefore permissible tc replace $\cosh(k\delta)$ in Equation 16 by unity. Therefore

$$u_\infty = u_b \cos(\omega t - kx) = \frac{a\omega}{\sinh(kh)} \cos(\omega t - kx) \tag{19}$$

is identical to the bottom velocity predicted by linear potential wave theory.

38. Returning to the order-of-magnitude estimates made earlier, the velocity scale for horizontal velocities, U, is identified as u_b, the near-bottom velocity predicted by linear wave theory. Furthermore, in the immediate vicinity of the bottom, the left-hand side of Equation 15 vanishes because of the no-slip condition, and balancing the order of magnitude of the remaining terms shows that

$$\delta = O\left[\frac{U_*^2}{\omega U}\right] \tag{20}$$

or since U_* is at most expected to be of order U, Equation 20 shows that

$$O(k\delta) \simeq O\left[\frac{U}{c}\right] \tag{21}$$

which ensures that the approximations made in the derivation of the linearized boundary layer approximation are internally consistent.

39. Inclusion of a steady current superimposed on the wave motion would have resulted in the same linearized boundary layer approximation of the governing equations provided the current velocity is scaled by $U = u_b$; i.e., so long as the current velocity is not an order of magnitude larger than the wave orbital velocity.

40. The boundary conditions for Equation 15 are the no-slip condition on the bottom and the requirement that the velocity inside the boundary layer u should approach the external velocity u_∞ at the edge of the boundary layer.

41. The no-slip condition is imposed by requiring

$$u = o \quad \text{at} \quad z = z_0 \tag{22}$$

where z_0 reflects the resistance offered by the bed to the flow. The specification of z_0 will be discussed in the next section. The other boundary condition is imposed by requiring

$$u \to u_\infty \qquad \text{as} \qquad z \to \infty \tag{23}$$

42. Here z is taken to be the vertical coordinate scaled by the boundary layer length scale δ. Since the scale is usually much less than the depth of flow this condition constrains the effect of the boundary layer to a small proportion of the depth.

Bottom Boundary Roughness

43. For turbulent flow over a rough surface, the boundary resistance experienced by the flow is produced by form drag (separation and eddy formation) and skin friction (direct shear stress) associated with the flow around individual roughness elements. Thus, the flow in the immediate vicinity of a rough bottom is in principle nonuniform. This condition is true also for a so-called steady uniform turbulent flow over a rough boundary consisting of, say, immobile sand grains, if one takes a "microscopic view" of the flow within a distance of the roughness scale of the boundary. However, farther away from the boundary the eddy motion can no longer be distinguished as associated with a particular roughness element; i.e., it becomes random in nature and may be interpreted as "turbulent" eddies.

44. For distances farther away from the boundary than the physical scale, k_b, of the individual roughness elements, the commonly accepted characteristics of turbulent shear flows apply; i.e., one may expect the mean flow, u, to have a logarithmic profile and be given by (Schlichting 1968)

$$u = \frac{u_*}{\kappa} \ln \frac{z}{z_0} \tag{24}$$

where

$u_* = \sqrt{\tau_b/\rho}$ = shear velocity

τ_b = bottom shear stress

κ = von Karman's constant ($\kappa = 0.4$)

z = height above bottom

z_0 = measure of the boundary roughness

45. For a flow over a plane boundary consisting of uniformly distributed, closely packed immobile sand grains, as in Nikuradse's (1932) extensive experiments, it is natural to choose the boundary roughness scale, k_b, equal to the sand grain diameter, d. In this case, $k_b = k_n = d$ with k_n denoting the equivalent Nikuradse sand grain roughness of the boundary. With this interpretation of k_n, the velocity profile given by Equation 24 holds with

$$z_0 = \begin{cases} k_n/30 & \text{for rough turbulent flow} \quad 70 < \dfrac{u_* k_n}{\nu} \\ (3.3\nu/u_*)/30 & \text{for smooth turbulent flow} \quad \dfrac{u_* k_n}{\nu} < 5 \end{cases} \tag{25}$$

where the generalization to cover smooth turbulent flow—ν denotes the kinematic viscosity of the fluid—has been introduced according to Schlichting (1968).

46. It is important to keep in mind that Equation 24 is valid only for distances, z, from the boundary exceeding the physical scale, k_b, of the boundary roughness. Thus, the prediction of $u = 0$ at $z = z_0$ which follows from Equation 24 is purely formal and obtained by extrapolation from the outer flow region. In fact, even the origin of z is not readily defined for a rough boundary. Fortunately the choice of location of theoretical bed, i.e., $z = 0$, affects the velocity predicted by Equation 24 significantly only for small values of z, where the solution, as pointed out above, merely represents a mathematical continuation of the outer flow.

47. While the physical interpretation of the scale of the physical boundary roughness, k_b, and the equivalent Nikuradse sand grain roughness, k_n, as the sand grain diameter, d, for flow over a plane bottom is a natural one, the situation is considerably more complicated if

the bottom profile is nonplanar, i.e., if it exhibits features that are large in comparison with the small distributed roughness elements considered above. An example of this situation would be a rippled bed as produced by waves propagating over a bottom consisting of movable sediments.

48. The flow around large-scale distributed roughness features contributes to the flow resistance experienced by the fluid above in much the same manner as discussed for the small boundary roughness; i.e., the large-scale bottom features produce form drag as well as skin friction. The only difference is the difference in scales of the roughness elements; e.g., the physical roughness length scale, k_b , is now the ripple height rather than the sand grain diameter. Except for the difference in vertical scale, the turbulent flow over large distributed roughness features may, however, be treated in much the same manner as flow over a plane rough boundary, i.e., with a velocity profile given by Equation 24 and τ_b interpreted as the average flow resistance per unit bottom area resulting from form drag and skin friction. The only difference is that the distance above the bottom above which Equation 24 is valid as well as the uncertainty of assigning a theoretical bottom level, $z = 0$, now are scaled by the physical scale of the bottom features, k_b .

49. The roughness scale influencing the velocity profile, i.e., z_0 or k_n , represents physically the scale of uniformly distributed, closely packed, three-dimensional roughness elements—equivalent sand grains—which placed on a plane boundary and subjected to the same flow as the nonplanar bottom would result in the same flow resistance. Thus, if the bottom features are two-dimensional and oriented perpendicular to the flow, such as ripples, the form drag on this type of bottom feature would be expected to be considerably larger than the form drag on a three-dimensional roughness element. For this reason, it is to be expected that the equivalent Nikuradse sand grain roughness, k_n , corresponding to a rippled bed would be considerably larger than the physical bottom roughness scale, $k_b \simeq$ the ripple height . Thus, Grant and Madsen (1982) suggest $k_n \simeq 4k_b$ for steep ripples.

50. The alternative to the treatment of a nonplanar boundary as a plane, artificially roughened boundary, is to mathematically account for the waviness of the boundary. This approach has been pursued for the case

of a pure wave motion, e.g., Lyne (1971); Sleath (1974, 1976, 1982); Sato, Mimura, and Watanabe (1984); and Shum (1988) based on an assumption of laminar flow; and recently by Sato, Uehara, and Watanabe (1986) using a turbulent closure model. Since the near-bottom flow in the coastal environment is likely to be turbulent rather than laminar and to consist of currents superimposed on waves, these models, which require extensive computations, are not appropriate for the present model development. Consequently, the present study treats the bottom as a plane horizontal bottom of uniform equivalent roughness expressed by k_n or z_0 as introduced in Equations 24 and 25.

Turbulence Models

51. To solve the linearized boundary layer equation, Equation 15, a model relating the shear stress, τ, to the mean flow characteristics, must be introduced.

52. For a laminar flow, this relationship is simply

$$\frac{\tau}{\rho} = \nu\left[\frac{\partial u}{\partial z} + \frac{\partial w}{\partial x}\right] \simeq \nu\frac{\partial u}{\partial z} \tag{26}$$

with ν denoting the kinematic viscosity of the fluid and the term $\partial w/\partial x$ is neglected since it is of order $(k\delta)^2$ relative to $\partial u/\partial z$.

53. For a turbulent flow, the shear stress on horizontal planes is in reality a momentum flux term—the Reynolds stress—which is related to turbulent velocity fluctuations, denoted by primes, through

$$\frac{\tau}{\rho} = -\overline{u'w'} \tag{27}$$

where the overbar indicates a time-averaged quantity and the modeling of this term is far from trivial.

54. For dimensional reasons, the problem of expressing the turbulent Reynold's stress may be recast as the problem of predicting a turbulent eddy viscosity, ν_t, which is defined, by analogy to the kinematic viscosity, through

$$\frac{\tau}{\rho} = -\overline{u'w'} = \nu_t \frac{\partial u}{\partial z} \tag{28}$$

55. Advanced turbulence models consist of separate differential equations from which ν_t is obtained as the product of a length scale—the mixing length—and a velocity scale obtained from the calculation of the turbulent energy. Models of this type have been employed recently by Celik and Rodi (1985); Hagatun and Eidsvik (1986); Justesen (1988); and Davies, Soulsby, and King (1988) for the treatment of wave-current interaction. While these numerical turbulence closure models at present are far too computationally involved and time-consuming to be of practical use as the basis for a general wave-current-sediment interaction model, they serve the purpose of providing excellent and detailed results against which far simpler models may be tested.

56. A simple model for the turbulent Reynolds stress may be obtained using Prandtl's mixing length hypothesis (Schlichting 1968) in which it is assumed that

$$u' = -\ell_u' \frac{\partial u}{\partial z} \qquad \text{and} \qquad w' = \ell_w' \left| \frac{\partial u}{\partial z} \right| \tag{29}$$

so that

$$\frac{\tau}{\rho} = -\overline{u'w'} = \ell^2 \left| \frac{\partial u}{\partial z} \right| \frac{\partial u}{\partial z} \tag{30}$$

with $\ell^2 = \overline{\ell_w' \ell_u'}$ denoting Prandtl's mixing length. From analogy with steady turbulent flow it may be assumed that $\ell = \kappa z$, where κ is von Karman's constant, at least close to the bottom.

57. Bakker (1974) followed by Bakker and van Doorn (1978), and van Kesteren and Bakker (1984) used a mixing length closure formulation, as did Asano and Iwagaki (1986), to obtain solutions to the turbulent wave-current interaction problem. While computationally far less involved than the numerical turbulence closure models mentioned previously, the mixing length models require numerical solution of the governing equations in order to provide results. This requirement limits their usefulness for general

application, although results obtained in this manner may be used for comparison with simpler analytical models.

Eddy viscosity models

58. Rather than assuming u' and w' both to be scaled by the mean velocity gradient, one may assume that $u_* = \sqrt{|\tau_b|/\rho}$, at least very close to the bottom, scales w'. This assumption results in Equation 27 becoming

$$\frac{\tau}{\rho} = -\overline{u'w'} = \ell u_* \frac{\partial u}{\partial z} \tag{31}$$

in which ℓu_* is identical to the turbulent eddy viscosity, ν_t, defined by Equation 28. With ℓ being the mixing length, comparison of Equations 28, 30, and 31 shows that

$$\nu_t = \ell^2 \left| \frac{\partial u}{\partial z} \right| = \ell u_* \tag{32}$$

which is an identity when u is taken as the logarithmic velocity profile given by Equation 24 and $\ell = \kappa z$.

59. The preceding considerations suggest that the turbulent eddy viscosity should vary according to

$$\nu_t = \kappa u_* z \tag{33}$$

with

$$u_* = \sqrt{|\tau_b|/\rho} \tag{34}$$

in the immediate vicinity of the bottom. In this respect, it is of some interest to note that the condition of ν_t varying according to Equation 33 as $z \to 0$ is used as a boundary condition in numerical turbulence closure models.

Use of a time-invariant eddy viscosity

60. Since the problem of the wave boundary layer is unsteady, it would be expected that the eddy viscosity defined by Equation 28 and expressed in terms of a mixing length arguments through Equations 32 and 33 would be a function of time. Thus, if a pure first-order wave motion in considered, the bottom shear stress may be expressed as

$$\tau_b = \tau_{bm}|f(t)|f(t) \tag{35}$$

in which τ_{bm} denotes the maximum bottom shear stress and its temporal variation is formally expressed by $|f(t)|f(t)$ about which it is known only that $|f(t)| = 1$.

61. Introducing Equation 35 in Equations 34 and 33 yields a time-varying eddy viscosity given by

$$\nu_t = \kappa u_{*m} z|f(t)| \tag{36}$$

in which $u_{*m} = \sqrt{\tau_{bm}/\rho}$ is the shear velocity based on the maximum bottom shear stress.

62. All arguments presented so far for the functional form of the turbulent eddy viscosity have invoked assumptions applicable to the immediate vicinity of the bottom, i.e., for $z < z_0^+$. For this region, the linearized governing equation, Equation 15, may be integrated to give

$$\tau - \tau_b = \int_{z_0}^{z} \left[\rho \frac{\partial u}{\partial t} + \frac{\partial p_\infty}{\partial x}\right] dz \simeq 0 \tag{37}$$

or

$$\frac{\tau}{\rho} = \kappa u_{*m} z|f(t)|\frac{\partial u}{\partial z} \simeq \frac{\tau_b}{\rho} = u_{*m}^2|f(t)|f(t) \tag{38}$$

valid for $z < z_0^+$.

63. Equation 38 may be solved, subject to the no-slip condition at $z = z_0$, to give the velocity profile in the immediate vicinity of the boundary

$$u = \frac{u_{*m}}{\kappa} \ln\frac{z}{z_0} f(t) \tag{39}$$

64. The exact same equation for the near-bottom velocity at the time it is maximum, i.e., when $f(t)$ is unity, can be obtained if the time-varying eddy viscosity given by Equation 36 is replaced by a time-invariant eddy viscosity based on the maximum bottom shear stress. In this case

$$\nu_t = \kappa u_{*m} z \tag{40}$$

and the near-bottom velocity

$$u = \frac{u_{*m}}{\kappa} \ln \frac{z}{z_0} \, |f(t)| f(t) \tag{41}$$

is obtained.

65. Comparison of Equations 39 and 41 shows the maximum near-bottom velocity [f(t) = 1] to be independent of whether a time-varying or a time-invariant eddy viscosity is used so long as the time-invariant eddy viscosity is scaled by the shear velocity obtained from the maximum bottom shear stress. While heuristic in nature, the preceding argument serves to support the adoption of a time-invariant eddy viscosity formulation, based on the maximum bottom shear stress, for the solution of unsteady turbulent wave boundary layer flows.

66. The use of a time-invariant eddy viscosity greatly simplifies the computational aspects of the problem. It is shown in the next section how this assumption allows the governing equation to be conveniently separated into a wave component and a current component.

67. Eddy viscosity profiles that are scaled as in Equation 33 by the shear velocity and a length scale have been used to obtain a simple analytic solution for steady turbulent flow problems. Kajiura (1964, 1968) has found that the use of a time-invariant eddy viscosity is sufficient to capture the gross features of the wave boundary layer. For these reasons, this study will be restricted to time-invariant eddy viscosity distributions. The evolution of such models for the wave and wave-current problems is discussed in Part III.

Equations for Waves and Current

68. Using the idea of a turbulent eddy viscosity as defined in Equation 28 in Equation 15, the governing equation can be written as

$$\frac{\partial \vec{u}}{\partial t} = -\frac{1}{\rho} \nabla p + \frac{\partial}{\partial z} \left[\nu_t \frac{\partial \vec{u}}{\partial z} \right] \tag{42}$$

where

$\vec{u}$ = {u,v} = horizontal {x,y} velocity vector

∇ = $\{\partial/\partial x, \partial/\partial y\}$ = horizontal gradient operator

ρ = fluid density

p = pressure

z = height above bottom

69. Separating the variables, $\vec{u}$ and p, into time-invariant (current) and time-varying (wave) components, i.e.,

$$\vec{u} = \vec{u}_c + \vec{u}_w$$
$$p = p_c + p_w \tag{43}$$

it is quite simple, since ν_t is assumed time-invariant, to separate the governing equation into two equations: one governing the waves

$$\frac{\partial \vec{u}_w}{\partial t} = -\frac{1}{\rho}\nabla p_w + \frac{\partial}{\partial z}\left[\nu_t \frac{\partial \vec{u}_w}{\partial z}\right] \tag{44}$$

the other governing the current

$$0 = -\frac{1}{\rho}\nabla p_c + \frac{\partial}{\partial z}\left[\nu_t \frac{\partial \vec{u}_c}{\partial z}\right] \tag{45}$$

Equation governing the waves

70. Without loss of generality, the wave is assumed to propagate in the x-direction so that $\vec{u}_w = u_w$. Furthermore, the wave pressure gradient may be expressed in terms of the near-bottom velocity predicted by linear wave theory as shown in Equation 16, i.e.,

$$\frac{\partial u_\infty}{\partial t} = -\frac{1}{\rho}\frac{\partial p_w}{\partial x} \tag{46}$$

where

$$u_\infty = u_b \cos\omega t = (A_b\omega)\cos\omega t \tag{47}$$

71. Introducing Equation 46 in 44 and making use of the fact that $u_\infty \neq u_\infty(z)$, so that $\partial u_w/\partial z = \partial(u_w - u_\infty)/\partial z$, the equation governing the wave orbital velocity within the wave boundary layer may be written

$$\frac{\partial(u_w - u_\infty)}{\partial t} = \frac{\partial}{\partial z}\left[\nu_t \frac{\partial(u_w - u_\infty)}{\partial z}\right] \tag{48}$$

72. Since this equation is linear and since ν_t is time-invariant, the simple harmonic forcing suggests that the solution of Equation 48 is simple harmonic. It is therefore convenient to employ complex variables and assume

$$\frac{u_w - u_\infty}{u_b} = \mathrm{Re}\{u_d e^{i\omega t}\} \tag{49}$$

where Re{ } denotes that the real part of the complex solution represents the physical solution sought, $i = \sqrt{-1}$, and u_d is a complex function of z .

73. Introducing Equation 49 in 48 and dispensing with the explicit reminder that only the real part of the complex expression makes physical sense leads to the equation governing the orbital velocity within the wave boundary layer for a simple periodic wave

$$\frac{d}{dz}\left[\nu_t \frac{du_d}{dz}\right] - i\omega u_d = 0 \tag{50}$$

74. Since both Equations 44 and 45 are linear, u_c and u_w will both have to satisfy the bottom boundary condition, given by Equation 22, individually. The upper boundary condition for the wave problem will still be as in Equation 23 since the wave boundary layer is expected to be small even in the presence of a current.

Equation governing the current

75. Denoting the magnitude of the current velocity vector by $u_c = |\vec{u}_c| = u_c(z)$ Equation 38 may be written

$$\frac{\partial}{\partial z}\left[\nu_t \frac{du_c}{dz}\right] = \left|\nabla\left[\frac{p_c}{\rho}\right]\right| \tag{51}$$

which may be integrated from the bottom, $z \simeq 0$, where $\nu_t \partial u_c / \partial z = \tau_c / \rho$, to a level z in order to obtain

$$\nu_t \frac{du_c}{dz} = \frac{\tau_c}{\rho} + \left| \nabla \left[\frac{p_c}{\rho} \right] \right| z \tag{52}$$

76. Realizing that the near-bottom flow is limited to a fraction of the total depth, h, over which the average shear stress varies from its maximum value of τ_c to zero, the second term on the right-hand side of Equation 52 is of the order $(z/h) \ll 1$ relative to τ_c / ρ. Thus, the pressure gradient term in Equation 52 may be neglected, and the resulting equation governing the current—often referred to as "the law of the wall" (e.g., Schlichting 1968)—becomes

$$\nu_t \frac{du_c}{dz} = \frac{\tau_c}{\rho} = u_{*c}^2 \tag{53}$$

with $u_{*c} = \sqrt{\tau_c / \rho}$ denoting the shear velocity associated with the current boundary shear stress.

77. Equation 53 is a first-order equation and requires only one boundary condition. The appropriate condition is the no-slip condition, Equation 22, which will give the effect of the boundary on the current flow.

78. Equations 50 and 53 can now be solved for any assumed vertical distribution of the eddy viscosity to give the wave and current velocity profiles. This procedure will be carried out in Parts III and IV.

PART III: REVIEW OF PREVIOUS MODELS

79. In this part, the development of eddy viscosity models scaled by the shear velocity for the wave current problem will be reviewed. Three of the more recent models will be discussed in detail, and the results obtained compared with experimental data.

Development of Eddy Viscosity Models

80. The first application of a turbulent eddy viscosity scaled by the shear velocity to a wave boundary layer was done by Kajiura (1964). He used an eddy viscosity that increased linearly with distance from the bottom analogous to the distribution used successfully to model steady flows. A modification was presented to account for boundary layers in the smooth and intermediate turbulence regimes. Using these models, he obtained graphs for the wave friction factor for various flow regimes that were in good agreement with existing experimental data. In a later publication, Kajiura (1968) proposed a tri-linear form of the eddy viscosity for the wave boundary layer.

81. An important feature of these models—and of most of the succeeding ones—was that the eddy viscosity was considered to be time invariant. This allowed a relatively simple solution to be obtained and, as shown in Part II, makes it possible to separate the wave-current problem into wave and current components making the solution of both more straightforward. Another feature of the 1968 model was that the eddy viscosity was scaled by a shear velocity based on the maximum shear stress rather than a representative "average" value.

82. The first application of this kind of eddy viscosity model to the wave current problem was made by Lundgren (1972). He considered a two-layer model with the flow in the upper layer influenced only by the current eddy viscosity while the flow in the lower layer was affected by the turbulence (and therefore the eddy viscosities) due to both wave and current. The combined eddy viscosity in the lower layer was obtained by the vector sum of the wave and current eddy viscosities which were scaled by their respective shear velocities. The current eddy viscosity was calculated according to the parabolic distribution used in steady open

channel flow while that for the wave was obtained from an empirical expression based on measurements in the pure wave boundary layer made by Jonsson (1963 and 1966). These measurements show that the assumption of a linearly varying eddy viscosity close to the bottom is correct. However, the values decrease exponentially beyond a certain height above the bottom. The current velocity profile was obtained by the numerical integration of the resulting expressions. Here too the wave eddy viscosity was considered time invariant and was scaled by the maximum shear velocity.

83. The later models differ from Lundgren's model in the vertical structure of the eddy viscosity distribution and also by the use of different definitions of the scaling shear velocity. Smith (1977) also proposed a linearly increasing eddy viscosity scaled by the sum of the wave and current shear velocities inside the wave boundary layer. Outside this layer, the current shear velocity was used while keeping the eddy viscosity continuous at the interface. This allowed the current velocity profile to be expressed analytically.

84. The first model that allowed for any angle between the wave and the current and that scaled the eddy viscosity by both the waves and the currents inside the wave boundary layer and the current alone outside the wave boundary layer was that of Grant and Madsen (Grant 1977; Grant and Madsen 1979). Their eddy viscosity was discontinuous at the outer edge of the wave boundary layer, and the solution for the current was sensitive to the definition of this outer edge. Some minor modifications to this model were proposed by Christofferson and Jonsson (1985) while retaining the discontinuity in the eddy viscosity. They also proposed a model with a constant eddy viscosity inside the boundary layer for very rough flows.

85. Further models were proposed by Tanaka and Shuto (1981) and Tanaka, Chian, and Shuto (1983). They used the combined shear velocity to scale the eddy viscosity over the entire depth with a one-layer (1981) and two-layer (1983) vertical structure.

86. In the following sections, three of these models will be presented in some detail and compared with experimental results. The models are a simplified version of the Grant-Madsen model (referred to as the GM model), the model proposed by Smith (1977) (referred to as the SM model), and the model proposed by Tanaka, Chian, and Shuto (1983) (referred to as the TS model). Also described is a higher order numerical turbulence closure

model presented by Davies, Soulsby, and King (1988) which is later used as a source of data to use in comparing the performance of the various simple models.

The Grant-Madsen Model

87. The GM model uses the following time-invariant eddy viscosity variation.

$$\nu_t = \begin{cases} \kappa u_{*cw} & z < \ell \\ \kappa u_{*c} & z > \ell \end{cases} \tag{54}$$

and the boundary layer thickness ℓ was defined by

$$\ell = \frac{\gamma \kappa u_{*cw}}{\omega} \tag{55}$$

where γ is a parameter defining the height of the wave boundary layer. Grant (1977) and Grant and Madsen (1979) suggested a value of 2.0 for γ, while Grant and Madsen (1986) suggested a value between 1.0 and 2.0.

88. In Grant (1977), u_{*c} and u_{*cw} were defined by time averaging the total bottom shear stress and the absolute value of the total shear stress respectively. However, in the definition of the maximum wave shear stress that was used to close the problem, the value of u_{*cw} was based on the maximum total shear stress. In the model presented by Grant and Madsen (1979), a u_{*cw} based on the maximum shear stress was used throughout the derivation.

89. The original GM model assumed a time-invariant eddy viscosity which would result in a sinusoidal variation of the bottom shear stress. For this reason their assumption of the bottom shear stress being proportional to $|\cos(\omega t)|\cos(\omega t)$ is actually inconsistent with their model formulation. This inconsistency was removed in the formulation given in Grant and Madsen (1986) where u_{*c} and u_{*cw} are defined directly from the current bottom shear stress and the maximum bottom shear stress. This was also the formulation given in Wiberg and Smith (1983). The new formulation makes the implementation of the model much less complicated

while giving results that are within 10 percent of the results obtained from the full model. However, the full model did indicate that the reference current velocity within the wave boundary layer was not in the same direction as the mean shear stress. This aspect of the problem is not brought out by any of the time-invariant eddy viscosity models considered in this study, while it is present in higher level turbulence closure models.

90. The combined shear velocity is defined by

$$u_{*cw} = \sqrt{\frac{\tau_m}{\rho}} \tag{56}$$

where τ_m is the maximum wave current bottom shear stress. If τ_w is the maximum wave shear stress, τ_c the average current shear stress and ϕ_{cw} the angle between the wave and the current, τ_m is given by

$$\vec{\tau}_m = (\tau_w + \tau_c\cos\phi_{cw} \ , \quad \tau_c\sin\phi_{cw}) \tag{57}$$

and therefore

$$\begin{aligned} \tau_m &= |\vec{\tau}_m| = (\tau_w^2 + \tau_c^2 + 2\tau_c\tau_w\cos\phi_{cw})^{\frac{1}{2}} \\ &= \tau_{wm}(1 + 2\mu^2\cos\phi_{cw} + \mu^4)^{\frac{1}{4}} \end{aligned} \tag{58}$$

where

$$\mu = \sqrt{\frac{\tau_c}{\tau_w}} = \frac{u_{*c}}{u_{*w}} \tag{59}$$

is a parameter expressing the relative magnitude of the turbulence intensity induced at the bottom by the current and the waves.

Wave problem

91. The equation to be solved is Equation 50. In the GM model, the wave problem is solved by assuming a linearly increasing eddy viscosity for the whole depth. Substituting this variation into Equation 50 gives

$$\frac{d}{dz}\left(\kappa u_{*cw} z \frac{du_d}{dz}\right) - i\omega u_d = 0 \tag{60}$$

92. This equation can be simplified by scaling the vertical coordinate by the boundary layer scale δ and introducing

$$\zeta = \frac{z}{\delta} \tag{61}$$

where

$$\delta = \frac{\kappa u_{*cw}}{\omega} \tag{62}$$

93. Substituting Equations 61 and 62 into Equation 60 leads to

$$\frac{d}{d\zeta}\left[\zeta\frac{du_d}{d\zeta}\right] + i^3 u_d = 0 \tag{63}$$

which is recognized (Hildebrand 1976, p 153) as a special form of the Bessel equation that has a general solution expressed in terms of the Kelvin functions of zeroth order. The solution for u_d in Equation 63 can be written as

$$u_d = A[\mathrm{ker}(2\sqrt{\zeta}) + i\ \mathrm{kei}(2\sqrt{\zeta})] + B[\mathrm{ber}(2\sqrt{\zeta}) + i\ \mathrm{bei}(2\sqrt{\zeta})] \tag{64}$$

where A and B are complex constants to be determined from the boundary conditions. These are given by Equations 22 and 23. Equation 23 is satisfied only if $B = 0$ since the functions ber and bei become exponentially large for large argument (Abramowitz and Stegun 1972, Chapter 9). Equation 22 then results in

$$A[\mathrm{ker}(2\sqrt{\zeta_0}) + i\ \mathrm{kei}(2\sqrt{\zeta_0})] = -1 \tag{65}$$

from which the solution for u_d is obtained as

$$u_d = \frac{-[\mathrm{ker}(2\sqrt{\zeta}) + i\ \mathrm{kei}(2\sqrt{\zeta})]}{\mathrm{ker}(2\sqrt{\zeta_0}) + i\ \mathrm{kei}(2\sqrt{\zeta_0})} \tag{66}$$

94. Recalling the definition of u_d, Equation 49, the solution for the wave velocity u_w is found to be

$$u_w = u_b \mathrm{Re}\left\{\left[1 - \frac{\mathrm{ker}(2\sqrt{\zeta}) + i\ \mathrm{kei}(2\sqrt{\zeta})}{\mathrm{ker}(2\sqrt{\zeta_0}) + i\ \mathrm{kei}(2\sqrt{\zeta_0})}\right] e^{i\omega t}\right\} \tag{67}$$

95. To close the problem, the definition of the maximum wave bottom shear stress is used to write

$$\frac{\tau_w}{\rho} = \max\left\{\left[\nu_t \frac{\partial u_w}{\partial z}\right]_{z=z_0}\right\} \tag{68}$$

which, using the definition of u_d in Equation 49, can be written as

$$\frac{\tau_w}{\rho} = u_{*w}^2 = u_b\left[\frac{\nu_t}{\delta}\left|\frac{\partial u_d}{\partial \zeta}\right|\right]_{z=z_0} \tag{69}$$

96. Substituting for ν_t from Equation 54 gives

$$u_{*w}^2 = \kappa u_{*cw} u_b\left[\zeta\left|\frac{\partial u_d}{\partial \zeta}\right|\right]_{z=z_0} \tag{70}$$

and considering Equation 66 this can be written as

$$u_{*w}^2 = \kappa u_{*cw} u_b \sqrt{\zeta_0}\ \left|A[\mathrm{ker}'(2\sqrt{\zeta_0}) + i\ \mathrm{kei}'(2\sqrt{\zeta_0})]\right| \tag{71}$$

where the primes denote differentiation with respect to the argument of the function and A is given by Equation 65. It is seen from Equations 56 and 58 that if u_{*c} and ϕ_{cw} are known this equation is an implicit equation for u_{*w}.

Current problem

97. The relevant governing equation in this case is Equation 53, where ν_t is given by Equation 54 for the current velocity profile. As stated before, ℓ, the height of the wave boundary layer, is defined by

$$\ell = \gamma\delta \tag{72}$$

where δ is defined in Equation 62. This leaves γ as an unresolved model parameter that can be determined by fitting, e.g., experimental data.

98. For the region $z < \gamma\delta$ the solution to Equation 53 is found as

$$u_c = \frac{u_{*cw}^2}{\kappa u_{*cw}} \ln\left[\frac{z}{z_0}\right] \tag{73}$$

after using the no-slip condition at $z = z_0$.

99. For the region $z > \gamma\delta$, the solution is

$$u_c = \frac{u_{*c}}{\kappa} \ln\left[\frac{z}{\gamma\delta}\right] + c \tag{74}$$

where C is a constant found by requiring the velocity to be continuous at the level ℓ . After matching the velocities, the full solution is

$$u_c = \begin{cases} \dfrac{u_{*c}^2}{\kappa u_{*cw}} \ln\left[\dfrac{z}{z_0}\right] & z < \gamma\delta \\ \dfrac{u_{*c}}{\kappa}\left[\ln\left[\dfrac{z}{\gamma\delta}\right] + \dfrac{u_{*c}}{u_{*cw}} \ln\left[\dfrac{\gamma\delta}{z_0}\right]\right] & z > \gamma\delta \end{cases} \tag{75}$$

Solution of practical problems

100. In the usual application of wave current theory, the wave characteristics u_b and ω are known as is the bottom roughness k_n . The current is specified by a mean shear stress, a mean velocity, or a velocity at a specified height above the bottom. It is generally required to find u_{*w} and u_{*cw} in order to calculate the velocity profile given by Equation 75.

101. Once the model is chosen by specifying a value of γ , an iterative solution procedure must be adopted. This procedure is discussed in detail in Part VI. For the sake of completeness, it is mentioned here that the procedure consists of solving Equations 71 and 75 in succession until the value of u_{*cw} converges.

The Smith Model

102. Smith (1977) proposed an eddy viscosity model as follows:

$$\nu_t = \begin{cases} \kappa(u_{*w} + u_{*c})z & z < \ell \\ \kappa u_{*c}\left[z + \dfrac{\ell u_{*w}}{u_{*c}}\right] & z > \ell \end{cases} \tag{76}$$

103. While the model presented was limited to co-directional waves and currents, an extension to the general case could be made by using the approach of Lundgren (1972). As in the GM model, the wave problem is solved by assuming that the linear eddy viscosity extends over the whole depth. The difference here is that the combined shear velocity is obtained from

$$u_{*cw} = u_{*c} + u_{*w} \tag{77}$$

instead of Equation 56. ℓ is a length scale defined by

$$\ell = \frac{\gamma \kappa u_{*w}}{\omega} \tag{78}$$

104. Smith (1977) originally defined ℓ such that $\gamma = 1$ but as in the GM model of the previous section, γ will be left as a free model parameter. The use of u_{*w} in Equation 78 as compared with u_{*cw} in Equation 62 should be noted.

Wave problem

105. The problem is identical to that in the GM model, and Equation 71 should be used. The only difference is that u_{*cw}, u_{*w}, and u_{*c} are related by Equation 77 instead of by Equation 58.

Current problem

106. The equation to be solved is Equation 53 with ν_t from Equation 76. After solving this equation using the no-slip condition and matching the velocity at $z = \ell$, the current velocity profile is obtained as

$$u_c = \begin{cases} \dfrac{u_{*c}^2}{\kappa u_{*cw}} \ln\left[\dfrac{z}{z_0}\right] & z < \ell \\ \dfrac{u_{*c}}{\kappa} \ln\left[\dfrac{z + \ell/\mu}{z_1}\right] & z > \ell \end{cases} \tag{79}$$

where

$$z_1 = \left[1 + \frac{1}{\mu}\right] \ell \left[\frac{z_0}{\ell}\right]^{\mu/(1+1/\mu)} \tag{80}$$

with μ defined by Equation 59.

107. The solution procedure is the same as that outlined in paragraphs 100 and 101 with the limitation to co-directional waves and currents.

The Tanaka, Chian, and Shuto Model

108. Tanaka, Chiang, and Shuto (1983) proposed the following eddy viscosity profile for both the wave and current problems.

$$\nu_t = \begin{cases} \kappa u_{*cw} & z < d \\ K' \text{Max}\left[\int_0^{z_h} (u_\infty - u)dz\right] = \kappa u_{*cw} d & z > d \end{cases} \tag{81}$$

109. Here K' is a constant taken as 0.016 and u and u_∞ are the horizontal velocities inside, and just outside the boundary layer, respectively. Tanaka, Chian, and Shuto (1983) use the maximum combined velocity at the free surface for u_∞, thus indicating that they considered the current boundary layer as the relevant one for this integral. z_h is the flow depth. u_{*cw} is defined as in the GM model, i.e.,

$$u_{*cw} = \sqrt{\frac{\tau_m}{\rho}} \tag{82}$$

110. This model was presented only for the co-directional case, but extension to the general case could be made using the formulation given in Tanaka and Shuto (1981).

Wave problem

111. As in the wave problem of the GM model the governing equation can be non-dimensionalized by defining ζ and δ by Equations 61 and 62 to give

$$\frac{d}{d\zeta}\left[\zeta \frac{du_d}{d\zeta}\right] + i^3 u_d = 0 \tag{83}$$

for the region $z < d$. For the region $z > d$, the use of the appropriate eddy viscosity from Equation 81 in Equation 60 results in

$$\frac{d^2u_d}{d\zeta} = \frac{iu_d}{\beta} \tag{84}$$

where

$$\beta = \frac{d}{\delta} \tag{85}$$

112. Now Equation 83 is the same as Equation 63; therefore, for $z < d$, we can write

$$u_d = A[\mathrm{ker}(2\sqrt{\zeta}) + i\ \mathrm{kei}(2\sqrt{\zeta})] + B[\mathrm{ker}(2\sqrt{\zeta}) + i\ \mathrm{kei}(2\sqrt{\zeta})] \tag{86}$$

and the solution of Equation 84 gives for $z > d$

$$u_d = Ce^{\sqrt{i/\beta}\zeta} + De^{-\sqrt{i/\beta}\zeta} \tag{87}$$

where A, B, C, and D are complex constants to be determined by the boundary conditions and the requirements that the velocity and its gradient be continuous at $z = d$.

113. Tanaka, Chian, and Shuto use the no-slip condition, i.e., Equation 22, and require

$$\frac{du_d}{dz} = 0 \qquad \text{at} \qquad z = z_h \tag{88}$$

This condition does not appear to be very realistic, but, as will be shown later, is practically the same as the use of Equation 23 for the cases considered.

114. After using the boundary and matching conditions, the following four simultaneous equations are obtained for A, B, C, and D.

$$A[\mathrm{ker}(2\sqrt{\zeta_0}) + i\ \mathrm{kei}(2\sqrt{\zeta_0})] + B[\mathrm{ber}(2\sqrt{\zeta_0}) + i\ \mathrm{bei}(2\sqrt{\zeta_0})] = -1 \tag{89}$$

$$A[\mathrm{ker}(2\sqrt{\beta}) + i\ \mathrm{kei}(2\sqrt{\beta})] + B[\mathrm{ber}(2\sqrt{\beta}) + i\ \mathrm{bei}(2\sqrt{\beta})] = Ce^{\sqrt{i\beta}} + De^{-\sqrt{i\beta}} \tag{90}$$

$$A[\mathrm{ker}'(2\sqrt{\beta}) + i\ \mathrm{kei}'(2\sqrt{\beta})] + B[\mathrm{ber}'(2\sqrt{\beta}) + i\ \mathrm{bei}'(2\sqrt{\beta})] = C\sqrt{i}e^{\sqrt{i\beta}} - D\sqrt{i}e^{-\sqrt{i\beta}} \tag{91}$$

$$Ce^{\sqrt{i/\beta}\zeta_h} - De^{-\sqrt{i/\beta}\zeta_h} = 0 \tag{92}$$

where

$$\zeta_h = \frac{z_h}{\delta} \tag{93}$$

115. It is seen from Equation 92 that if ζ_h is large, i.e., if the flow depth is much greater than the boundary layer scale, C is a very small fraction of D and setting C to zero would produce a negligible change in the solution. This is the same as if Equation 23 had been used as a boundary condition instead of Equation 88. Following the solution for the constants A , B , C , and D , the problem is closed by defining u_{*w} as in the GM model, i.e.,

$$u_{*w}^2 = \kappa u_{*cw} u_b \left[\zeta \left| \frac{\partial u_d}{\partial \zeta} \right| \right]_{z=z_0} \tag{94}$$

and, using Equation 86, results in

$$u_{*w}^2 = \kappa u_{*cw} u_b \sqrt{\zeta_0} \left| A[\text{ker}'(2\sqrt{\zeta_0}) + i\ \text{kei}'(2\sqrt{\zeta_0})] + B[\text{ber}'(2\sqrt{\zeta_0}) + i\ \text{bei}'(2\sqrt{\zeta_0})] \right| \tag{95}$$

which is an implicit equation for u_{*w}.

Current problem

116. Again, a solution to Equation 53 with ν_t from Equation 81 in this case is needed. However, for the region $z > d$, Tanaka, Chian, and Shuto use a linear decrease of the mean shear stress to zero at the free surface. This decrease results in the equation

$$\nu_t \frac{du_c}{dz} = u_{*c}^2 \left[1 - \frac{z}{z_h} \right] \tag{96}$$

for the region $z > d$. Solving Equations 53 and 96 and matching the velocity at $z = d$, the current velocity profile is obtained as

$$u_c = \begin{cases} \dfrac{u_{*c}^2}{\kappa u_{*cw}} \ln\left[\dfrac{z}{z_0}\right} & z < d \\ \dfrac{u_{*c}^2}{\kappa u_{*cw}} \left[\dfrac{1}{d}\left(z - \dfrac{z^2}{2z_h} \right) + \ln\left[\dfrac{d}{z_0}\right] - 1 + \dfrac{d}{2z_h} \right] & z > d \end{cases} \tag{97}$$

Determination of d

117. So far the value of d has not been given explicitly in terms of the other quantities, but only as the integral in Equation 81. Tanaka, Chian, and Shuto evaluate this integral by assuming that u_∞ is the combined wave and current velocity at the free surface and that d is much greater than z_0. The result is a cubic equation for d which can be expressed in the present notation as

$$s = \frac{K'}{\kappa^2}\left[\left[\frac{s}{2} + \frac{s^2}{3} + \frac{1}{6s}\right]\frac{u_{*c}^2}{u_{*cw}^2} + \frac{\delta u_{*w}^2}{z_h u_{*cw}^2}\right] \tag{98}$$

where

$$s = \frac{d}{z_h} \tag{99}$$

and δ is defined in Equation 62.

118. Therefore in the iterative solution procedure, d is also continually updated by the use of Equation 98.

Numerical Turbulence Model of Davies, Soulsby, and King

119. As mentioned in Part II, solution of the governing equation (Equation 15) requires a definition of the shear stress term on the right-hand side. In turbulent flow, this term is actually a momentum flux term known as the Reynolds stress and is defined by Equation 27. The problem of expressing this stress in terms of the mean flow variables is known as the turbulence closure problem.

120. The simplest way of doing this is by defining an eddy viscosity as in Equation 28 and then prescribing the variation of this quantity in time and space. This is the method used in the simple models considered in this study. These models are known as zero equation models and have the drawback of being able to predict only the gross flow properties.

121. The next step up in complexity is to define the eddy viscosity as the multiple of a velocity scale and a length scale ℓ. The velocity scale is taken to be the square root of k —the average turbulent kinetic energy. An equation for k is then derived in terms of the mean flow variables with the turbulent energy dissipation ϵ expressed in terms of k and ℓ. The problem is closed by specifying the variation of the length

scale. These are known as one-equation models and, in common with the simpler mixing length models described in Part II, have the disadvantage that the variation of ℓ must be assumed. A further refinement is then to derive an equation for either ϵ or the mixing length ℓ. This results in a two-equation model which has been used successfully for two-dimensional flows.

122. The numerical model used by Davies, Soulsby, and King (1988) is of the latter kind with equations for k and ℓ in addition to the equations for the velocity. The boundary conditions used for the k equation are those of zero energy flux at the bottom and the free surface while the condition on ℓ is that it approaches the value κz_0 as z approaches z_0. It can be shown, however, from the k equation and its boundary condition that very near the bottom k is proportional to the square of the shear velocity. Taking this in conjunction with the boundary condition on ℓ and the definition of the eddy viscosity means that the eddy viscosity is constrained to approach a value proportional to $u_* z_0$ as z approaches z_0. In other words the eddy viscosity will vary linearly very close to z_0.

123. This shows that the vertical variation of the eddy viscosity used in this model is of the same form as that used in all the simple models very close to the bed. The reasoning behind the use of the linearly varying eddy viscosity throughout the depth in the GM model is that the variation close to the bed is the controlling factor in determining the shear stress rather than the variation away from the bed. If this is the case, the predicted shear stresses from both models should be similar.

124. However, the numerical model allows for a time-varying eddy viscosity that is obtained with greater sophistication than in the simple models. For this reason, the velocity profiles, etc., obtained from the numerical model are considered to represent accurate solutions to the governing equations and provide a good data set for comparison with the results of the simple models.

125. In the implementation of the model, the steady current is generated first by imposing an oscillating pressure gradient of tidal frequency. After the initial transients have died away, this is replaced by a steady pressure gradient and the solution run on until a steady state is reached. Then the waves are applied by imposing an oscillating pressure

gradient at the wave frequency such that the required wave motion is obtained after the solution has converged. This condition corresponds in nature to the driving force behind the current remaining unchanged before and after the waves. Therefore, the depth-averaged current velocity will change after the wave motion is imposed.

Experimental Data

126. Many of the models discussed so far have been presented only as theories with no comparison of results with experimental data. An exception is the TS model which was compared with experimental data obtained by Tanaka, Chian, and Shuto (1983) from a wind tunnel. This experiment will be discussed along with the comparison of the TS model to the selected data. One reason for the lack of comparisons has been the paucity of good experimental data from unsteady turbulent boundary layers, particularly for the wave-current interaction problem.

127. The data available for comparison are of two kinds—physical and numerical. Physical data are those measured from the laboratory and field. They are more meaningful in that they are from the real world where all models must ultimately be applied, but their disadvantage is that the conditions during the measurement may not correspond to those assumed in developing the theory.

128. Numerical data are obtained by solving the same governing equations numerically using sophisticated higher order turbulence closure models. The conditions assumed are similar to those used for the present theories; therefore, they provide a good test of the performance of the simple eddy viscosity closure models in simulating the "exact" numerical solutions. Furthermore, the numerical models may be able to simulate conditions that are very difficult to obtain in the laboratory. A good example of this is the case of waves and a current at an angle. This condition cannot easily be realised in an ordinary wave flume.

Physical data

129. The wave-current models presented here should, in the limit of a vanishingly small current, be able to predict the velocity profile under a pure wave motion. Therefore, three sets of data from wave boundary layers are chosen for comparison. They are the data sets from Tests 1 and 2 of

Jonsson and Carlsen (1976)—named JC1 and JC2 for convenience—and the data set from Van Doorn (1981) which is referred to as VDW.

130. Jonsson and Carlsen measured velocities in the turbulent oscillatory flow near a fixed bed with two-dimensional artificial roughness elements. The experiments were performed in an oscillating water tunnel, and the velocities were measured at various heights above a trough in the bottom roughness by a micro-propeller. The measurements were phase averaged over many cycles and then smoothed in both z and t. The details of the smoothing were not given.

131. The experimental parameters needed to run the theoretical models are given in Table 1. Jonsson and Carlsen calculated values of k_n, the equivalent Nikuradse roughness, and Δ, the displacement of the theoretical bed below the top of the roughness elements. However, the values given in Table 1 are those obtained by Grant (1977), who used a more systematic analysis and obtained values that scaled more consistently with the dimensions of the roughness elements. The vertical profile of the phase of the velocity with respect to the free-stream velocity can also be obtained from their measurements.

Table 1

Experimental Parameters for the Data Sets from a Pure Wave Motion

Data Set	u_b cm/s	ω s^{-1}	k_n cm	A_b/k_n
JC1	211.0	0.749	1.59	177.2
JC2	153.0	0.873	7.50	23.4
VDW	26.5	3.142	2.10	4.1
DVW05	50.0	0.785	15.0	4.2
DVW10	100.0	0.785	15.0	8.5
DVW15	150.0	0.785	15.0	12.7

132. Van Doorn obtained measurements in the boundary layer of a wave flume with two-dimensional artificial roughness elements. Velocities were measured at various heights above a crest and above a trough of the roughness using a laser-doppler anemometer. The value of the equivalent roughness was determined by measuring the velocity profile of a pure current flow and finding the intercept on the z axis from a semi-logarithmic plot of the velocity with height. The theoretical bed was set at the bottom of the roughness elements. The relative phase of the wave velocity was also reported. The relevant experimental parameters are given in Table 1.

133. For the case of waves and currents, the two data sets from Bakker and Van Doorn (1978) have been selected. These experiments were performed in the wave flume described in the preceding paragraph. A steady current was established in the flume by means of a recirculating pump. The inlet and outlet for the steady flow were 24 m apart. Waves were generated at one end by a flat wave board oscillating horizontally and absorbed by a wave damper at the other end. The wave period used was 2.0 sec and the water depth 0.3 m.

134. For the experiments with waves and a current, the bottom roughness elements (2 mm high at 15-mm centers) were applied over a distance of 15 m from the inlet. Velocities were measured using a laser-doppler anemometer above a crest and above a trough of the bottom roughness. The water surface elevation was measured using a resistance-type wave gage.

135. The measurements were analyzed using the waves from each wave train that were present after the start-up transients had passed and before the first reflected wave returned. Three wave trains were analyzed for pump flow rates corresponding to average velocities of 10 cm/sec and 20 cm/sec in the absence of waves. The time-averaged velocities above a trough were reported for the two flow rates. These sets will be referred to as BVD10 and BVD20, respectively. The experimental parameters are given in Table 2.

136. The pump flow rates in these experiments cannot be used as an indicator of the average flow velocity in the presence of waves. One reason is that the experimental current velocity profiles plotted in Figure 5 of the next section show that the velocity increases logarithmically with height above the bottom only up to a certain level,

Table 2

Experimental Parameters for the Data Sets from a Combined Wave and Current Motion

Data Set	u_b cm/s	ω s^{-1}	k_n cm	A_b/k_n	ϕ_{cw} deg	Current Specification
BVD10	25.7	3.142	2.1	3.9	0	u_c = 8.2 cm/s at z = 4.6 cm
BVD20	24.3	3.142	2.1	3.7	0	u_c = 22.4 cm/s at z = 5.9 cm
DV0500	50.0	0.785	15.0	4.2	0	τ_c = 3.5 Pa
DV1000	100.0	0.785	15.0	8.5	0	τ_c = 3.5 Pa
DV1045	100.0	0.785	15.0	8.5	45	τ_c = 3.5 Pa
DV1090	100.0	0.785	15.0	8.5	90	τ_c = 3.5 Pa
DV1500	150.0	0.785	15.0	12.7	0	τ_c = 3.5 Pa

after which it remains nearly constant. This indicates that the current profile at the measuring station was not fully developed; i.e., the effect of the bottom had not penetrated all the way to the surface by the time the flow reached the measuring station. Therefore, requring the depth-averaged velocity from the theoretical profiles to equal the pump flow rates would result in an error as the theory assumes fully developed flow.

137. Another reason is that the wave-induced mass transport will cause a return flow in the flume that opposes the current. This is shown in the plot of current velocities with and without waves for the same pump flow rate given in Bakker and Van Doorn (1978). For these reasons, it was decided to select a data point from near the top of the logarithmic region for each set and require the theoretical profiles to pass through that point; i.e., the current was specified as a point value rather than as a depth-averaged value.

Numerical data

138. The results for wave and wave-current flows presented in Davies, Soulsby, and King (1988) obtained from the model described in the preceding section are selected for comparison. The case studies of Davies, Soulsby, and King were performed for an assumed water depth of 10 m and a bottom of equivalent Nikuradse roughness k_n = 15 cm . The wave period was 8 sec and

the wave motion was specified by the value of the free stream velocity u_b . The current was specified by the mean shear stress τ_c .

139. The model was run for one case of waves alone with u_b = 1.0 m/sec and one case of a pure current with τ_c = 3.5 Pa which are referred to as DVW10 and DVC, respectively. Runs with waves and the current in the same direction were carried out with τ_c = 3.5 Pa and u_b = 0.5, 1.0, and 1.5 m/sec (referred to as DV0500, DV1000, and DV1500, respectively). Finally, two runs were performed with τ_c = 3.5 Pa and u_b = 1.0 m/sec with the angle between the wave direction and the mean shear stress at 45 and 90 deg (referred to as DV1045 and DV1090). The parameters needed to run the theoretical models are given in Tables 1 and 2.

140. The results are presented as profiles of the instantaneous velocity for different values of the phase of the free-stream velocity for the cases DVW10 and DV1000 and as profiles of the time-averaged velocity for all five wave-current cases and the case of a pure current. The maximum bed shear stresses and phase leads are also tabulated. The maximum wave bottom shear stress and phase lead for two more cases of waves alone were also tabulated. These had u_b = 0.5 and 1.5 m/sec and are referred to as DVW05 and DVW15, respectively.

Comparison of Model Results with Experimental Data

Waves alone

141. For the case of waves alone, the wave part of the GM model can be used with u_{*cw} replaced everywhere by u_{*w} . The SM model has the identical solution for a pure wave motion. Since the TS model does not have a separable wave component, it will not be discussed here. The solution for the wave velocity from the GM model is given by Equation 67. The phase can be found from the argument of the term in the square brackets in that equation.

142. The comparisons of the predicted wave velocity and phase with the three data sets from the physical experiments are shown in Figures 1, 2, and 3 while the comparison with the numerical data set DVW10 is shown in Figure 4. It should be noted that the problem of a pure wave motion does not involve the free parameter γ .

143. The agreement with all these data sets is quite poor with the chief drawback being the overprediction of the boundary layer and the

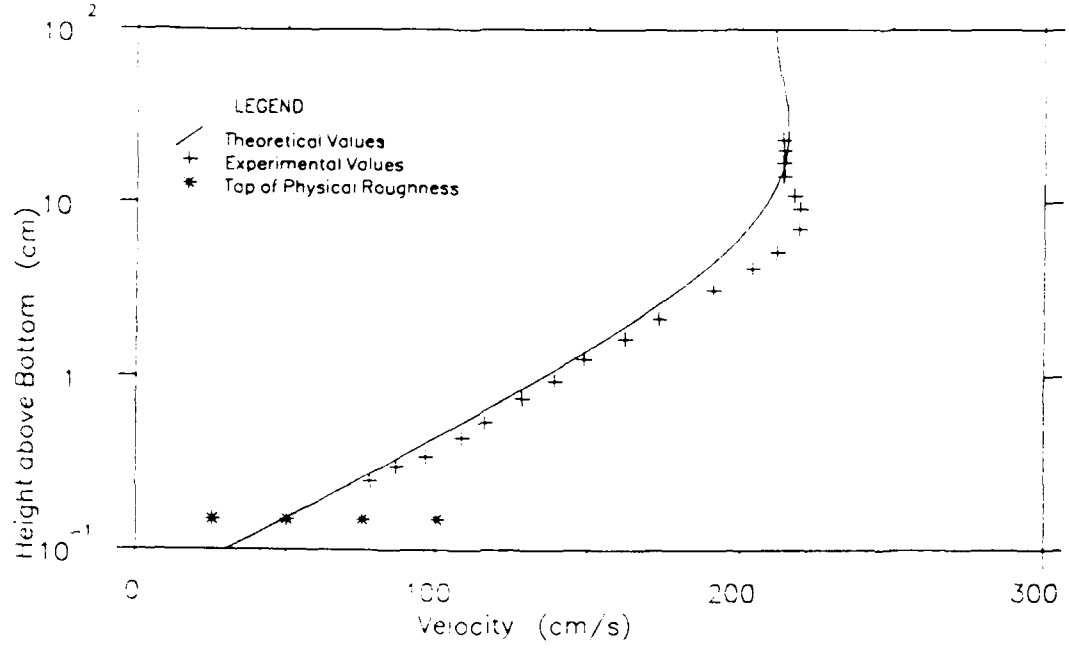

a. Wave velocity

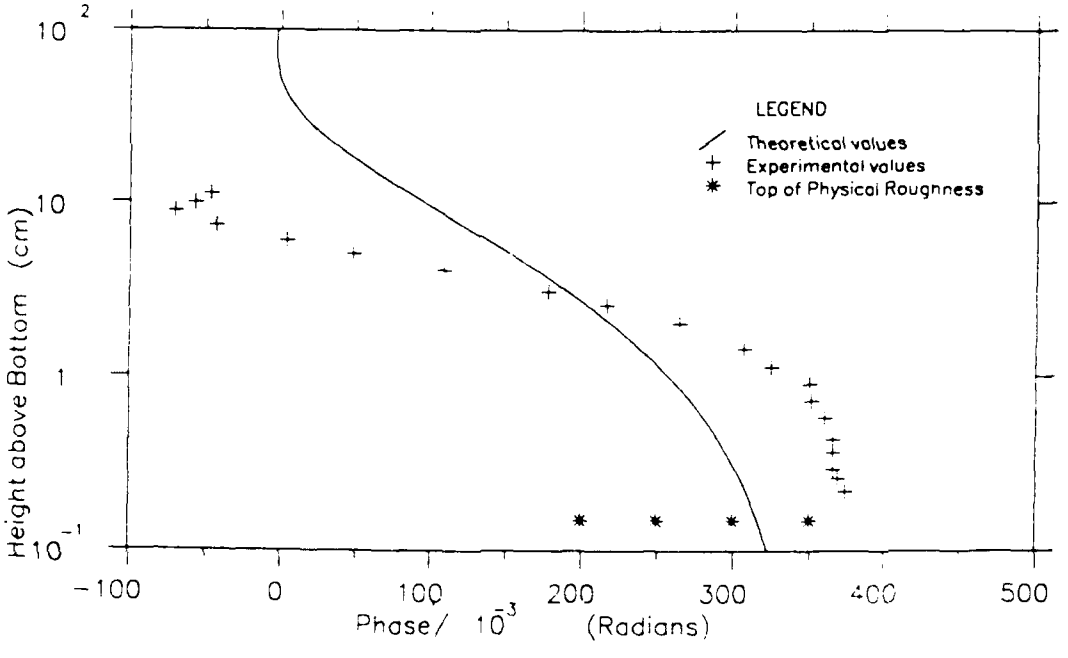

b. Phase

Figure 1. Comparison of the wave velocity and phase profiles from Jonsson and Carlsen (1976) Test 1 with the results of the GM model

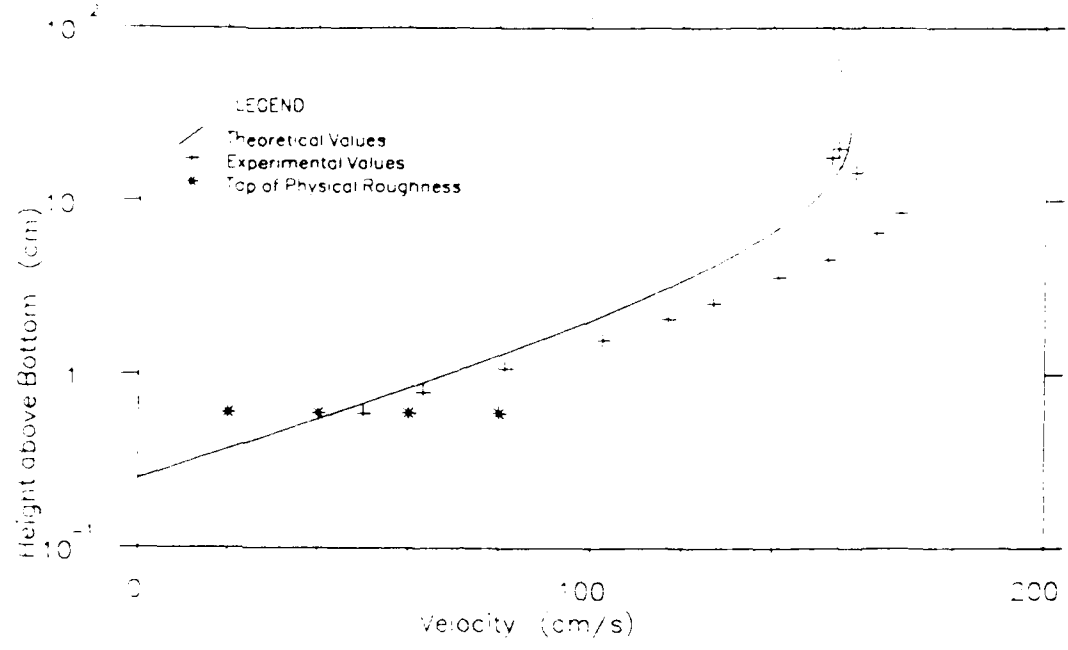

a. Wave velocity

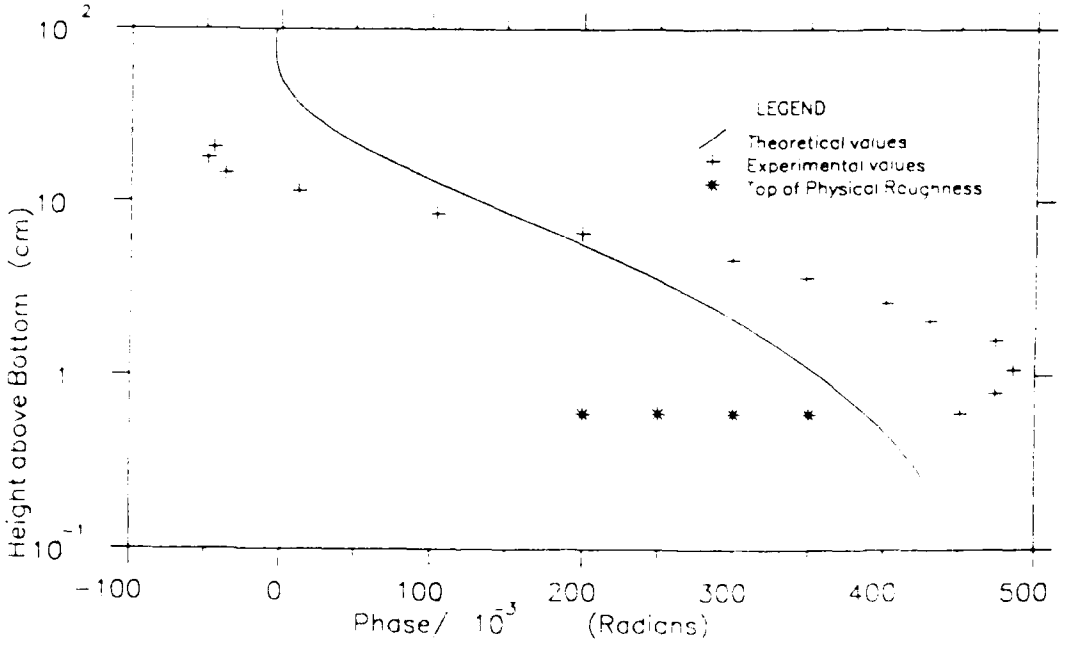

b. Phase

Figure 2. Comparison of the wave velocity and phase profiles from Jonsson and Carlsen (1976) Test 2 with the results of the GM model

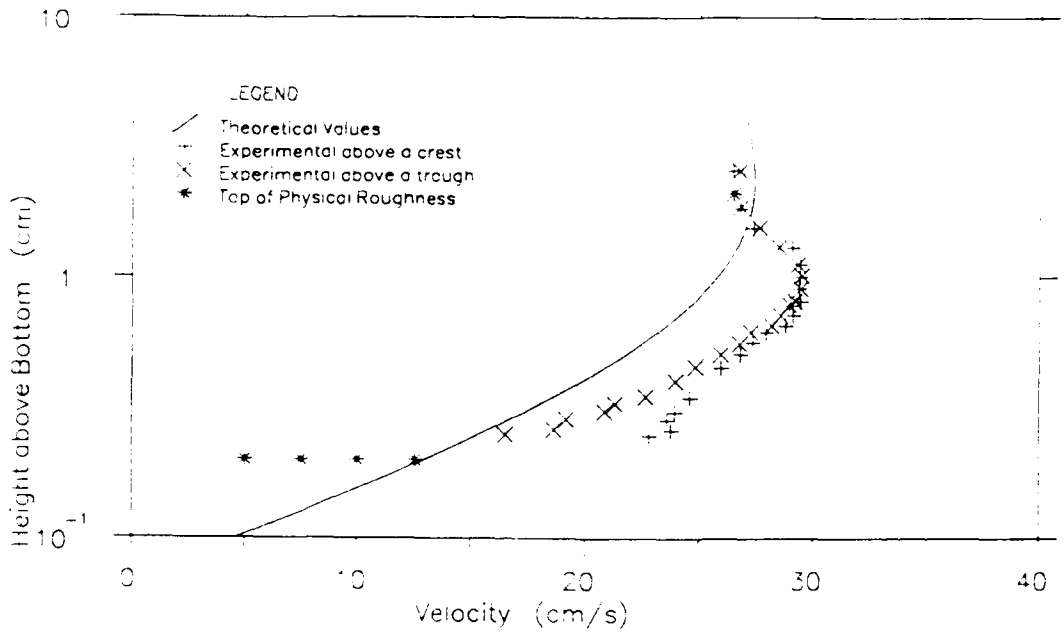

a. Wave velocity

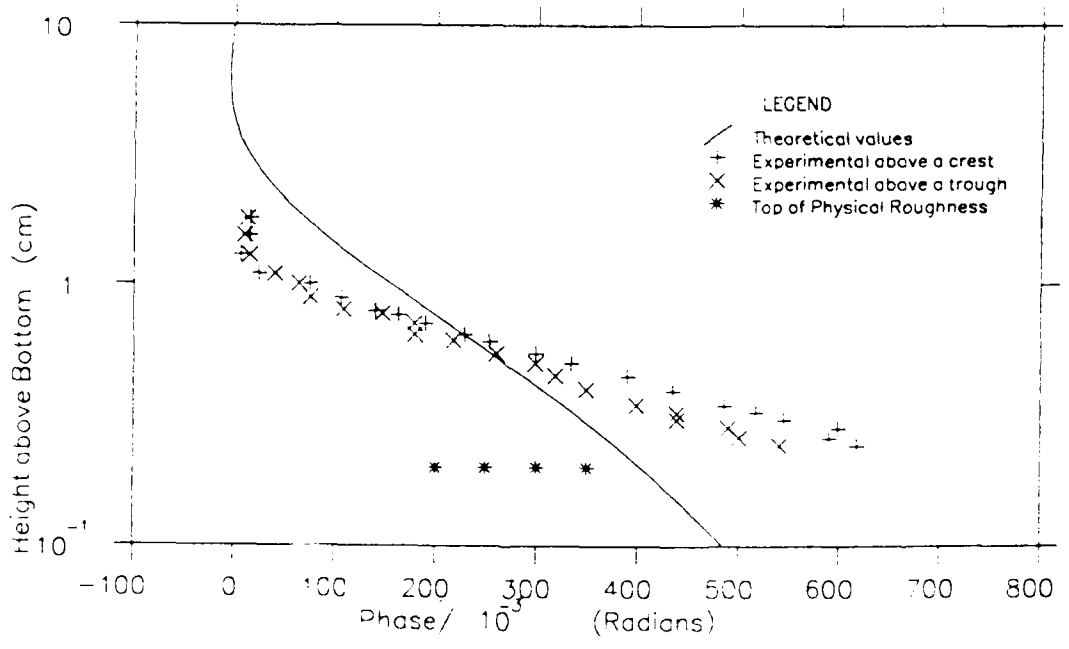

b. Phase

Figure 3. Comparison of the wave velocity and phase profiles from Van Doorn (1981) with the results of the GM model

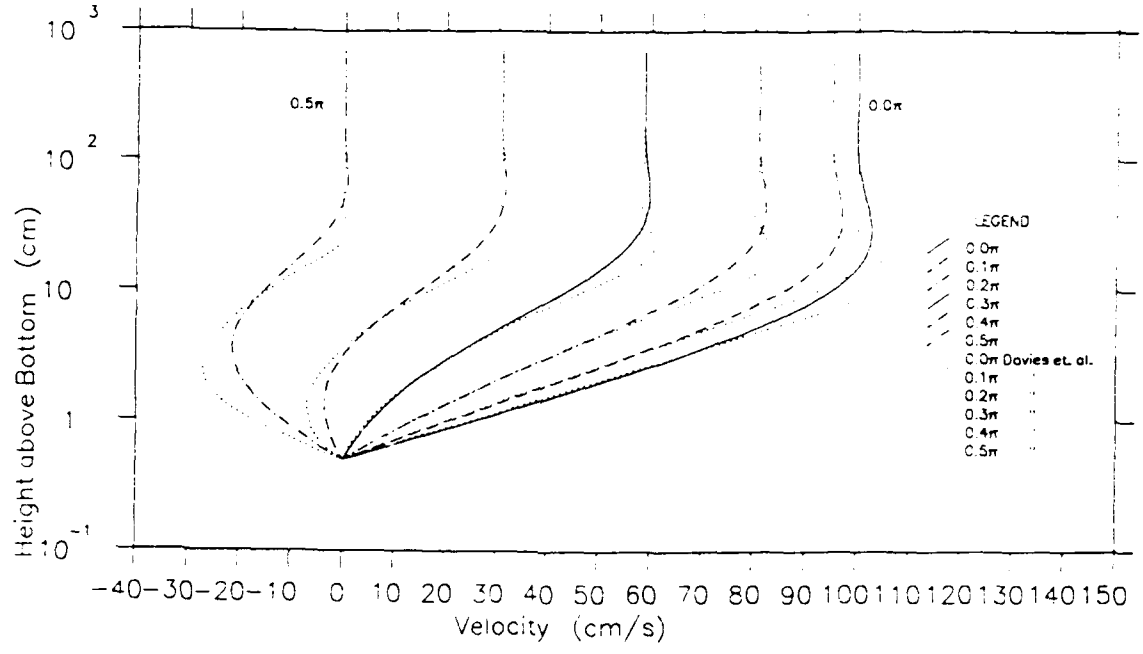

a. Wave velocity at phases $0-0.5\pi$

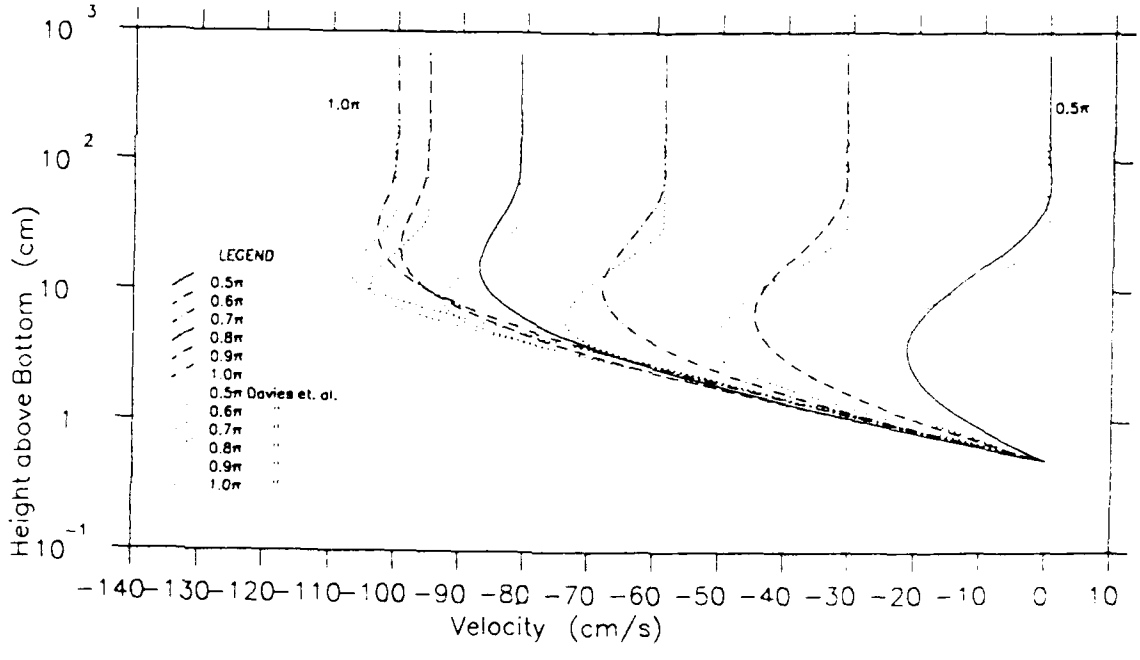

b. Wave velocity at phases $0.5\pi-\pi$

Figure 4. Comparison of the instantaneous wave velocity profile at various phases of the free stream velocity from Davies, Soulsby, and King (1988) with the results of the GM model

underprediction of the "overshoot" velocity near the top of the boundary layer. The phase is also poorly predicted particularly near the bottom. The prediction of the near bottom velocity is better with the exception of the set VDW. This set is obtained from an experiment with a very rough bottom and may be outside the range of validity of the present theory. It also shows clearly that the velocity near the roughness elements is not uniform but depends on where the measurement is made.

144. The main problems mentioned can be attributed to the use of a linearly varying eddy viscosity for the whole depth. As shown in Lundgren (1972), experimental evidence suggests an exponential decrease after a certain height. This model leads to too large a value of the eddy viscosity near the top of the boundary layer. Since the boundary layer thickness scales with the level of eddy viscosity, this continuous increase leads to overprediction of the boundary layer thickness. Furthermore, the increased eddy viscosity leads to smaller velocity gradients for the same shear stress. This results in the theoretical profile being much smoother than the experimental profiles as shown in the comparisons.

145. The values of bottom shear stress and phase from Davies, Soulsby, and King are compared with the values from the GM model in Table 3. Shear stress is overpredicted by about 20 percent while the phase lead is well

Table 3

Calculated Maximum Wave Shear Stresses and Phase Leads for the Conditions of Davies, Soulsby, and King (1988) from the GM Model Compared with the Results Given by Davies, Soulsby, and King (1988)

	τ_w (Pa)		Phase Lead (deg)	
Data Set	Davies et al.	GM Model	Davies et al.	GM Model
DVW05	8.1	9.7	28.2	29.6
DVW10	23.5	27.8	26.4	27.5
DVW15	44.3	52.0	25.2	26.3

predicted. The overprediction of the shear stress could be due to the eddy viscosity being too high.

Waves and a current

146. The current velocity profile for the conditions corresponding to each data set was calculated using each model. The results for each model are presented separately.

147. GM model. The comparisons of the results from the GM model and the data are shown in Figures 5, 6, and 7. Two values of the parameter γ in Equation 72 have been selected; $\gamma = 1.5$ is in the middle of the range suggested by Grant and Madsen (1986) while $\gamma = 1.0$ appears to give a better fit overall. Figure 7 shows the results for the case of waves and currents at an angle. These results will be shown for the GM model only because it is the only one that made allowance for any angle between the two.

148. The data set BVD20 and all the sets from Davies, Soulsby, and King show clearly the existence of two logarithmic regions with a transition region. This vindicates the reasoning behind the GM model. The set BVD10 does not show the lower region. The discontinuity in the eddy viscosity results in a kink in the velocity profile at the edge of the boundary layer while the data show a smooth transition.

149. The current for the sets BVD10 and BVD20 is specified by a velocity at a certain height; i.e., the program is run until the profile passes through this point. Since the GM model and the data sets exhibit a logarithmic velocity profile outside the boundary layer, this specification means that it is difficult to decide on the "best fit" value of γ for these sets. This is seen in Figure 5. In the case of the Davies, Soulsby, and King profiles the current is specified by the mean shear stress and different values of γ cause significant variation in the velocity profiles as seen in Figure 6.

150. However, as shown in these figures, different values of γ will apparently provide a good fit to the data for each of the three values of u_b. A value of 1.5 seems good for the set DV1500 while $\gamma = 1.0$ fits DV1000 well and an even lower value is indicated for the set DV0500. This is a shortcoming of the model and is a result of the assumed vertical structure of the eddy viscosity being oversimplified.

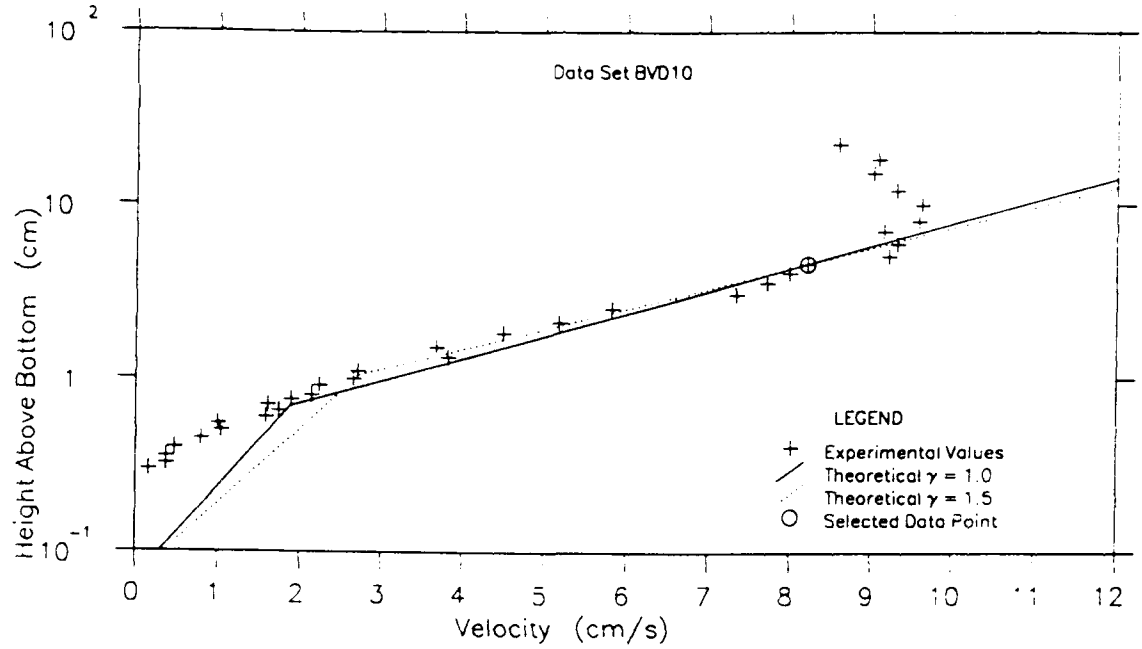

a. Data set BVD10

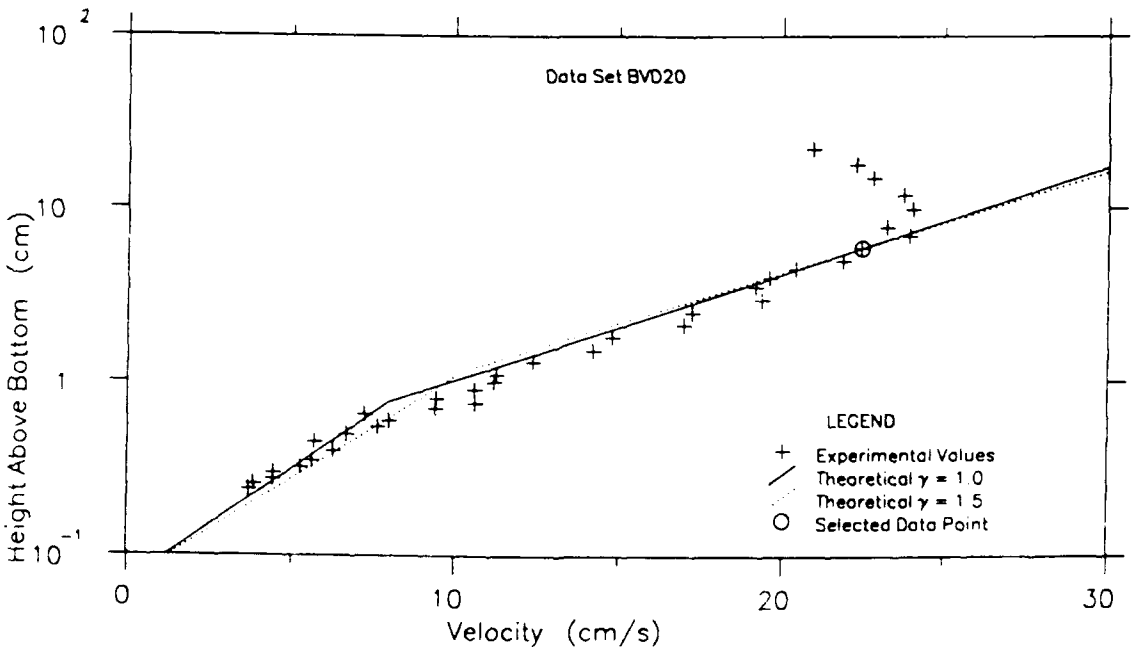

b. Data set BVD20

Figure 5. Comparison of the current velocity profiles from Bakker and Van Doorn (1978) with the results of the GM model for $\gamma = 1.0$ and $\gamma = 1.5$

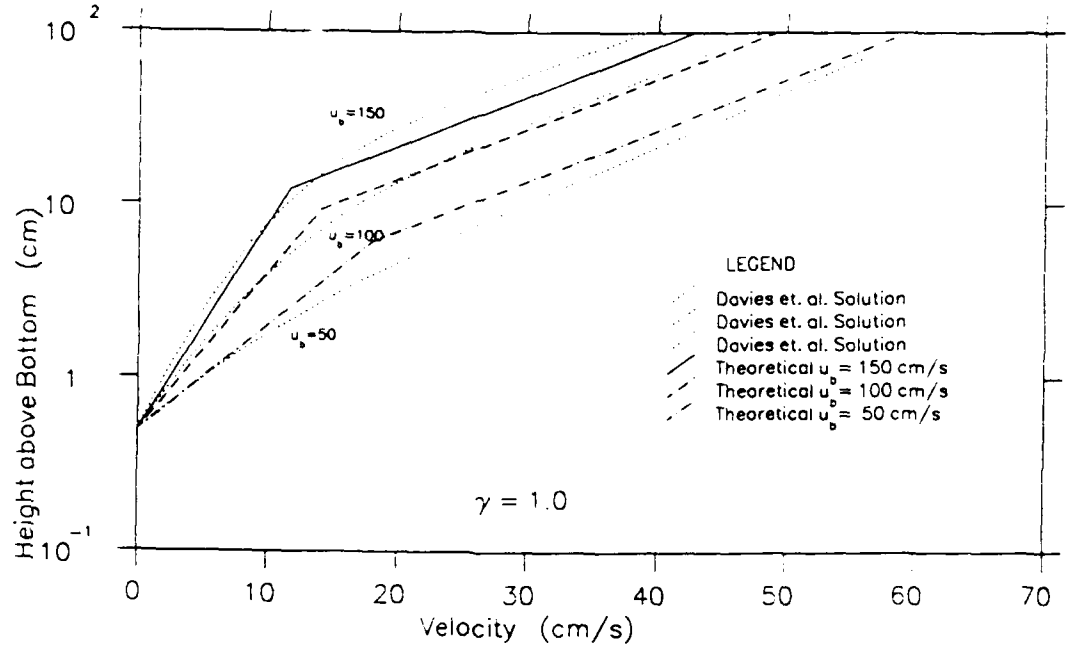

a. Comparison with $\gamma = 1.0$

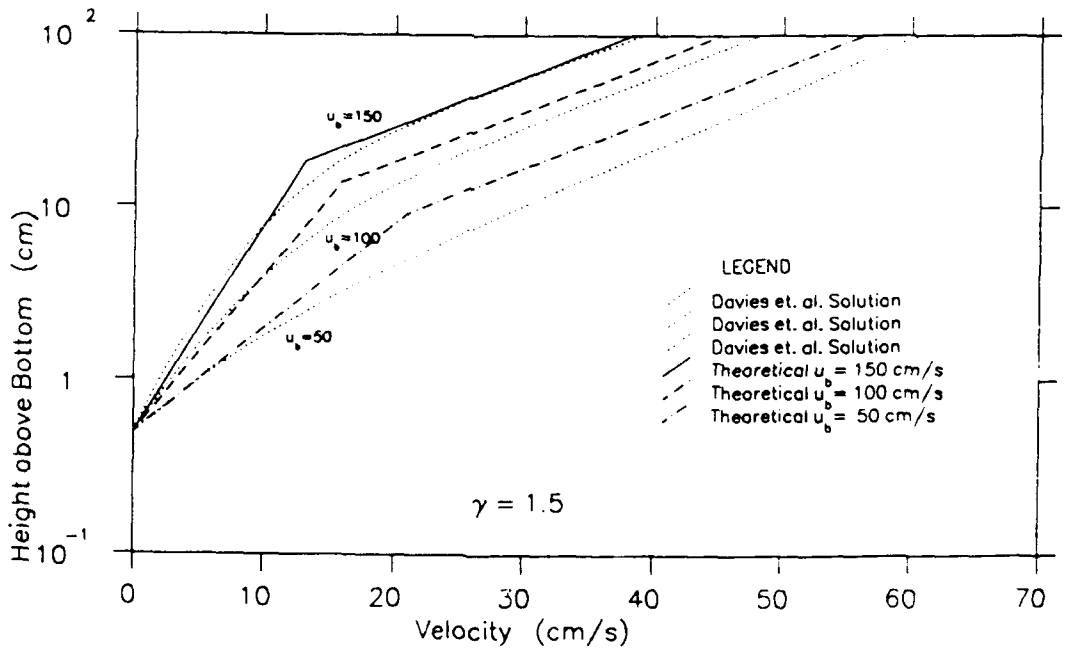

b. Comparison with $\gamma = 1.5$

Figure 6. Comparison of the current velocity profiles from Davies, Soulsby, and King (1988) for waves and currents in the same direction with the results of the GM model for $\gamma = 1.0$ and $\gamma = 1.5$

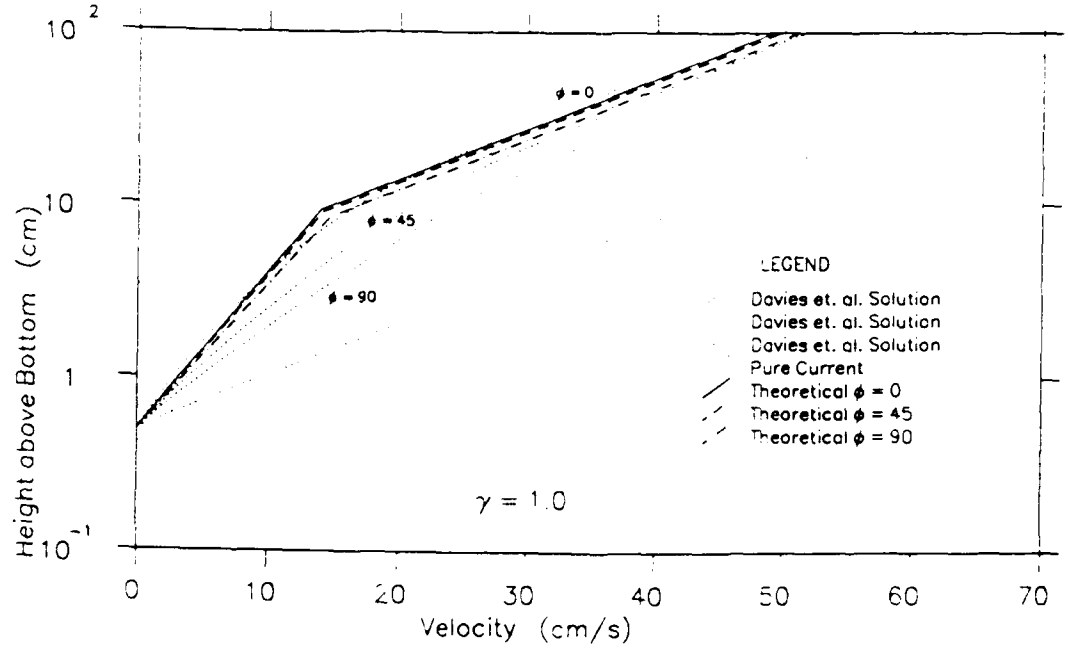

a. Comparison with $\gamma = 1.0$

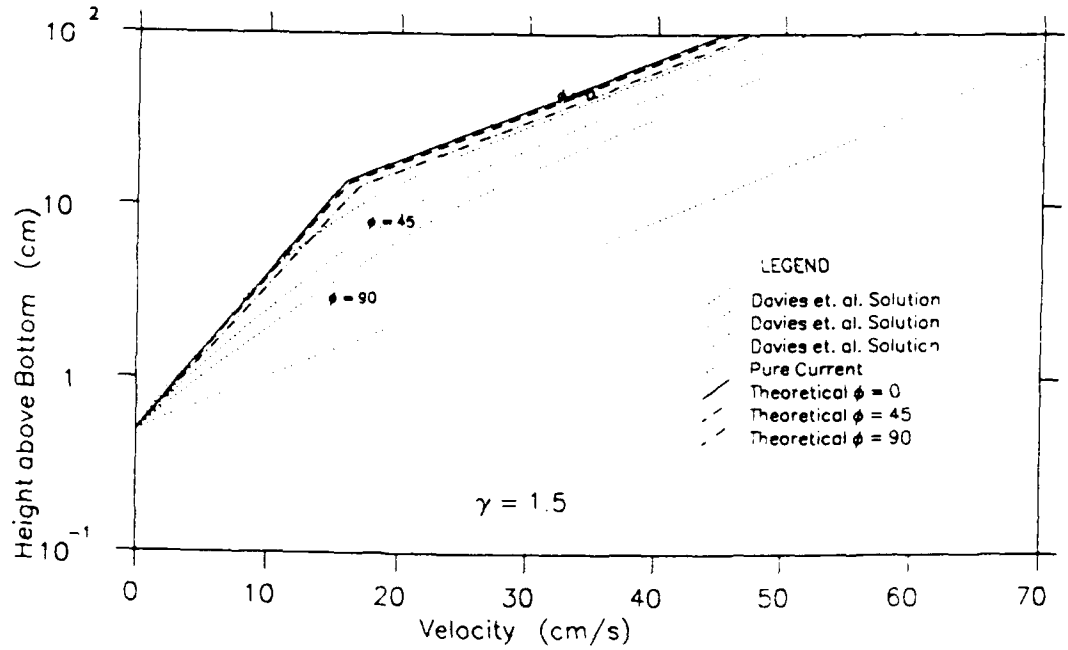

b. Comparison with $\gamma = 1.5$

Figure 7. Comparison of the current velocity profiles from Davies, Soulsby, and King (1988) for waves and currents at an angle with the results of the GM model for $\gamma = 1.0$ and $\gamma = 1.5$

Table 4

Calculated Maximum Bottom Shear Stress for the Conditions of Davies, Soulsby, and King (1988) from the GM, SM, and TS Models Compared with the Results of Davies, Soulsby, and King (1988)

	Maximum Shear Stress τ_m (Pa)			
Data Set	Davies et al.	GM Model	SM Model	TS Model
DV0500	13.0	14.7	20.6	14.7
DV1000	28.0	33.1	44.8	33.5
DV1045	27.0	31.7	--	--
DV1090	24.2	28.2	--	--
DV1500	48.9	57.3	74.6	59.2

151. Another problem is that a change in the current profile with change in the angle between the wave and the current is hardly brought out by the MG model as evidenced by the results presented in Figure 7.

152. The results for the maximum bottom shear stress of the data sets from Davies, Soulsby, and King are compared in Table 4 with the results from the three models. Since the value of γ does not come into the wave problem the maximum shear stress does not depend on γ when the current shear stress is specified, as is the case here. The table shows that the GM model overpredicts the shear stresses by about 20 percent as in the case with waves alone.

153. The current shear stress in the data sets BVD10 and BVD20 is not given but is instead determined as part of the solution. Since the solution for the GM model is logarithmic in the upper layer and this model fits the data well, the predicted current shear stress can be assumed to be close to the actual value. The predicted wave and current shear stresses from the various models are compared in Table 5, which shows that the results from the GM model for the shear stresses are fairly insensitive to the value of γ. This is in agreement with what Grant (1977) found for the original GM model.

154. SM model. The results from the SM model are presented along with the experimental data in Figures 8 and 9. Results are shown for two values

Table 5

Predicted Maximum and Current Shear Stresses from the GM, SM, and TS Models for Conditions Corresponding to the Bakker and Van Doorn Experiments

Data Set	Predicted Current Shear Stress (Pa)					Predicted Maximum Shear Stress (Pa)				
	GM Model		SM Model		TS Model	GM Model		SM Model		TS Model
	γ=1.0	γ=1.5	γ=0.1	γ=1.0		γ=1.0	γ=1.5	γ=0.1	γ=1.0	
BVD10	0.18	0.22	0.18	0.53	0.44	2.9	3.0	3.8	4.8	3.3
BVD20	0.80	0.89	0.81	1.80	1.33	3.6	3.7	5.1	6.8	4.3

of the parameter $\gamma - \gamma = 1.0$ as originally proposed by Smith (1977) and $\gamma = 0.1$ which is the value that appears to give a good fit to the data in general. The use of $\gamma = 0.1$ leads to a significant improvement in the profiles. However, when this value is used, the level of the boundary layer (ℓ as defined in Equation 78) is set very near or below the level of the physical roughness (2 mm for the Bakker and Van Doorn data and 5 cm for the Davies, Soulsby, and King data).

155. The reason for this is that inside the wave boundary layer the combined shear velocity is found by adding the wave and current shear velocities instead of defining it by means of the combined shear stress as done in GM model. This results in a combined shear velocity that is too high causing excessive retardation of the current within the boundary layer. Therefore, a good fit is obtained when the boundary layer is kept very small. Another drawback of this model is that the profile outside the boundary layer is not exactly logarithmic resulting in a poor fit to the data.

156. It is seen from Figure 9 that, as in the GM model, different values of γ will give a good fit to each of the three profiles. This is a further indication that a two-layer model is insufficient to represent the velocity profile.

157. The maximum shear stresses and phase leads predicted by the model for the Davies, Soulsby, and King conditions are also given in Table 4. As before, these values are not influenced by the value of γ when the current

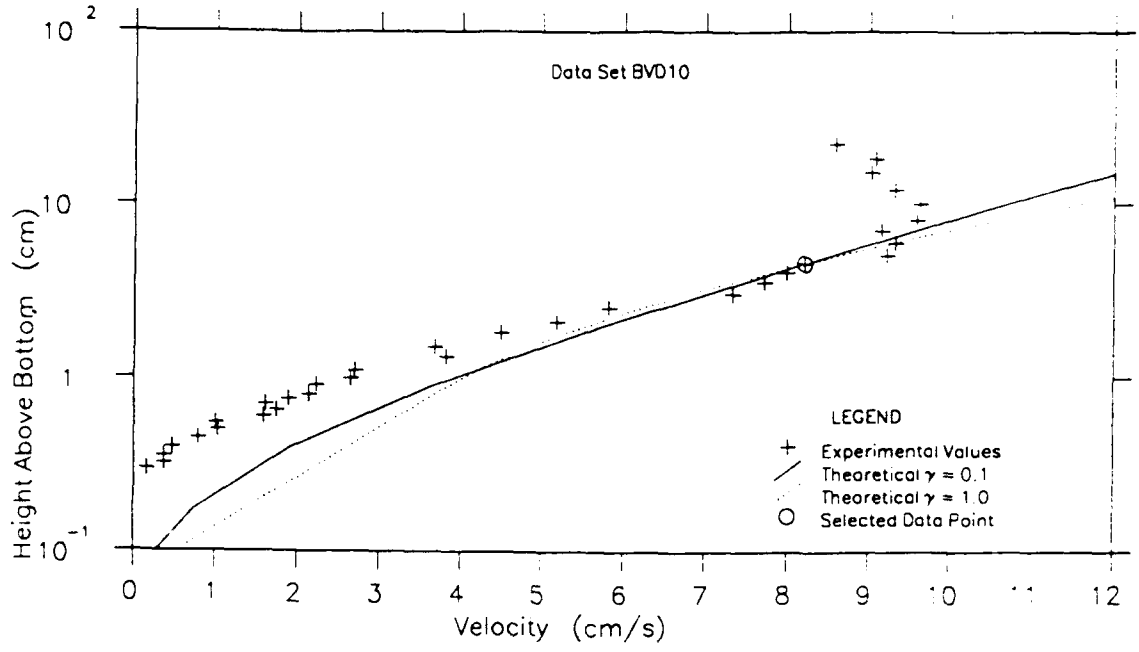

a. Data set BVD10

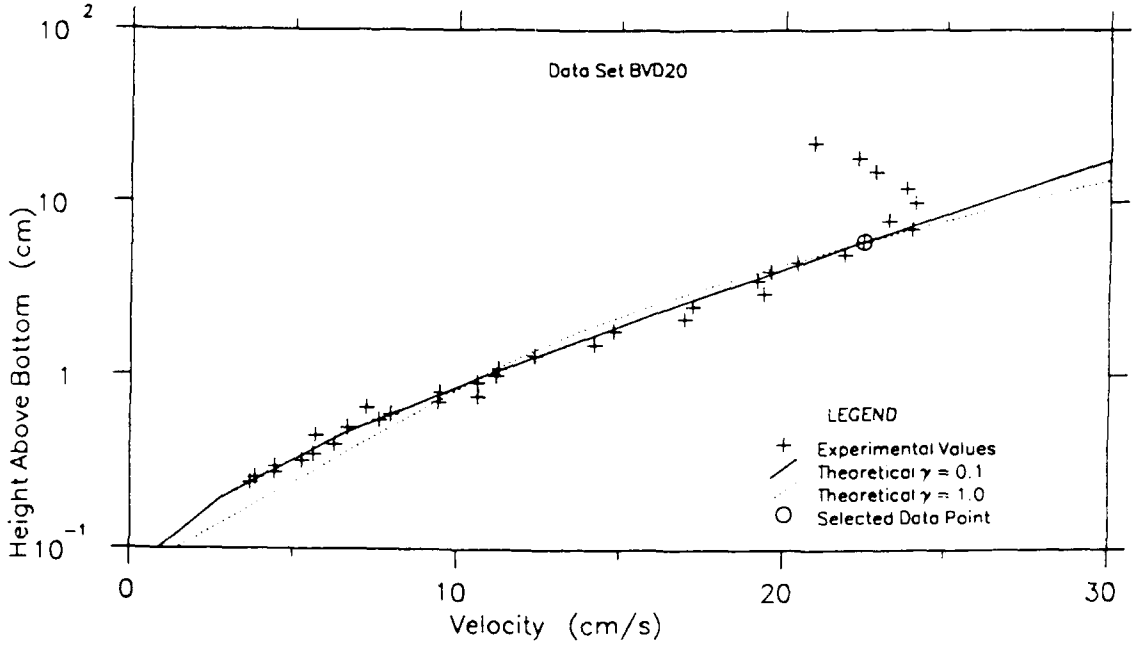

b. Data set BVD20

Figure 8. Comparison of the current velocity profiles from Bakker and Van Doorn (1978) with the results of the SM model for $\gamma = 0.1$ and $\gamma = 1.0$

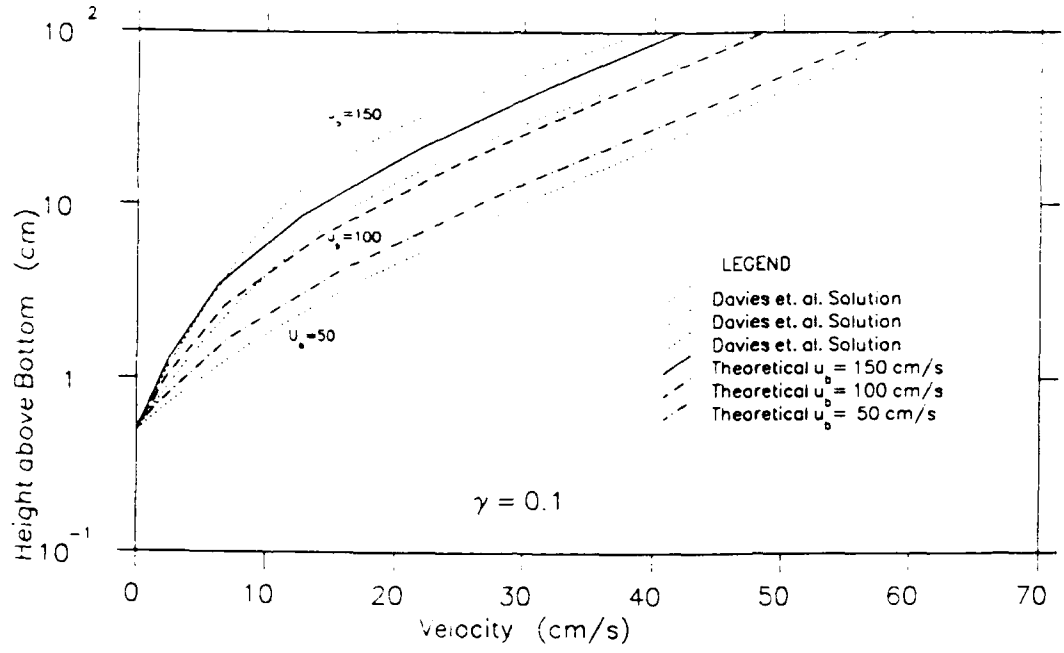

a. Comparison with $\gamma = 0.1$

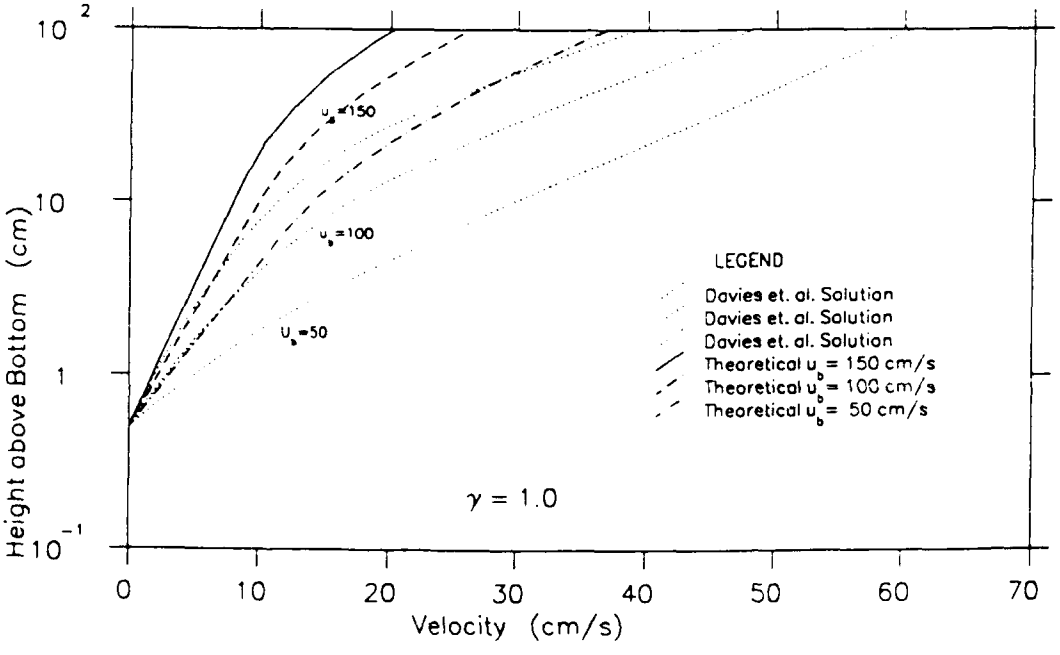

b. Comparison with $\gamma = 1.0$

Figure 9. Comparison of the current velocity profiles from Davies, Soulsby, and King (1988) for waves and current in the same direction with the results of the SM model for $\gamma = 0.1$ and $\gamma = 1.0$

shear stress is given. The table shows that the wave shear stresses are overpredicted by about 50 percent. This is due to the eddy viscosity being too large in the wave problem. This is further evidence that the definition of the combined shear velocity in this model is incorrect.

158. As shown in Table 5, the shear stresses predicted for the data sets BVD10 and BVD20 are quite different for the two values of γ used. The current shear stresses obtained with $\gamma = 0.1$ are close to those found from the GM model, but the corresponding wave shear stresses are overpredicted.

159. Therefore, it can be concluded that the SM model does not perform as well as the GM model for any of the data sets regardless of the value chosen for γ. The selected eddy viscosity inside the boundary layer is too high while the form of the eddy viscosity in the upper layer is incorrect.

160. TS model. The results of the TS model are compared with the data in Figures 10 and 11. The model does not predict any data set well because the wave boundary layer thickness is greatly overpredicted in most of the cases considered. However, even when the boundary layer height is better calculated, as in the set DV1500, the assumption of a constant eddy viscosity in the upper layer leads to an incorrect shape of the profile there as shown in Figure 11.

161. The calculated maximum shear stresses corresponding to the Davies Soulsby, and King conditions in Table 4 are very close to the values obtained from the GM model. This is not surprising as the wave problem formulations in the two models are nearly identical. The wave shear stresses in Table 5 are also almost the same as from the GM model, but the current shear stress is much larger.

162. The reason for the poor performance of this model appears to be the method used to define d, the thickness of the wave boundary layer in a wave-current flow. The definition in terms of the integral in Equation 81 is an attempt to relate d to the displacement thickness of the boundary layer. For a pure current with a logarithmic velocity profile, the evaluation of this integral yields $d = 0.1z_h$ while for the current profile derived for this model $d = 0.133z_h$ is obtained. In the limit of a pure wave motion, $d = 0.1\delta$ is obtained with δ defined by Equation 62 with u_{*w} used in place of u_{*cw}.

MISSING PAGES WILL BE INSERTED AT AN LATER DATE
AS ERRATA(S)

62 thru 70

186. The boundary conditions are the no-slip condition at $z = z_0 = k_n/30$, and the approach to the free stream velocity as $z \to \infty$. Since u_d is defined in Equation 43, the no-slip condition becomes

$$u_d = -1 \qquad \text{at} \qquad \zeta = \zeta_0 = z_0/\delta \tag{109}$$

which, for $\zeta_0 < a$, by use of Equation 103 yields

$$A[\ker(2\sqrt{\zeta_0}) + i\,\mathrm{kei}(2\sqrt{\zeta_0})] + B[\mathrm{ber}(2\sqrt{\zeta_0}) + i\,\mathrm{bei}(2\sqrt{\zeta_0})] = -1 \tag{110}$$

187. From the condition at infinity it is obtained that

$$u_d \to 0 \qquad \text{as} \qquad \zeta \to \infty \tag{111}$$

which is satisfied only if F, in Equation 108, is zero since the Kelvin functions ber and bei become exponentially large as their arguments approach infinity (Abramowitz and Stegun 1972, Chapter 9). Thus,

$$F = 0 \tag{112}$$

188. The remaining conditions necessary to determine the constants are matching conditions applied at the inner and outer boundaries of the intermediate region, i.e., at $\zeta = a$ and $\zeta = a/\epsilon$, respectively. The matching conditions require continuity of velocity and velocity gradient (shear stress) as the boundaries are approached from above and below.

189. Matching of velocities is readily accomplished by use of Equations 103 and 106 and Equations 106 and 108 at $\zeta = a$ and $\zeta = a/\epsilon$, respectively, and results in

$$A[\ker(2\sqrt{a}) + i\,\mathrm{kei}(2\sqrt{a})] + B[\mathrm{ber}(2\sqrt{a}) + i\,\mathrm{bei}(2\sqrt{a})] = Ce^{\sqrt{ia}} + De^{-\sqrt{ia}} \tag{113}$$

and

$$Ce^{\sqrt{ia}/\epsilon} + De^{-\sqrt{ia}/\epsilon} = E[\ker(2\sqrt{a}/\epsilon) + i\,\mathrm{kei}(2\sqrt{a}/\epsilon)] \tag{114}$$

190. Matching of velocity gradients at $\zeta = a$ is obtained from Equations 103 and 106 and results in

$$A[\mathrm{ker}'(2\sqrt{a}) + i\,\mathrm{kei}'(2\sqrt{a})] + B[\mathrm{ber}'(2\sqrt{a}) + i\,\mathrm{bei}'(2\sqrt{a})] = C\sqrt{ie}^{\sqrt{ia}} - D\sqrt{ie}^{-\sqrt{ia}} \quad (115)$$

while matching of velocity gradients at $\zeta = a/\epsilon$, obtained from differentiation of Equations 106 and 108, yields

$$C\sqrt{ie}^{\sqrt{ia}/\epsilon} - D\sqrt{ie}^{-\sqrt{ia}/\epsilon} = E[\mathrm{ker}'(2\sqrt{a}/\epsilon) + i\,\mathrm{kei}'(2\sqrt{a}/\epsilon)] \quad (116)$$

191. In Equations 115 and 116 the primes denote differentiation with respect to the argument of the function. Solution of the five linear equations, Equations 110, 113, 114, 115, and 116, for the five arbitrary constants constitutes the solution of the wave problem. Inspection of the equations involved reveals that the parameters to be specified in order to obtain a solution are

$$\zeta_0 = \frac{\zeta_0}{\delta} = \frac{k_n/30}{\kappa u_{*cw}/\omega} \quad ; \quad a \quad \text{and} \quad \epsilon = \frac{u_{*c}}{u_{*cw}} \quad (117)$$

192. These three parameters are significant in determining the nature of the solution: ζ_0 expresses the effect of bottom roughness since it depends on the equivalent Nikuradse sand grain roughness, k_n ; a expresses the fraction of the wave boundary layer thickness over which the eddy viscosity is assumed to vary linearly; and ϵ expresses the relative magnitude of current and combined wave-current shear velocities.

193. In a physical application of the theoretical results presented above, it is reasonable to assume a scenario in which k_n , the bottom roughness, u_b and ω , the waves, and $u_{*c} = \sqrt{\tau_c/\rho}$, the average bottom shear stress, are known or specified. This leaves a and u_{*cw} to be determined before a solution to the wave problem can be obtained. As alluded to previously, the determination of u_{*cw} calls for a closure hypothesis, while a should be regarded as a free (fitting) parameter.

Closure of Wave Problem and Wave Friction Factor

194. In the present analysis, the closure hypothesis is chosen by specifying that the shear velocity, u_{*cw}, scaling the eddy viscosity in the wave boundary layer, corresponds to the maximum combined wave-current bottom shear stress, τ_m, i.e.,

$$u_{*cw} = \sqrt{\tau_m/\rho} \tag{118}$$

195. The relation between u_{*cw} and u_{*w} can be found from Equation 58 to be

$$u_{*cw} = \sqrt{\tau_m/\rho} = u_{*w}(1 + 2\mu^2\cos\phi_c + \mu^4)^{\frac{1}{4}} \tag{119}$$

with μ defined in Equation 59. From the definitions of the parameters expressing the relative magnitudes of shear velocities, Equations 101 and 59, a relationship between ϵ and μ

$$\epsilon = \mu(1 + 2\mu^2\cos\phi_{cw} + \mu^4)^{-\frac{1}{4}} \tag{120}$$

is obtained.

196. Thus, the parameter ϵ, necessary to specify in order to obtain a solution to the wave problem, may alternatively be thought of as expressing the relative importance of waves and currents, μ, and the direction of the current relative to the waves, ϕ_{cw}.

197. While the closure hypothesis adopted here defines u_{*cw} and therefore the eddy viscosity variation, it is not readily seen how its value is to be determined from knowledge of bottom roughness, k_n, and wave characteristics, u_b and ω, other than by trial and error, i.e., assume a value of u_{*cw}, thereby specifying the necessary parameters given by Equation 117 with a assumed known, and then use the definition of the maximum wave bottom shear stress in conjunction with Equation 119 to see if the assumed value of u_{*cw} was correct. This procedure can be facilitated by the introduction of a wave friction factor.

198. Jonsson (1966) defined a friction factor for pure wave motion f_w by

$$\tau_w = \tfrac{1}{2}\rho f_w u_b^2 \tag{121}$$

199. Here f_w represents the entire interaction of the wave motion specified by u_b ($u_b = u_\infty$) with the bottom. For fully rough turbulent flow, it was found that

$$f_w = f\left[\frac{A_b}{k_n}\right] \tag{122}$$

where

$$A_b = \frac{u_b}{\omega} \tag{123}$$

is the excursion amplitude and k_n the equivalent Nikuradse roughness. Thus A_b/k_n is a relative roughness parameter.

200. In analogy with Equation 121, a wave friction factor for the wave-current problem can be defined as

$$\tau_w = \tfrac{1}{2}\rho f_{wc} u_b^2 \tag{124}$$

where the subscript wc reflects the fact that the increase in bottom turbulence and thereby bottom wave shear stress due to the current is taken into account.

201. Introducing this definition of the wave friction factor along with Equation 119 in the definition of ζ_0 as given by Equation 117 one obtains

$$\zeta_0 = \frac{k_n/30}{\kappa u_{*cw}/\omega} = \frac{k_n/30}{\kappa u_{*w}(1 + 2\mu^2\cos\phi_c + \mu^4)^{\frac{1}{4}}/\omega} = \frac{\sqrt{2}}{30\kappa}\,\frac{k_n}{A_b'}\,\frac{1}{\sqrt{f_{wc}'}} \tag{125}$$

in which

$$A_b' = \frac{u_b}{\omega}(1 + 2\mu^2\cos\phi_{cw} + \mu^4)^{\frac{1}{2}} = A_b(1 + 2\mu^2\cos\phi_{cw} + \mu^4)^{\frac{1}{2}} \tag{126}$$

and

$$f_{wc}' = f_{wc}(1 + 2\mu^2\cos\phi_{cw} + \mu^4)^{-\frac{1}{2}} \tag{127}$$

202. Thus, specifying a value of ζ_0 is identical to specifying a relationship between the modified relative roughness, k_n/A_b', and the modified wave friction factor, f_{wc}'.

203. An alternative expression to Equation 124 for the maximum wave bottom shear stress may be obtained directly from the definition

$$\frac{\tau_w}{\rho} = \lim_{z \to "0"} \left\{ \left| \nu_t \cdot u_b \cdot \frac{\partial u_d}{\partial z} \right| \right\} \tag{128}$$

in which the limit $z \to$ "0" may be strictly enforced, i.e., $z \to 0$, or loosely enforced by evaluating the expression at $z = z_0$, the location where $u_w = 0$. In either case, it is expected that the definition of the bottom shear stress falls within the near-bottom region, $z \leq a\delta$, where u_d is given by Equation 108 and ν_t by the first expression in Equation 100. This shows that very rough flows (i.e., low A_b/k_b) are not considered. For these flows a model such as that of Kajiura (1968) or Christoffersen and Jonsson (1985) would be appropriate.

204. Introducing the appropriate expressions for ν_t and u_d in Equation 128 and expressing u_{*cw} as given by Equation 119 results in

$$\begin{aligned} \frac{1}{u_b} u_{*w}^2 &= \kappa u_{*cw} \lim_{\zeta \to "0"} \left[\left| \zeta \frac{du_d}{d\zeta} \right| \right] = \kappa u_{*w} (1 + 2\mu^2 \cos\phi_{cw} + \mu^4)^{\frac{1}{4}} \lim_{\zeta \to "0"} \left[\left| \sqrt{\zeta} \frac{du_d}{d(2\sqrt{\zeta})} \right| \right] \\ &= \kappa u_{*w} (1 + 2\mu^2 \cos\phi_{cw} + \mu^4)^{\frac{1}{4}} \lim_{\zeta \to "0"} \{ \sqrt{\zeta} \left| A[\ker'(2\sqrt{\zeta}) \right. \\ &\quad \left. + i\, \mathrm{kei}'(2\sqrt{\zeta})] + B[\mathrm{ber}'(2\sqrt{\zeta}) + i\, \mathrm{bei}'(2\sqrt{\zeta})] \right| \} \end{aligned} \tag{129}$$

205. When $u_{*w} = \sqrt{\tau_w/\rho}$ is expressed in terms of the wave friction factor defined by Equation 124, this expression may be regarded as an equation for the modified wave friction factor:

$$\begin{aligned} \sqrt{f_{wc}'} = \sqrt{2}\kappa \lim_{\zeta \to "0"} \{ & \sqrt{\zeta} \left| A[\ker'(2\sqrt{\zeta}) + i\, \mathrm{kei}'(2\sqrt{\zeta})] \right. \\ & \left. + B[\ker'(2\sqrt{\zeta}) + i\, \mathrm{kei}'(2\sqrt{\zeta})] \right| \} \end{aligned} \tag{130}$$

206. If the limiting process in Equation 130 is strictly enforced, i.e., $\zeta \to 0$, the asymptotic expansions for Kelvin functions given by Abramowitz and Stegun (1972, Chapter 9) show that only the term involving ker′ survives the limiting process, since

$$\lim_{\zeta \to 0} \{ \ker'(2\sqrt{\zeta}) = -\frac{1}{2\sqrt{\zeta}} \tag{131}$$

while the remaining terms behave as $\sqrt{\zeta}\ln\zeta$ or $\sqrt{\zeta}$ and therefore vanish as $\zeta \to 0$.

207. For the limit $\zeta \to 0$ Equation 130 therefore becomes

$$\sqrt{f_{wc}'} = \kappa \frac{|-A|}{\sqrt{2}} \qquad \text{for limit} \quad \zeta = 0 \tag{132}$$

while interpreting the limiting process $\zeta \to$ "0" in Equation 130 as $\zeta = \zeta_0$ results in

$$\sqrt{f_{wc}'} = \sqrt{2}\kappa\sqrt{\zeta_0}\left|A[\mathrm{ker}'(2\sqrt{\zeta_0}) + i\ \mathrm{kei}'(2\sqrt{\zeta_0})] + B[\mathrm{ber}'(2\sqrt{\zeta_0}) + i\ \mathrm{bei}'(2\sqrt{\zeta_0})]\right| \qquad \text{for limit} \quad \zeta = \zeta_0 \tag{133}$$

208. The two values obtained from Equations 132 and 133 are practically identical for small values of ζ_0 (large A_b/k_b). For larger values of ζ_0, use of Equation 132 leads to values of the phase lead of the bottom shear stress over the free stream velocity much greater than 45°. For turbulent flow, this value is expected to be less than 45°, which is the result for laminar flow. Also since ζ_0 is the level at which the velocity is formally set to zero, enforcing the limit in Equation 128 does not seem consistent. For these reasons Equation 128 is evaluated at $\zeta = \zeta_0$ for the rest of this study.

209. For $A_b'/k_n = 1$ and $\epsilon = 0.1$ the value of f_{wc}' obtained from Equations 132 and 133 are 0.268 and 0.159, respectively. For $A_b'/k_n = 10.0$, they are 0.056 and 0.063 while for $A_b'/k_n = 100$, they are 0.022 and 0.0215, respectively.

Modified Wave Friction Factor Diagram

210. Equation 133 can be used to derive a modified wave friction factor diagram in analogy to the diagrams for pure wave motion derived theoretically by Kajiura (1968) and semi-empirically by Jonsson (1976).

211. This is done by solving Equations 110, 113, 114, 115, and 116 for assumed values of ζ_0, α, and ϵ. Introducing the calculated values of A and B into Equation 133 results in a value of f_{cw}' while the corresponding value of A_b'/k_n is found from Equation 126. Repeating this

process for various values of ζ_0 with a and ϵ kept constant results in a modified wave friction factor diagram for that particular combination of a and ϵ. This shows that for a given a, the wave friction factor f_{wc} is now a function of three variables, A_b/k_n, μ, and $\cos\phi_{cw}$.

212. Figure 12 presents an example of a modified wave friction factor diagram for several values of ϵ with $a = \frac{1}{2}$. The use of the modified friction factor and relative roughness as defined by Equations 126 and 127 effectively reduces the relationship to a single curve independent of the value of ϵ. Some dependency on ϵ does become apparent for very small values of the relative roughness as shown in the expanded figure for small A_b'/k_n.

213. The advantages of using the modified friction factor diagram are well brought out in Figure 13, which shows the relationship between the actual friction factor f_{wc} and the actual relative roughness A_b/k_n for a range of ϵ for a co-directional wave current system ($\phi_{cw} = 0$). These figures show that f_{wc} depends strongly on ϵ, unlike in the modified fraction factor diagrams. The collapse of the different lines onto a single curve will make the use of the diagram much simpler.

214. The parameter a is treated so far as a free parameter to be determined after comparison with experimental data. Figure 14 shows the wave friction factor for a pure wave motion ($f_{wc}' = f_{wc} = f_w$) against the relative roughness for different values of a. These show that the wave friction factor is essentially independent of a for values of the relative roughness greater than 20 or so. Some dependency on a is present for smaller values of the relative roughness as shown in the expansion for small A_b/k_n.

215. Therefore given u_b, ω, k_n, and ϕ_{cw} and assuming a value of μ, f_{wc}' can be found from the graph. Then f_{wc} can be found from Equation 127 and u_{*w} from Equation 124. This makes the iterative solution easier to carry out.

Current Problem

216. Having solved the wave problem, the problem of determining the current velocity profile remains. This problem is governed by Equation 53 with ν_t given by Equation 100. Proceeding with the solution from the

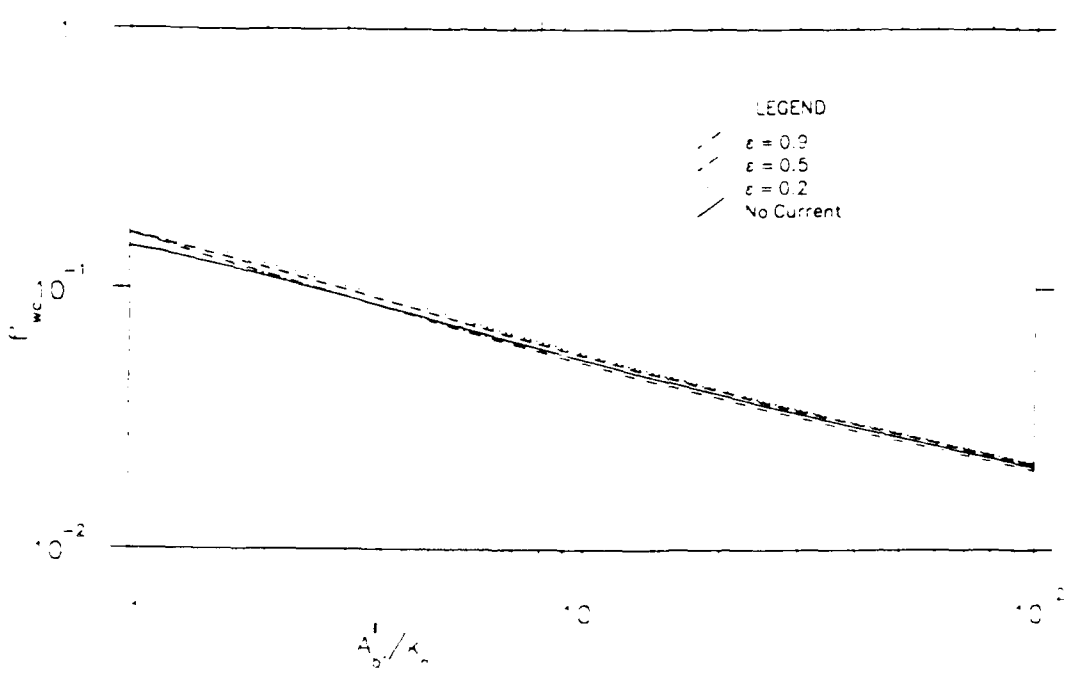

a. Friction factor diagram for $1 < A_b'/k_n < 100$

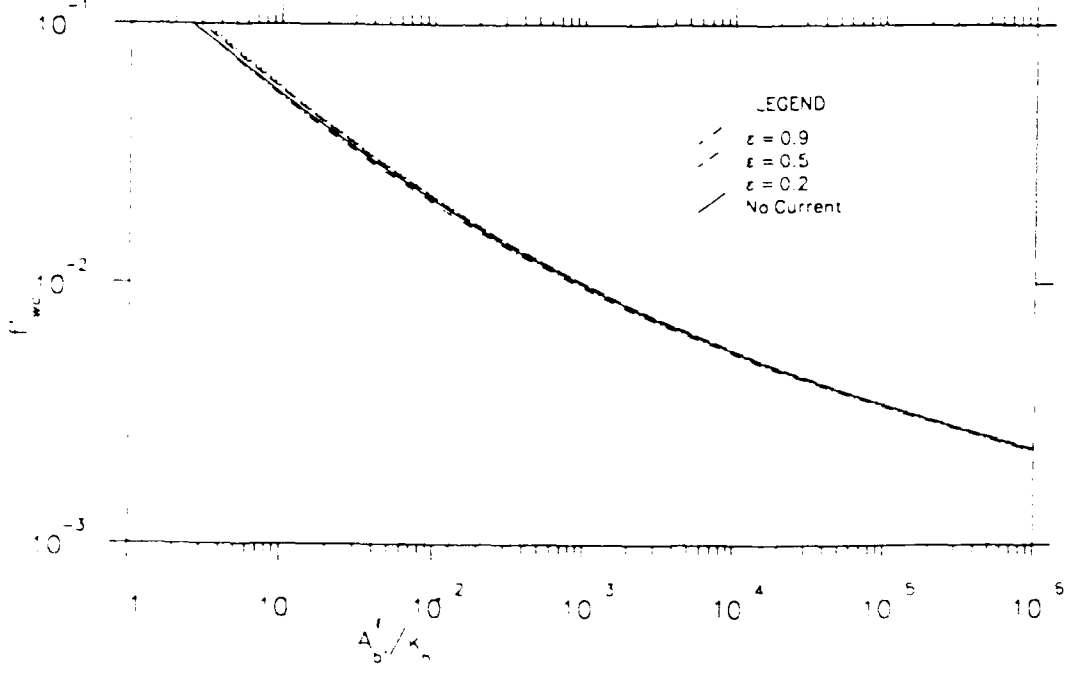

b. Friction factor diagram for $1 < A_b'/k_n < 10^6$

Figure 12. Modified wave friction factor diagram with $a = 0.5$ for several values of ϵ

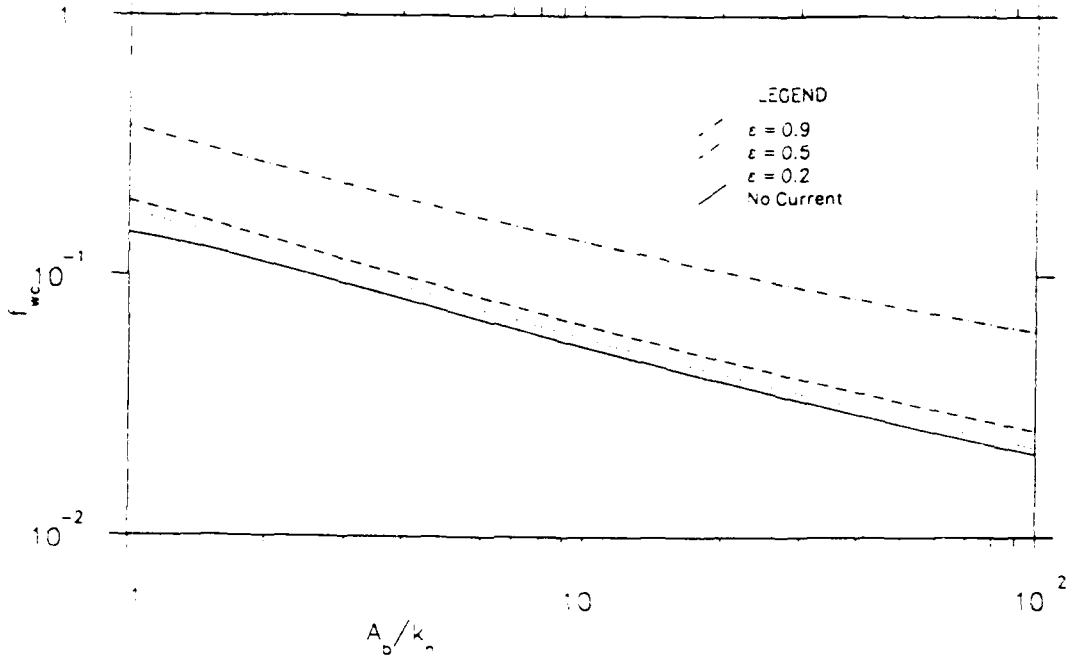

a. Friction factor diagram for $1 < A_b/k_n < 100$

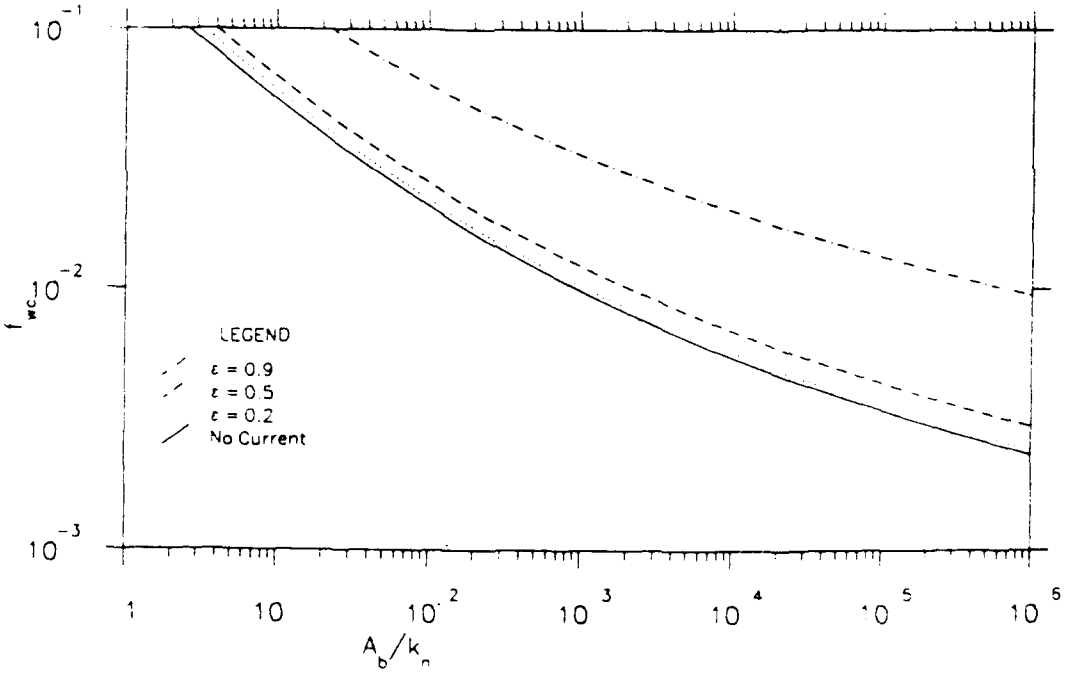

b. Friction factor diagram for $1 < A_b/k_n < 10^6$

Figure 13. Wave friction factor diagram for waves and currents in the same direction with $a = 0.5$

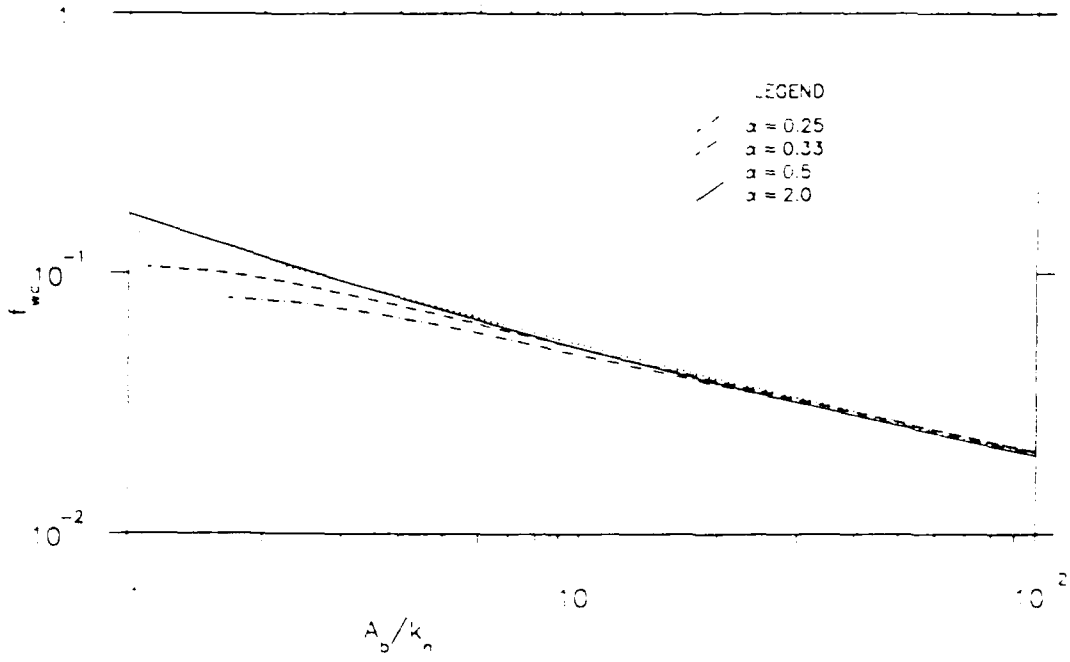

a. Friction factor diagram for $1 < A_b/k_n < 100$

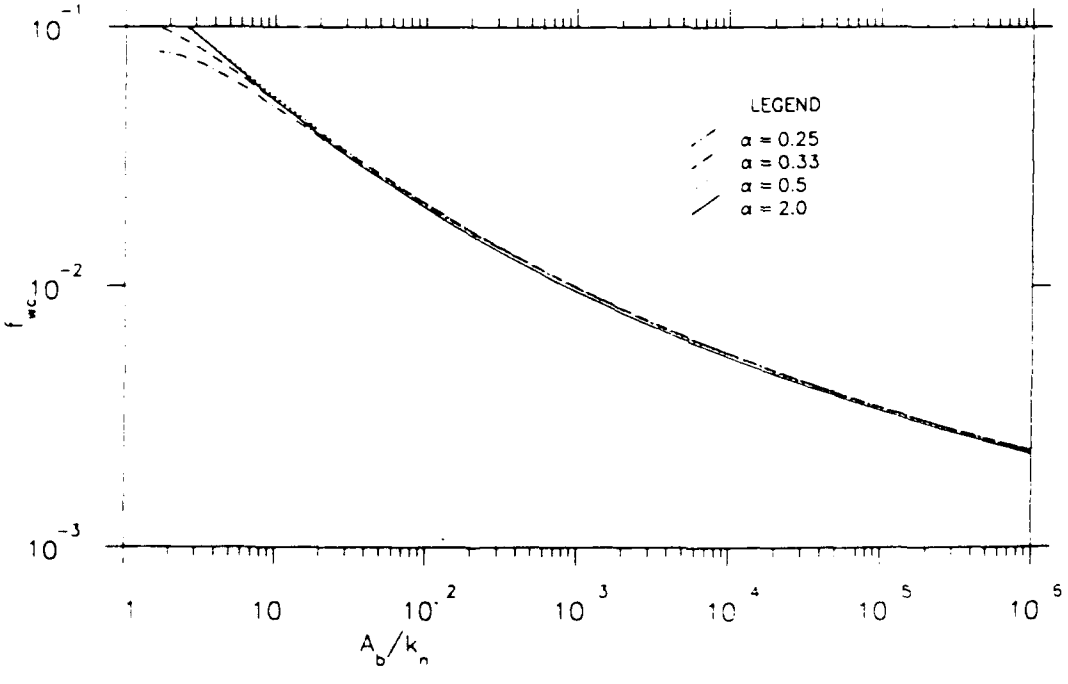

b. Friction factor diagram for $1 < A_b/k_n < 10^6$

Figure 14. Wave friction factor diagram (no current) for different α values

near-bottom region and up and invoking boundary and matching conditions in the process, the solution for the current is obtained.

217. For the near-bottom region, $z < a\delta$, within which the eddy viscosity varies linearly, the governing equation for the current becomes

$$\kappa u_{*cw} z \frac{du_c}{dz} = u_{*c}^2 \tag{134}$$

for which the solution, satisfying the no-slip condition at $z = z_0 = k_n/30$, is

$$u_c = \frac{u_{*c}}{u_{*cw}} \frac{u_{*c}}{\kappa} \ln \frac{z}{z_0} \tag{135}$$

218. For the intermediate region, $a\delta < z < a\delta/\epsilon$, the eddy viscosity is constant and the governing equation is

$$\kappa u_{*cw} a\delta \frac{du_c}{dz} = u_{*c}^2 \tag{136}$$

for which the solution is

$$u_c = \frac{u_{*c}}{u_{*cw}} \frac{u_{*c}}{\kappa} \left[\frac{z}{a\delta} - 1 + \ln \frac{a\delta}{z_0} \right] \tag{137}$$

The requirement of matching current velocity at $z = a\delta$ is used to determine the constant of integration obtained from integration of Equation 136.

219. In the outer region, $z > a\delta/\epsilon$, the eddy viscosity is again linear and results in a logarithmic velocity profile given by

$$u_c = \frac{u_{*c}}{\kappa} \left[\ln \left[\frac{z}{a\delta/\epsilon} \right] + C \right] \tag{138}$$

where z for convenience has been nondimensionalized by the level $a\delta/\epsilon$ at which the solution must match the solution given by Equation 137.

220. Performing this matching results in the determination of the constant C and a current velocity in the outer region given by

$$u_c = \frac{u_{*c}}{\kappa}\left[\ln\left(\frac{z}{a\delta/\epsilon}\right) + 1 + \frac{u_{*c}}{u_{*cw}}\left[\ln\frac{a\delta}{z_0} - 1\right]\right] \tag{139}$$

221. To avoid any misinterpretation of this result, it should be emphasized that Equation 139, although formally valid in the outer region, $z \geq a\delta/\epsilon$, is limited by the assumption of the validity of "the law of the wall." Thus, Equation 139 cannot be extended beyond a fraction of the current boundary layer thickness.

222. In the limit of a small current, i.e., $u_{*c} \ll u_{*cw}$, the last term inside the bracket of Equation 139 will be insignificant, and the velocity profile for large z will be given by

$$u_c \cong \frac{u_{*c}}{\kappa} \ln\left(\frac{z}{a\delta/e\epsilon}\right) \tag{140}$$

223. This equation is the same as that for a pure current, as in Equation 24, but with z_0 replaced by the value $z_0' = a\delta/e\epsilon$. In other words, the bottom roughness seen by the current is no longer given by z_0 but by z_0'. This is the apparent roughness discussed by Grant and Madsen (1979). It is scaled by δ, the wave boundary layer thickness, instead of by k_n, the equivalent roughness parameter. For a strong wave motion, δ may be much larger than k_n, leading to an apparent roughness that is much larger than what would be predicted from a knowledge of the bottom conditions.

224. In the limit of a very weak wave motion $\epsilon = u_{*c}/u_{*cw} \to 1$; therefore, Equation 139 reduces to Equation 24, which gives the profile for a pure current.

Comparison with Experimental Data

225. The results of the model developed in the preceding section will be compared with the same experimental data used in Part III.

Waves alone

226. In the GM model, the problem of a pure wave motion did not involve any free model parameter. For the present model, however, the parameter a can be varied, and the most suitable value chosen after comparison with the data. Figures 15, 16, and 17 present the model results using $a = 0.15$,

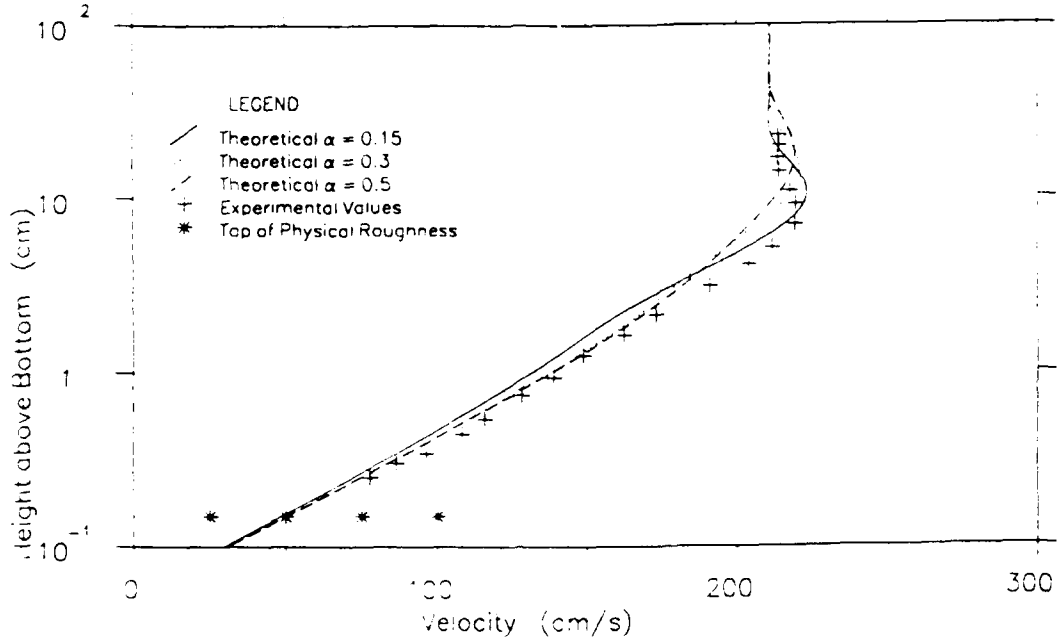

a. Wave velocity

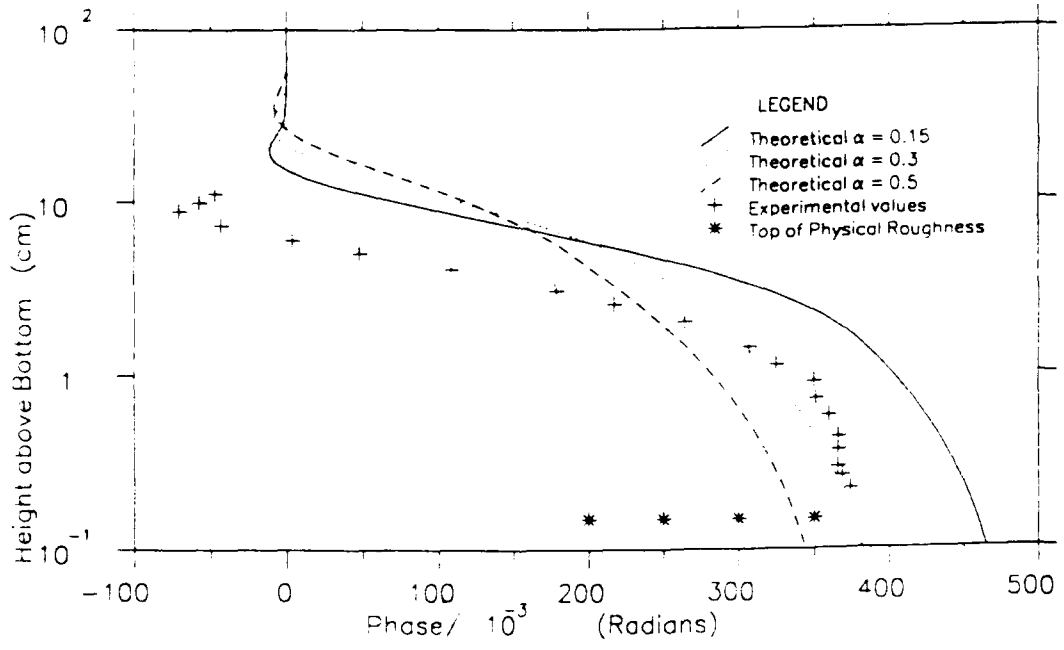

b. Phase

Figure 15. Comparison of the wave velocity and phase profiles of Jonsson and Carlsen (1976) Test 1 with the results of the improved model using three different values of α

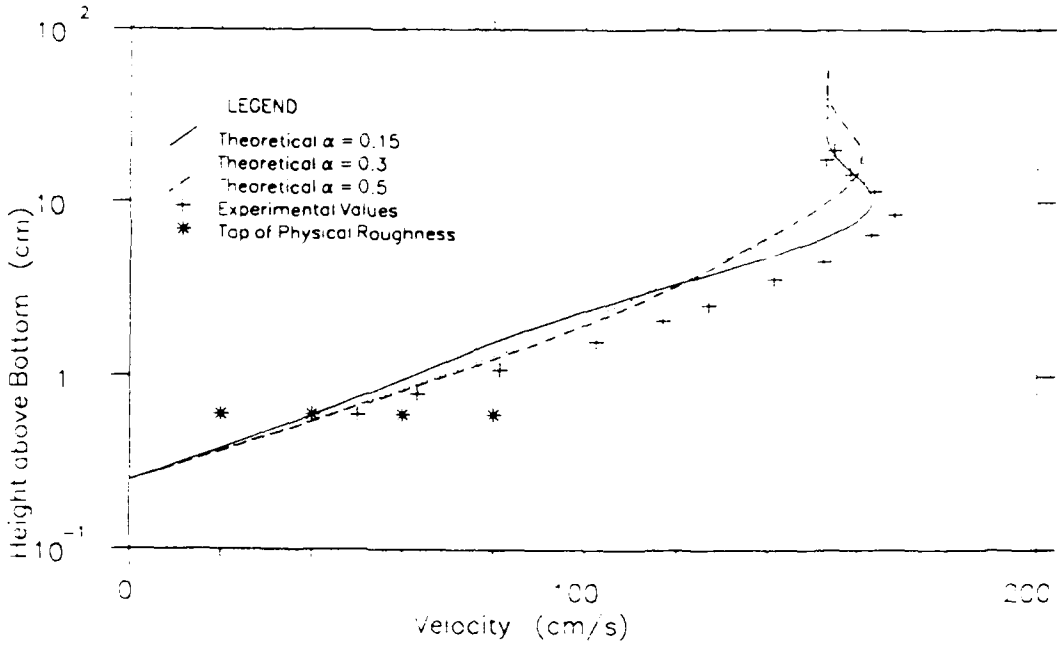

a. Wave velocity

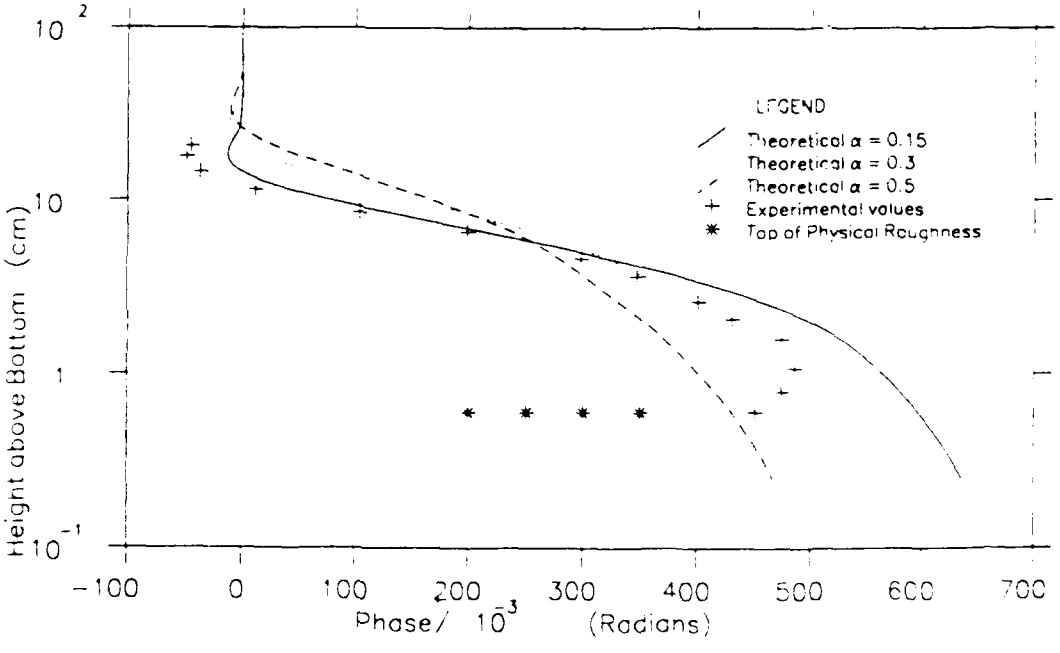

b. Phase

Figure 16. Comparison of the wave velocity and phase profiles of Jonsson and Carlsen (1976) Test 2 with the results of the improved model using three different values of α

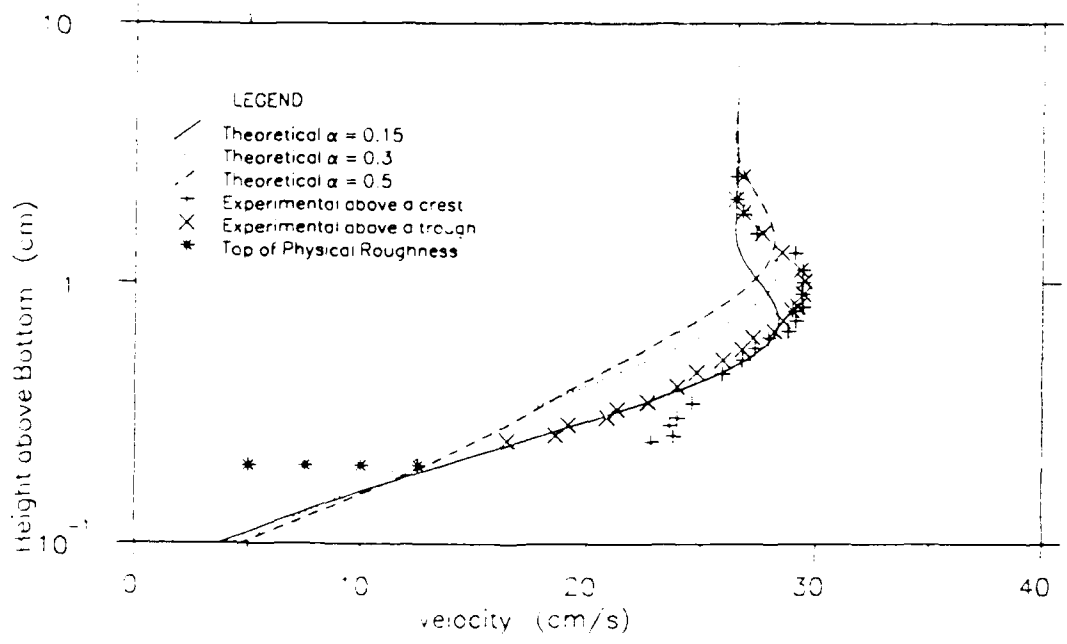

a. Wave velocity

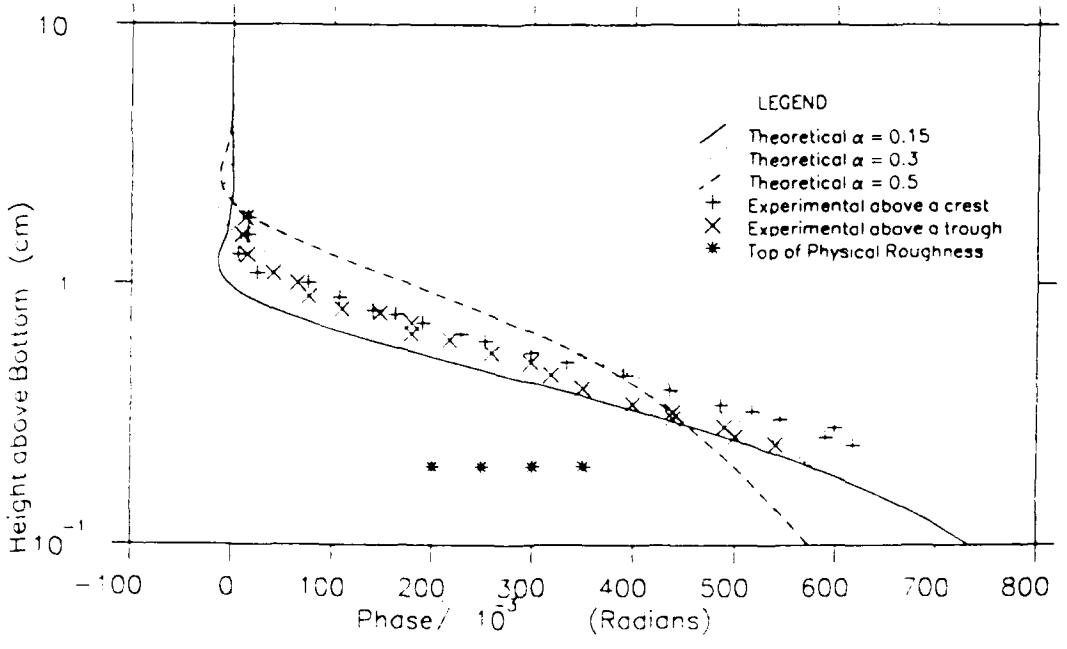

b. Phase

Figure 17. Comparison of the wave velocity and phase profiles from Van Doorn (1981) with the results of the improved model using three different values of α

$\alpha = 0.3$, and $\alpha = 0.5$ compared with the three data sets from the physical experiments. Figure 18 presents the comparison of the instantaneous wave velocity profiles of Davies, Soulsby, and King (1988) with the predicted profiles using $\alpha = 0.5$.

227. As shown in the figures, the predictions afforded by the present model are closer to the data than are those of the GM model in Figures 1, 2, 3, and 4. The boundary layer thickness, the level of the overshoot, and the magnitude of the overshoot are better represented. Figures 15, 16, and 17 show that the results with $\alpha = 0.15$ are the best with regard to these phenomena. This agrees with the results of Trowbridge and Madsen (1984a and 1984b).

228. However, when considering the flow close to the bottom, Figures 15 and 16 show that the profiles with $\alpha = 0.5$ and $\alpha = 0.3$ show significantly better agreement with the data than the profiles with $\alpha = 0.15$. Figure 18 shows a similar result with $\alpha = 0.5$ giving good agreement near the bottom, particularly when the velocity is a maximum, but performing less well near the top of the boundary layer. On the other hand, it is seen in Figure 17 that only the profile with $\alpha = 0.15$ fits the data near the bottom while none of the profiles does well towards the top of the boundary layer.

229. The maximum wave shear stresses and phase leads corresponding to the Davies, Soulsby, and King conditions for these values of α along with the results from the GM model are presented in Table 6. Considering the shear stress, it is seen that a value of α between 0.15 and 0.3 is indicated to fit the data. However, for these low values of α , the phase lead is too large with the value for the set DVW05 with $\alpha = 0.15$ being almost as much as that for laminar flow. The phase profiles from the physical data sets in Figures 15, 16, and 17 indicate that $\alpha = 0.3$ is the best value.

230. The above discussion shows that the indications from the comparisons for a pure wave motion regarding the optimum value of α are unclear. $\alpha = 0.5$ does well for the near-bottom region while $\alpha = 0.15$ does best for the top of the boundary layer.

Waves and currents

231. The comparison of the predicted current velocity profiles with the data is shown in Figures 19 and 20 using the values $\alpha = 0.15$ and 0.5 . It

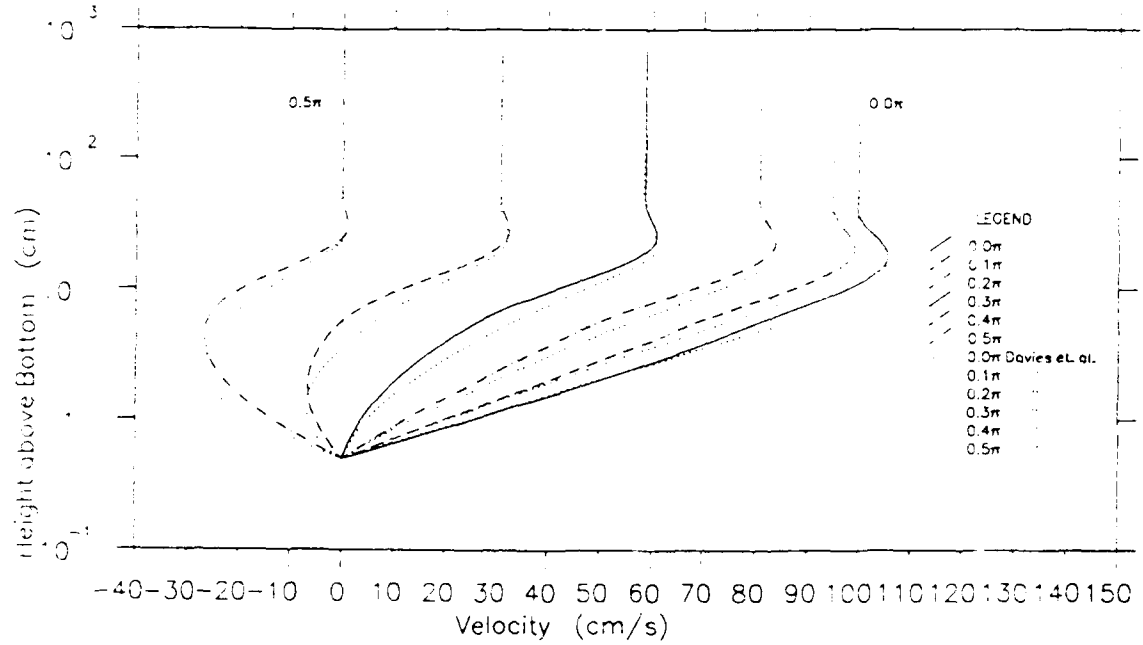

a. Wave velocity at phases $0-0.5\pi$

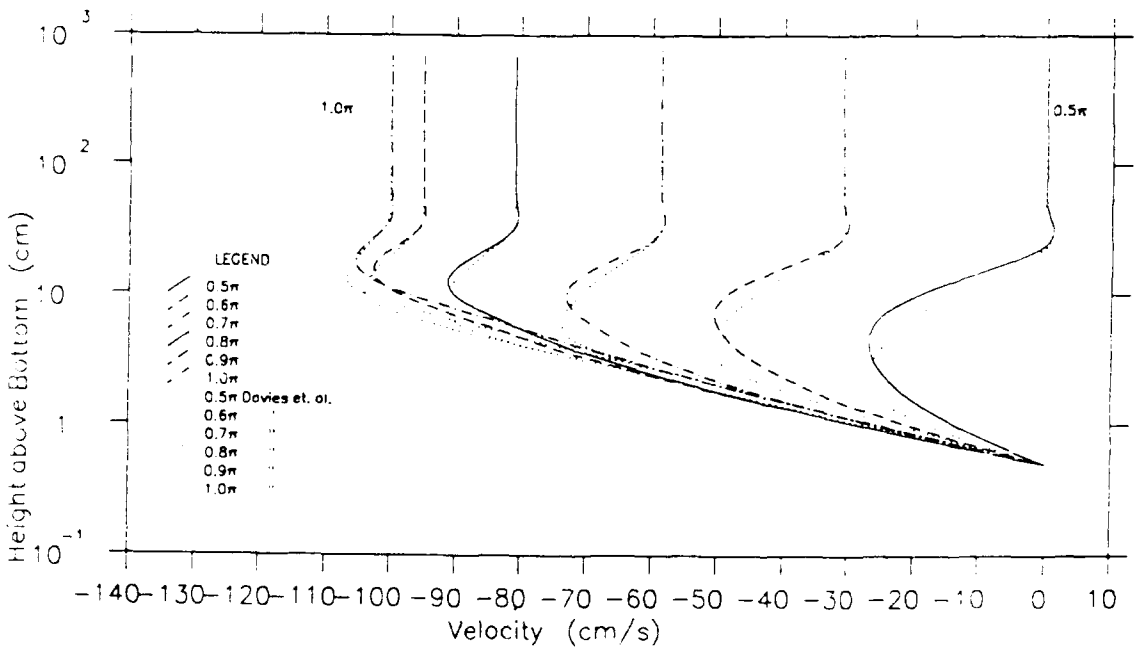

b. Wave velocity at phases $0.5\pi-\pi$

Figure 18. Comparison of the instantaneous wave velocity profile at various phases of the free stream velocity from Davies, Soulsby, and King (1988) with the results of the improved model a = 0.5

Table 6

Calculated Maximum Wave Shear Stress and Phase Lead for the Conditions of Davies, Soulsby, and King (1988) from the GM and the Improved Models Compared with the Results from Davies, Soulsby, and King (1988)

	Wave Shear Stress (Pa)					Phase Lead (deg)				
			Improved Model					Improved Model		
Data Set	Davies et al.	GM Model	α=0.15	α=0.3	α=0.5	Davies et al.	GM Model	α=0.15	α=0.3	α=0.5
DVW05	8.1	9.7	6.0	8.9	9.9	28.2	29.6	44.8	39.2	34.4
DVW10	23.5	27.8	21.0	27.2	28.9	26.4	27.5	42.0	35.2	31.0
DVW15	44.3	52.0	42.3	51.9	54.1	25.2	26.3	37.8	33.1	29.2

was found that $\alpha = 0.5$ resulted in a very good fit to all the data sets. It is particularly encouraging that a single value of α fits all three current profiles in Figure 20, which were for three different values of u_b. This is an improvement over the GM model for which, as shown in Figure 6, different values of γ are required to give a good fit to each profile.

232. The maximum shear stresses predicted for the Davies, Soulsby, and King conditions using the two values of α are presented in Table 7 along with the results from the GM model. It is seen that $\alpha = 0.5$ gives values that are very close to those from the GM model while the use of $\alpha = 0.15$ results in a lower shear stress. This is expected because as shown in the previous section, $\alpha = 0.15$ gives rise to lower wave shear stresses.

233. The maximum and current shear stresses predicted for the Bakker and Van Doorn conditions are given in Table 8 for the two values of α along with the results from the GM model using the "best fit" value of $\gamma = 1.0$. Use of $\alpha = 0.15$ leads to current shear stresses that are about 50 percent less than the values obtained with $\alpha = 0.5$. The effect of this decrease on the current profiles can be seen in Figure 19, where the slope of the profile in the outer region does not match the data.

234. However, as shown in Figure 21, the model is unable to fully represent the change in the profile caused by the change in ϕ_{cw} —the angle between the wave and current. It is seen, however, that the model

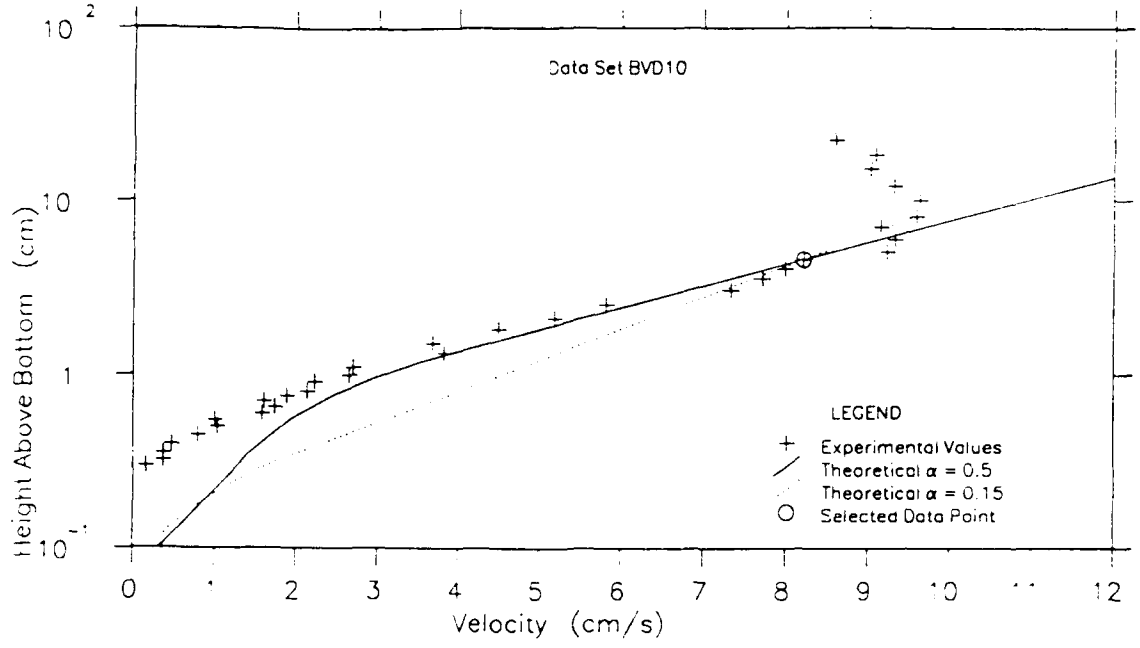

a. Data set BVD10

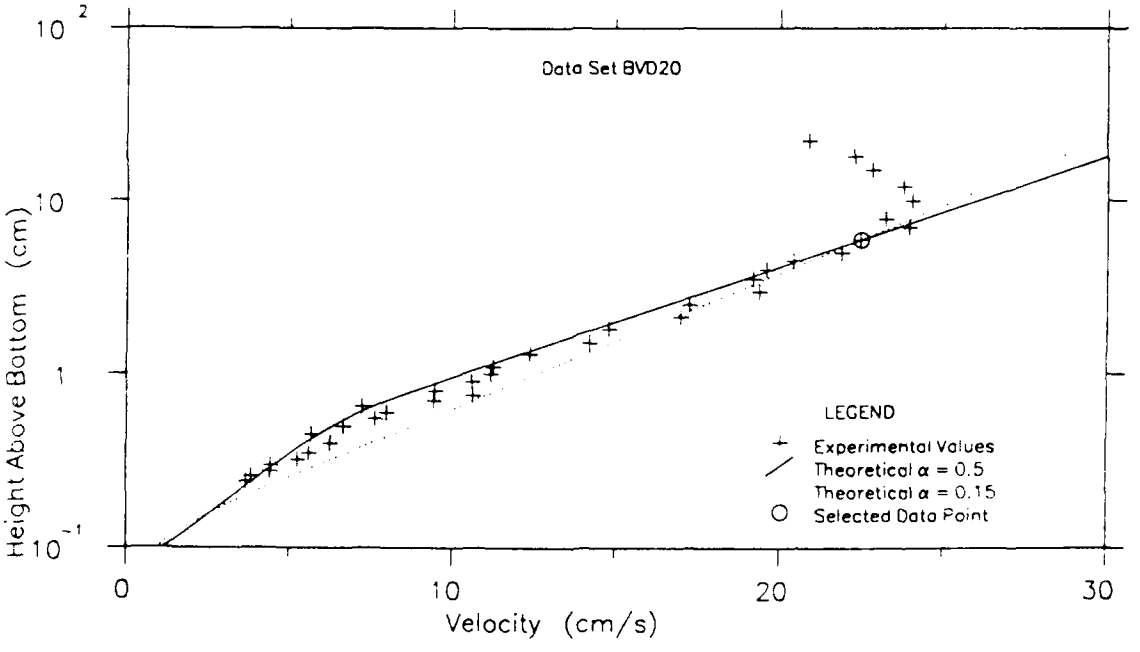

b. Data set BVD20

Figure 19. Comparison of the current velocity profiles from Bakker and Van Doorn (1978) with the results of the improved model with α = 0.15 and α = 0.5

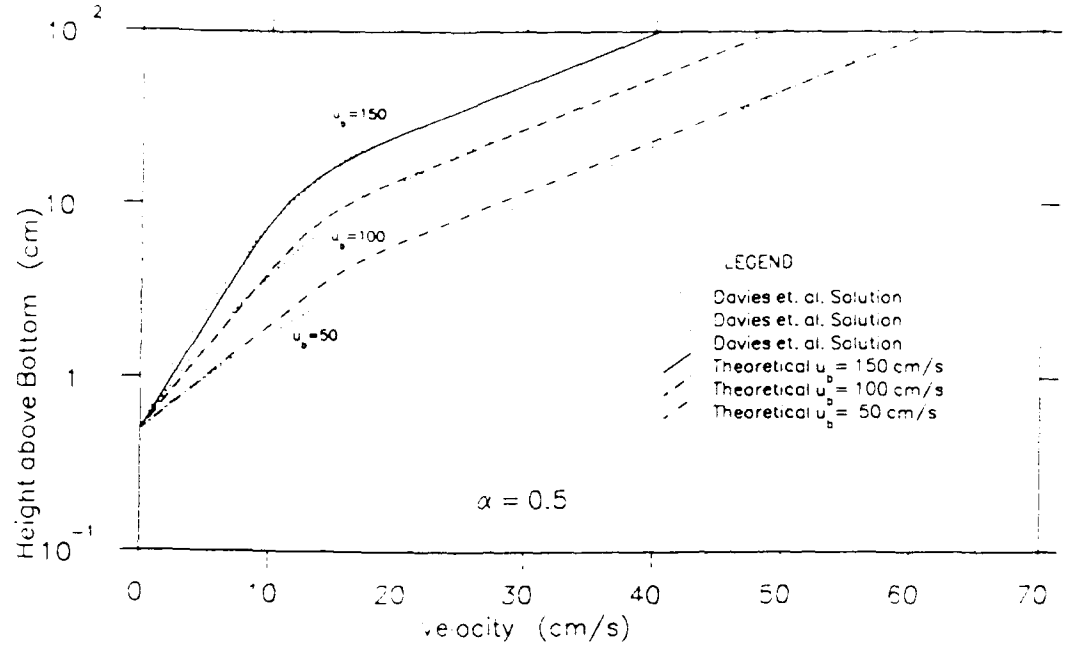

a. Comparison with α = 0.5

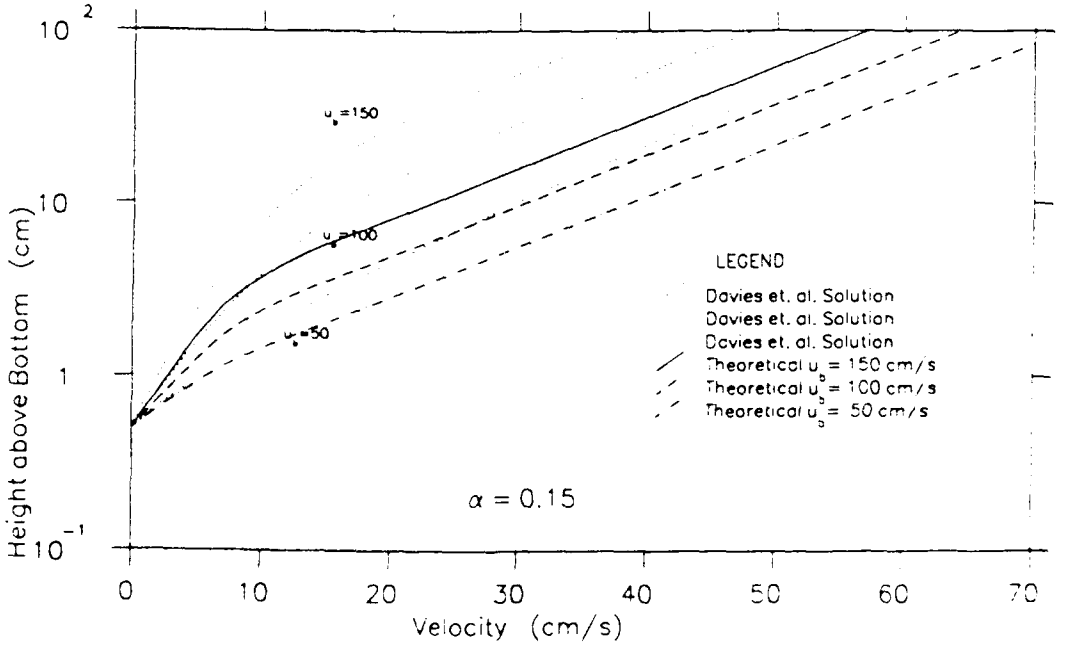

b. Comparison with α = 0.15

Figure 20. Comparison of the current velocity profiles from Davies, Soulsby, and King (1988) for waves and currents in the same direction with the results of the improved model with α = 0.15 and α = 0.5

Table 7

Calculated Maximum Bottom Shear Stress for the Conditions of Davies, Soulsby, and King (1988)

Data Set	Maximum Shear Stress (Pa)			
	Davies et al.	GM Model	Improved Model	
			a=0.15	a=0.5
DV0500	13.0	14.7	12.0	14.7
DV1000	28.0	33.1	26.0	34.0
DV1045	27.0	31.7	24.6	32.6
DV1090	24.2	28.2	21.0	29.1
DV1500	48.9	57.3	46.7	59.5

Table 8

Calculated Maximum and Current Shear Stresses for the Conditions of Bakker and Van Doorn from the Improved Model and the GM Model

Data Set	Current Shear Stress (Pa)			Maximum Shear Stress (Pa)		
	CM Model	Improved Model		GM Model	Improved Model	
	γ=1.0	a=0.15	a=0.5	γ=1.0	a=0.15	a=0.5
BVD10	0.18	0.093	0.19	2.9	1.7	3.0
BVD20	0.80	0.49	0.74	3.6	2.3	3.5

does perform marginally better than the GM model in this respect. For example, the difference in velocity between the case with $\phi_{cw} = 90^{\circ}$ and the case with $\phi_{cw} = 0$ in the outer region increases from 2.0 to 2.5 cm/sec. This, however, is still significantly less than the value of 8.5 cm/sec shown by the results of Davies, Soulsby, and King (1988).

Summary

235. All the comparisons with the experimental data show that the model is an improvement upon the GM model. The results obtained for a pure wave

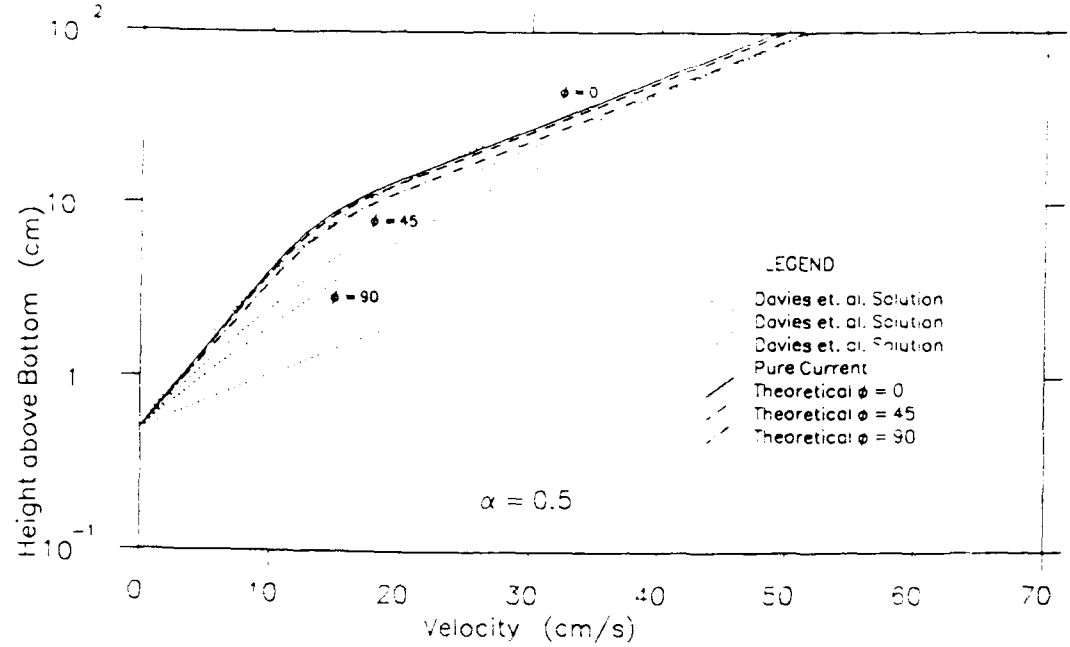

a. Comparison with $\alpha = 0.5$

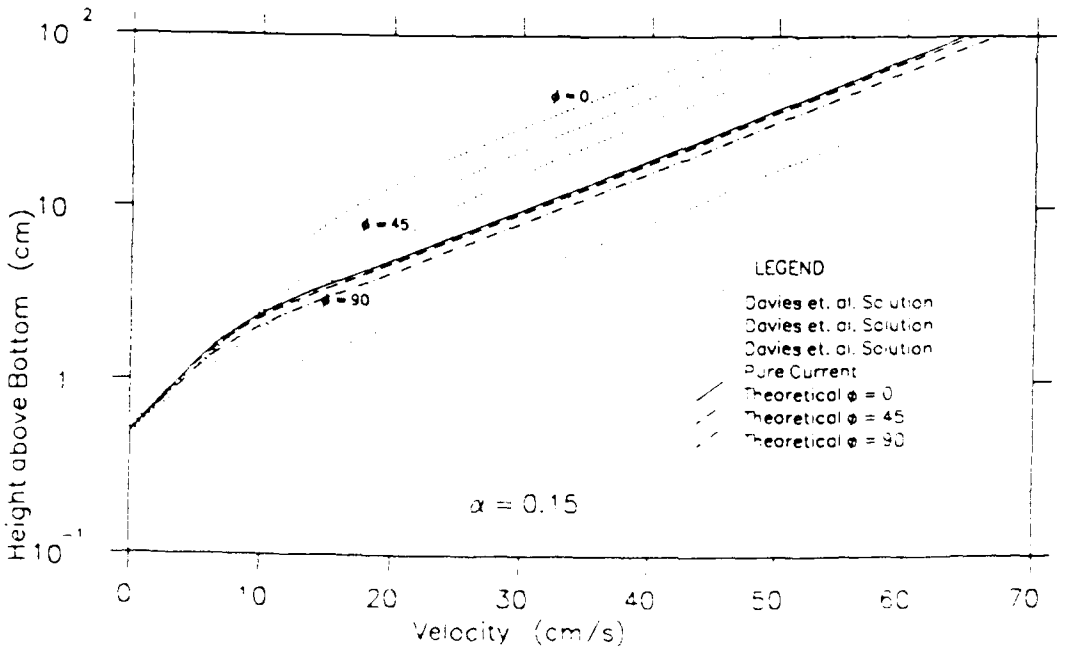

b. Comparison with $\alpha = 0.15$

Figure 21. Comparison of the current velocity profiles from Davies, Soulsby, and King (1988) for waves and currents at an angle with the results of the improved model with $\alpha = 0.15$ and $\alpha = 0.5$

motion reproduce the features of the experimental data better than the GM model. The generated current velocity profiles have a smooth transition between the wave boundary layer and the current boundary layer. The most important advance from the GM model is the fact that a single value of a fits all the data for current profiles in the case of co-directional waves and currents well.

236. However, the results for the comparison with the wave data suggest that a value of $a = 0.3$ or slightly less is the best for the wave problem while the comparisons with the current profiles strongly indicate $a = 0.5$ as the best value. The use of $a = 0.5$ does not result in very drastic changes to the values obtained in the wave problem and actually does better in predicting the near-bottom velocity in two data sets. The proportional change in the value of the overshoot is not very large when $a = 0.5$ is used in place of $a = 0.15$. On the other hand, use of a smaller value of a results in significant changes to the current velocity and shear stress as shown previously.

237. Bearing in mind that the near-bottom wave velocity is more important for application to sediment transport, it is proposed that $a = 0.5$ be selected as the value of the free parameter in this model. This value is expected to give good predictions for the current profiles when $\phi_{cw} = 0$ while not being very much in error for the wave velocity. There is, however, still a deficiency in the model's representation of waves and currents at an angle.

PART V: TIME-VARYING EDDY VISCOSITY MODEL

238. While the time-invariant eddy viscosity model developed in Part IV gave excellent results for a current velocity profile with waves in the same direction, it could not adequately represent the effect of a change in the angle between the waves and the current as shown in the data from Davies, Soulsby, and King (1988). The results of Davies, Soulsby, and King also show that the direction of the mean velocity when $0 < \phi_{cw} < 90^{\circ}$ is close to that of the mean shear stress only in the outer region, while the mean velocity closer to the bottom is deflected by the waves. These features are also apparent in the results of Van Kesteren and Bakker (1984).

239. The inability of the model to represent these features is a result of the simple formulation used. It was shown in Part II that once the eddy viscosity is assumed time-invariant, the linearized boundary layer equation can be separated into a wave and a current problem. Once this separation is accomplished, it can be seen that the wave velocity and the current velocity always lie along the direction of the free stream velocity and the mean shear stress, respectively, regardless of the sophistication of the eddy viscosity model used. This means that simply using a more elaborate time-invariant eddy viscosity model will not reproduce the phenomena discussed above. Instead it seems that an eddy viscosity that varies with time should be considered. This has been done in Trowbridge and Madsen (1984a, b) for a pure wave boundary layer, and they obtain features such as a third harmonic velocity in the boundary layer that are present in physical experiments but not obtainable if a time-invariant eddy viscosity is assumed.

240. Therefore in this Part a time-varying eddy viscosity model will be developed that has a form similar to that used in Trowbridge and Madsen (1984a, b). The assumption of a weak current is used to obtain tractable approximate governing equations for the waves and for the current. These are then solved, and the results compared with the experimental data.

Derivation of Approximate Equations for Waves and Current

241. The governing equation is the linearized boundary layer equation, derived in Part II, and identical to the one used in Part IV

$$\frac{\partial \vec{u}}{\partial t} = -\frac{1}{\rho}\nabla p + \frac{\partial}{\partial z}\left[\nu_t \frac{\partial \vec{u}}{\partial z}\right] \tag{141}$$

in which the shear stress (Reynolds stress) on horizontal planes has been expressed through the concept of a turbulent eddy viscosity

$$\frac{\vec{\tau}}{\rho} = \nu_t \frac{\partial \vec{u}}{\partial z} \tag{142}$$

242. While the separation of the governing equation, Equation 141, for the combined wave and current flow into its time-varying (wave) and time-invariant (current) components was readily achieved in Part II, due to ν_t being time-invariant, this separation is far more involved here since ν_t is considered a function of time.

243. To perform the separation the variables $\vec{u} = \{u,v\}$, p , and ν_t are expressed in terms of their time-dependent and time-independent contributions, denoted by tilde ($\tilde{}$) and overbar ($\bar{}$), respectively. Furthermore, since the wave motion is assumed simple periodic, the time-dependent contribution is split up into its even and odd harmonics, denoted by subscripts e , $(\tilde{})_e$, and o , $(\tilde{})_o$, respectively.

244. Introducing this notation, i.e.,

$$\begin{aligned} \vec{u} &= \{u,v\} = \{\bar{u},\bar{v}\} + \{\tilde{u}_e,\tilde{v}_e\} + \{\tilde{u}_o,\tilde{v}_o\} \\ p &= \bar{p} + \tilde{p}_e + \tilde{p}_o \\ \nu_t &= \bar{\nu} + \tilde{\nu}_e + \tilde{\nu}_o \end{aligned} \tag{143}$$

in Equation 141 and assuming, without loss in generality, the periodic waves to propagate in the x-direction, i.e., invoking $\tilde{p}_e = 0$ and $\partial\tilde{p}/\partial y = 0$, the x and y components of the governing equation become

$$\frac{\partial(\tilde{u}_e+\tilde{u}_o)}{\partial t} = -\frac{1}{\rho}\frac{\partial(\bar{p}+\tilde{p}_o)}{\partial x} + \frac{\partial}{\partial z}\left[(\bar{\nu} + \tilde{\nu}_e + \tilde{\nu}_o)\frac{\partial(\bar{u}+\tilde{u}_e+\tilde{u}_o)}{\partial z}\right]$$

$$\frac{\partial(\tilde{v}_e+\tilde{v}_o)}{\partial t} = -\frac{1}{\rho}\frac{\partial\bar{p}}{\partial y} + \frac{\partial}{\partial z}\left[(\bar{\nu} + \tilde{\nu}_e + \tilde{\nu}_o)\frac{\partial(\bar{v}+\tilde{v}_e+\tilde{v}_o)}{\partial z}\right] \tag{144}$$

245. To obtain the equation governing the time-independent (current) velocity, Equation 144 is time-averaged. Making use of the fact that only products of even or odd terms contribute to the time-average, this results in the equations

$$\frac{\partial}{\partial z}\left[\bar{\nu}\frac{\partial\bar{u}}{\partial z}\right] = \frac{1}{\rho}\frac{\partial\bar{p}}{\partial x} - \frac{\partial}{\partial z}\left[\overline{\tilde{\nu}_e\frac{\partial\tilde{u}_e}{\partial z}} + \overline{\tilde{\nu}_o\frac{\partial\tilde{u}_o}{\partial z}}\right]$$

$$\frac{\partial}{\partial z}\left[\bar{\nu}\frac{\partial\bar{v}}{\partial z}\right] = \frac{1}{\rho}\frac{\partial\bar{p}}{\partial y} - \frac{\partial}{\partial z}\left[\overline{\tilde{\nu}_e\frac{\partial\tilde{v}_e}{\partial z}} + \overline{\tilde{\nu}_o\frac{\partial\tilde{v}_o}{\partial z}}\right] \tag{145}$$

which, by comparison with Equation 51 of Part II, clearly bring out the wave-influence in the equations governing the current.

246. Subtracting Equation 145 from Equation 144 and collecting even and odd harmonics, the equations governing the time-dependent (wave) motion are obtained for the direction of wave propagation

$$\frac{\partial\tilde{u}_o}{\partial t} = -\frac{1}{\rho}\frac{\partial\tilde{p}_o}{\partial x} + \frac{\partial}{\partial z}\left[(\bar{\nu} + \tilde{\nu}_e)\frac{\partial\tilde{u}_o}{\partial z}\right] + \frac{\partial}{\partial z}\left[\tilde{\nu}_o\frac{\partial(\bar{u} + \tilde{u}_e)}{\partial z}\right] \tag{146}$$

$$\frac{\partial\tilde{u}_e}{\partial t} = \frac{\partial}{\partial z}\left[\tilde{\nu}_o\frac{\partial\tilde{u}_o}{\partial z} - \overline{\tilde{\nu}_o\frac{\partial\tilde{u}_o}{\partial z}}\right] + \frac{\partial}{\partial z}\left[\bar{\nu}\frac{\partial\tilde{u}_e}{\partial z}\right] + \frac{\partial}{\partial z}\left[\tilde{\nu}_e\frac{\partial\bar{u}}{\partial z}\right] + \frac{\partial}{\partial z}\left[\tilde{\nu}_e\frac{\partial\tilde{u}_e}{\partial z} - \overline{\tilde{\nu}_e\frac{\partial\tilde{u}_e}{\partial z}}\right] \tag{147}$$

and for the direction perpendicular to the wave direction

$$\frac{\partial\tilde{v}_o}{\partial t} = \frac{\partial}{\partial z}\left[(\bar{\nu} + \tilde{\nu}_e)\frac{\partial\tilde{v}_o}{\partial z}\right] + \frac{\partial}{\partial z}\left[\tilde{\nu}_o\frac{\partial(\bar{v} + \tilde{u}_e)}{\partial z}\right] \tag{148}$$

$$\frac{\partial \tilde{v}_e}{\partial t} = \frac{\partial}{\partial z}\left[\tilde{\nu}_o \frac{\partial \tilde{v}_o}{\partial z} - \overline{\tilde{\nu}_o \frac{\partial \tilde{v}_o}{\partial z}}\right] + \frac{\partial}{\partial z}\left[\bar{\nu}\frac{\partial \tilde{v}_e}{\partial z}\right] + \frac{\partial}{\partial z}\left[\tilde{\nu}_e \frac{\partial \bar{v}}{\partial z}\right]$$

$$+ \frac{\partial}{\partial z}\left[\tilde{\nu}_e \frac{\partial \tilde{v}_e}{\partial z} - \overline{\tilde{\nu}_e \frac{\partial \tilde{v}_e}{\partial z}}\right] \tag{149}$$

247. In passing it is noted, by comparison with Equation 48, that the time-independent current velocity appears explicitly in the equations governing the wave motion.

Weak current assumption

248. To further simplify the governing equations derived above, the assumptions of a weak current, expressed through the smallness of the parameter

$$\mu = \frac{u_{*c}}{u_{*w}} < 1 \tag{150}$$

also used in Part II, without restrictions on its magnitude, is introduced.

249. Since the flow in the immediate vicinity of the bottom scales with the ratio of the shear stresses, it follows that

$$\frac{\{\bar{u}, \bar{v}\}}{\tilde{u}_o} = O\left[\frac{\tau_c}{\tau_w}\right] = O(\mu^2) \tag{151}$$

where $\tilde{u}_o$, the odd harmonic wave velocity, is used to represent the wave velocity since this is expected to be the leading term for a simple harmonic wave motion.

250. As argued by Trowbridge and Madsen (1984a) and in Part II, the time-varying eddy viscosity should, in the immediate vicinity of the bottom, be related to the shear velocity based on the instantaneous (time-varying) bottom shear stress, $\tau_b(t)$, i.e.,

$$u_* = u_*(t) = \sqrt{|\tau_b(t)|/\rho} \tag{152}$$

251. For a periodic wave motion, u_* given by Equation 152 will result in a shear velocity consisting of only even harmonics (including a constant time-invariant contribution). The addition of a small steady shear stress

on top of the periodic wave shear stress will produce an asymmetry between the magnitude of the bottom shear stress associated with wave crest and trough. This asymmetry will, as demonstrated by Trowbridge and Madsen (1984b), result in odd harmonics appearing in the temporal variation of u_* .

252. Based on the preceding arguments, it is therefore reasonable to assume—subject to later verification—that the terms in the eddy viscosity expansion given by Equation 143 are related according to

$$\frac{\tilde{\nu}_e}{\bar{\nu}} = O(\beta)$$

$$\frac{\tilde{\nu}_0}{\bar{\nu}} = O(\mu^2) \tag{153}$$

where β is of the order 0.4 (Trowbridge and Madsen 1984a).

253. Using the rough order-of-magnitude estimates presented above comparison of the first two terms on the right-hand side of Equation 147 suggests

$$\frac{\tilde{u}_e}{\tilde{u}_0} = O(\mu^2) \tag{154}$$

Approximate equation for the wave problem

254. Applying order-of-magnitude arguments based on the preceding estimates to Equation 146 reveals that the last term in Equation 146 is of the order $\mu^4/\beta \ll 1$ relative to the smallest of the remaining terms, $\tilde{\nu}_e \, \partial\tilde{u}_0/\partial z$, which is of the order β . The equation governing the odd harmonic wave motion in the direction of wave propagation may therefore be taken as

$$\frac{\partial\tilde{u}_0}{\partial t} = -\frac{1}{\rho}\frac{\partial\tilde{p}_0}{\partial x} + \frac{\partial}{\partial z}\left[(\bar{\nu} + \tilde{\nu}_e)\frac{\partial\tilde{u}_0}{\partial z}\right] \tag{155}$$

which is identical to the equation solved by Trowbridge and Madsen (1984a) for a pure wave motion.

255. Similarly, the last two terms on the right-hand side of Equation 147 are seen to be of order $\beta < 1$ relative to the remaining terms, which are of order μ^2. Thus, the even harmonic wave problem in the direction of wave propagation may be approximated by

$$\frac{\partial \tilde{u}_e}{\partial t} = \frac{\partial}{\partial z}\left[\tilde{\nu}_0 \frac{\partial \tilde{u}_0}{\partial z} - \overline{\tilde{\nu}_0 \frac{\partial \tilde{u}_0}{\partial z}}\right] + \frac{\partial}{\partial z}\left[\bar{\nu}\frac{\partial \tilde{u}_e}{\partial z}\right] \tag{156}$$

256. As mentioned, the smallest term retained in the odd wave problem, Equation 155, is of order β relative to the leading, O(1), terms while the entire expression for the even wave problem, Equation 156, is of order μ^2, i.e., considerably smaller than the smallest term retained in Equation 155. It is therefore consistent, as a first approximation, to disregard the even wave problem.

257. For the wave motion perpendicular to the direction of wave propagation the forcing terms are associated with the current, i.e., $\tilde{\nu}_0 \, \partial \bar{v}/\partial z$ and $\tilde{\nu}_e \, \partial \bar{v}/\partial z$ in Equations 148 and 149, respectively. It follows from this that

$$\frac{\tilde{v}_0}{\tilde{u}_0} = O(\mu^4)$$

$$\frac{\tilde{v}_e}{\tilde{u}_0} = O(\beta\mu^2) \tag{157}$$

258. It is therefore entirely consistent with previous approximations and not surprising that the wave motion within the boundary layer in the direction perpendicular to the direction of wave propagation is negligibly small.

Approximate equations for the current problem

259. Applying order-of-magnitude arguments to the equations governing the time-independent (current) problem, Equation 145, shows that these may be approximated by

$$\frac{\partial}{\partial z}\left[\bar{\nu}\frac{\partial \bar{u}}{\partial z}\right] = \frac{1}{\rho}\frac{\partial \bar{p}}{\partial x} - \frac{\partial}{\partial x}\left[\overline{\tilde{\nu}_0 \frac{\partial \tilde{u}_0}{\partial z}}\right] \tag{158}$$

$$\frac{\partial}{\partial z}\left[\bar{\nu}\frac{\partial \bar{v}}{\partial z}\right] = \frac{1}{\rho}\frac{\partial \bar{p}}{\partial y} \tag{159}$$

where terms neglected are at most of order β relative to those retained.

260. Integration of Equations 158 and 159 from the bottom, $z \to 0$, to the outer edge of the wave boundary layer, $z = \delta$, gives

$$\left[\bar{\nu}\frac{\partial \bar{u}}{\partial z}\right]_{z\to 0}^{\delta} = \frac{1}{\rho}\frac{\partial \bar{p}}{\partial x}\delta - \left[\overline{\tilde{\nu}_0\frac{\partial \tilde{u}_0}{\partial z}}\right]_{z\to 0}^{\delta} \tag{160}$$

$$\left[\bar{\nu}\frac{\partial \bar{v}}{\partial z}\right]_{z\to 0}^{\delta} = \frac{1}{\rho}\frac{\partial \bar{p}}{\partial y}\delta \tag{161}$$

261. At the outer edge of the wave boundary layer, $z = \delta$, the wave motion will not contribute to the shear stress since here $\partial\tilde{u}_0/\partial z = \partial u_\infty/\partial z \simeq 0$. Also, the contribution of the mean pressure gradient term is vanishingly small so long as δ is well within the current boundary layer sale, in which case the law of the wall may be applied to the current problem. At the outer edge of the wave boundary layer, the following relations therefore hold

$$\bar{\nu}\left\{\frac{\partial \bar{u}}{\partial z}, \frac{\partial \bar{v}}{\partial z}\right\}_{z\to\delta} = \frac{\vec{\tau}_c}{\rho} = u_{*c}^2\{\cos\phi_{cw}, \sin\phi_{cw}\} \tag{162}$$

where $\vec{\tau}_c$, the current bottom shear stress vector, is assumed to be at an angle ϕ_{cw} to the direction of wave propagation.

262. In the immediate vicinity of the bottom, $z \to 0$, Equations 160 and 161 may therefore be written as

$$\bar{\nu}\frac{\partial \bar{u}}{\partial z} = u_{*c}^2\cos\phi_{cw} - \overline{\tilde{\nu}_0\frac{\partial \tilde{u}_0}{\partial z}} \tag{163}$$

$$\bar{\nu}\frac{\partial \bar{v}}{\partial z} = u_{*c}^2\sin\phi_{cw} \tag{164}$$

which constitute the equations governing the current in the direction and perpendicular to the direction of wave propagation.

263. It is of particular interest to note that the time-varying eddy viscosity formulation, in contrast to the time-invariant eddy viscosity formulation of Part IV, gives rise to a difference between the equation governing the current velocity components.

Eddy Viscosity Formulation

264. Other than relating the scale of the eddy viscosity to that of the shear velocity, Equation 152, for the purpose of rough order-of-magnitude estimates, nothing has been said about its functional form up to now. To be more specific about the eddy viscosity formulation to be used in the solution of the wave and current problem, it is assumed that the eddy viscosity may be expressed as a product of two terms—one accounting for the temporal, the other for the spatial variability.

265. It is therefore assumed that

$$\nu_t = g(z) \cdot f(t) \tag{165}$$

where f(t) is obtained from the temporal variation of the instantaneous shear velocity, $u_*(t) = \sqrt{|\vec{\tau}_b(t)/\rho}$.

266. Commensurate with the weak current assumption, the instantaneous bottom shear stress vector is assumed given by

$$\vec{\tau}_b = \{\tilde{\tau}_1 \cos\theta + \tau_c \cos\phi_{cw},\ \tau_c \sin\phi_{cw}\} \tag{166}$$

where τ_1 is the magnitude of the first harmonic shear stress at the bottom, θ is the phase of the wave, ωt, plus some arbitrary phase angle, and terms involving even harmonics in the shear stress have been neglected following the argument justifying that the even wave problem, given by Equation 156, need not be solved.

267. To obtain the magnitudes of the instantaneous shear stress from Equation 166 only terms linear in τ_c are retained since $\tau_c/\tilde{\tau}_1 = O(\mu^2)$. Therefore

$$|\vec{\tau}_b| = \tau_b = \{\vec{\tau}_1^2\cos^2\theta + 2\tilde{\tau}_1\tau_c\cos\phi_{cw}\cos\theta\}^{\frac{1}{2}} = \tilde{\tau}_1|\cos\theta|\left\{1 + 2\frac{\tau_c\cos\phi_{cw}}{\tilde{\tau}_1\cos\theta}\right\}^{\frac{1}{2}} \quad (167)$$

268. The square root in this expression may be expanded treating the τ_c -term as small relative to unity. This assumption is clearly violated during a short time interval around $\cos\theta = 0$; however, for most of the wave period, the assumption is a good one, and when it is violated, the resulting term is indeed small. Therefore, formal expansion of Equation 167 yields

$$\frac{\tau_b}{\rho} = u_*^2 \approx u_{*1}^2|\cos\theta|\left\{1 + \frac{\tau_c\cos\phi_{cw}}{\tilde{\tau}_1\cos\theta}\right\} \quad (168)$$

269. To obtain an expression for the instantaneous shear velocity in terms of a harmonic expansion, as assumed in Equation 143, use is made of the Fourier expansions

$$\begin{aligned} |\cos\theta| &= \frac{2}{\pi}\left[1 + \frac{2}{3}\cos 2\theta + \cdots\right] \\ \frac{|\cos\theta|}{\cos\theta} &= \frac{4}{\pi}(cc \quad + \cdots) \end{aligned} \quad (169)$$

which introduced in Equation 168 yields

$$u_*^2 = \frac{2}{\pi}u_{*1}^2\left[1 + \frac{2}{3}\cos 2\theta + 2\frac{\tau_c\cos\phi_{cw}}{\tilde{\tau}_1}\cos\theta\right] \quad (170)$$

and therefore approximately

$$u_* = \sqrt{\frac{2}{\pi}}u_{*1}\left[1 + \frac{1}{3}\cos 2\theta + \frac{\tau_c\cos\phi_{cw}}{\tilde{\tau}_1}\cos\theta\right] \quad (171)$$

This equation can be written as

$$\frac{u_*}{u_{*1}} = \sqrt{\frac{2}{\pi}} + \mu^2\cos\phi_{cw} \cdot \sqrt{\frac{2}{\pi}}\cos\theta + \frac{1}{3}\sqrt{\frac{2}{\pi}}\cos 2\theta \quad (172)$$

and the exact value of u_*/u_{*1} is obtained from Equation 167 as

$$\frac{u_*}{u_{*1}} = (\cos^2\theta + 2\mu^2\cos\phi_{cw}\cos\theta + \mu^4)^{\frac{1}{4}} \tag{173}$$

270. Equation 172 gives an approximation to Equation 167 in terms of a constant and first- and second-harmonic terms. The "best fit" values of the three coefficients in this expansion can alternatively be obtained from a Fourier expansion of Equation 173.

271. Figure 22 shows the approximate expansion in Equation 172 compared with the exact expression from Equation 167 and to a "best fit" curve drawn using the first three coefficients of a Fourier cosine expansion of Equation 173, using two different values of μ and ϕ_{cw} .

272. The approximate expansion is fairly close to the exact value even at these very large values of μ For the case with $\phi_{cw} = 0$, the approximation does worst when the exact value is near zero. However, because of the persistence of turbulent fluctuation, it is physically unrealistic to expect the eddy viscosity to vanish during the cycle, and this failure is therefore not considered a serious shortcoming of the approximation.

273. The use of the "best-fit" coefficient improves the approximation, particularly for the case with $\phi_{cw} = 90$. However, these coefficients must be calculated for each case numerically; therefore, the expansion with the final coefficients in Equation 172 is considered sufficiently accurate for the purposes of the present study.

274. With the temporal variation of the instantaneous shear velocity given by Equation 171 and choosing the spatial variation used for the time-invariant eddy viscosity model in Part IV results in the following time-varying eddy viscosity model

$$\nu_t = \begin{cases} \kappa u_* z & z \le a_1\delta \\ \kappa u_* a_1\delta & a_1\delta \le z \le \sqrt{\frac{2}{\pi}}a_1\delta/\epsilon \\ \kappa u_{*c} z & z \ge \sqrt{\frac{2}{\pi}}a_1\delta/\epsilon \end{cases} \tag{174}$$

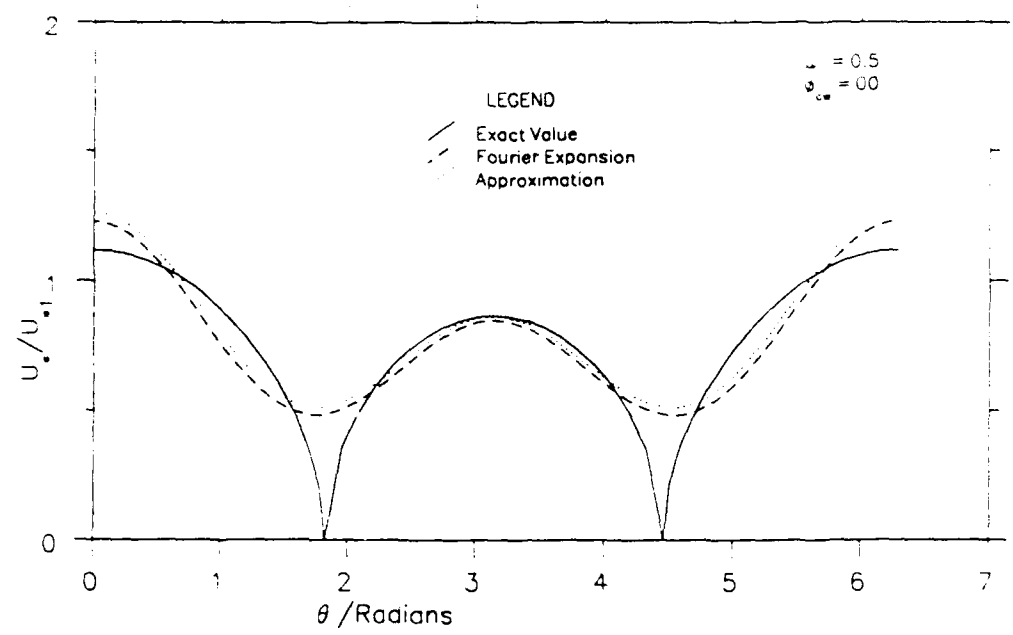

a. Comparison with $\mu = 0.5$, $\phi_{cw} = 0°$

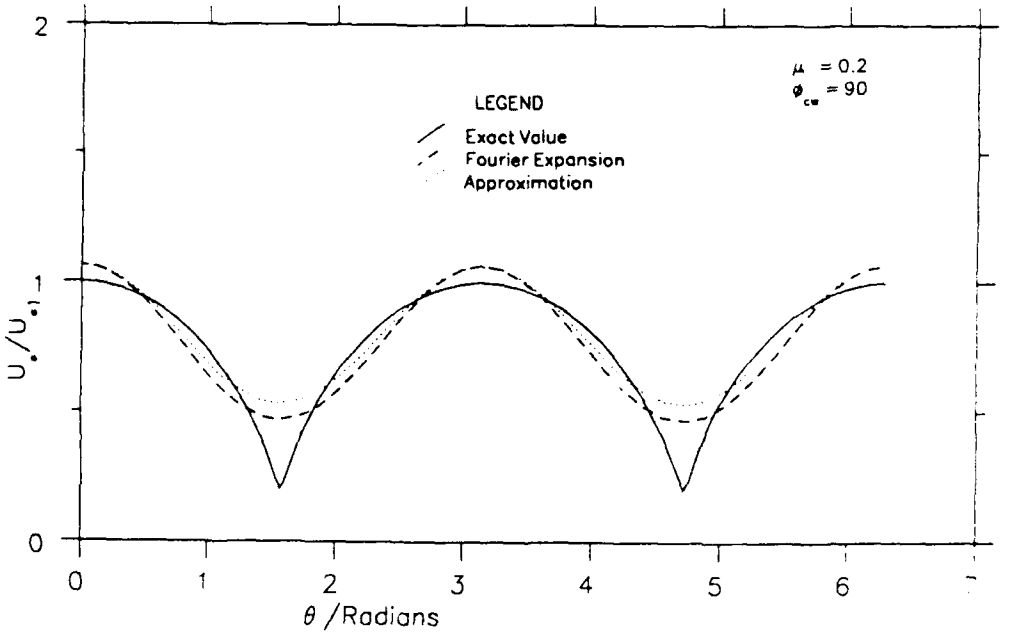

b. Comparison with $\mu = 0.2$, $\phi_{cw} = 90°$

Figure 22. Comparison of the approximate expansion of the eddy viscosity in Equation 32 with the exact value in Equation 33 and the three-term Fourier expansion

with u_* given by Equation 171 and the definitions of δ and ϵ being the same as those introduced in Part IV with the appropriate modification due to the weak current assumption. For example $u_{*cw} \simeq u_{*1}$ since the current is weak so that $\epsilon = \mu \ll 1$ and $\delta = \kappa u_{*1}/\omega$. As in the time-invariant model, a_1 is a free model parameter that is determined after comparison with the experimental data.

275. In the time-invariant eddy viscosity model of Part IV, the eddy viscosity in the wave boundary layer was scaled by u_{*cw}, which was derived from the maximum shear stress. This ensures that the slope of the eddy viscosity profile in the lower region $z_0 < z < a\delta$ is greater than that in the outer region.

276. For the time-varying model outlined above, however, it is seen that the slope of the mean eddy viscosity profile is greater in the wave boundary layer only if

$$\mu = \frac{u_{*c}}{u_{*1}} < \sqrt{\frac{2}{\pi}} \tag{175}$$

which means that the use of the present model, derived for small μ, is limited by the condition given by Equation 175.

277. The level of the transition from an eddy viscosity scaled by the wave shear velocity to one scaled by the current shear velocity in Equation 174 is chosen so that the mean eddy viscosity is continuous. This results in a discontinuity in the instantaneous eddy viscosity at this level because the eddy viscosity above it is considered time invariant, while that below varies with time. The time-varying eddy viscosity is due to the wave motion; therefore, a more logical place to cut off the time variation would be the top of the wave boundary layer, i.e., at $z = \delta$. The wave problem could then be solved for a time-varying eddy viscosity below $z = \delta$ and a time-invariant eddy viscosity above this level with the solutions matched at this level. This procedure would, however, be cumbersome to implement. In practice it is found that the assumed form of the eddy viscosity above the level $z = \delta$ does not have much effect on the wave solution. For the solution of the wave problem, it is therefore assumed that the eddy viscosity variation is as given in Equation 174 but with the time variation assumed to be present in the upper region as well. As will

be seen, this makes the solution far less complicated than the procedure outlined above while not being much in error so long as the level $z = \sqrt{2/\pi}a_1\delta/\mu$ is greater than the level $z = \delta$, This condition will be satisfied when

$$\epsilon = \mu < \sqrt{\frac{2}{\pi}}a_1 \tag{176}$$

278. Before proceeding with the solution to the wave and current problem inspection of Equation 171 in conjunction with Equation 172 shows that the assumption regarding the order of magnitude of the eddy viscosity components made in Equation 153 indeed are correct with $\beta = \frac{1}{3}$ being small—although not very small—relative to unity.

Wave Problem

279. The equation governing the wave problem is given by Equation 155 and may alternatively be expressed in terms of the velocity deficit

$$\tilde{u}_d = \frac{\tilde{u}_0 - u_\infty}{u_b} \tag{177}$$

where $u_\infty \neq u_\infty(z)$ is the near-bottom velocity predicted by linear potential wave theory, i.e., governed by

$$\frac{\partial u_\infty}{\partial t} = -\frac{1}{\rho}\frac{\partial \tilde{p}_0}{\partial x} \tag{178}$$

280. Introducing these expression in Equation 155, this equation becomes

$$\frac{\partial \tilde{u}_d}{\partial t} = \frac{\partial}{\partial z}\left[\bar{\nu}\left[1 + \frac{\tilde{\nu}_e}{\bar{\nu}}\right]\frac{\partial \tilde{u}_d}{\partial z}\right] \tag{179}$$

where

$$1 + \frac{\tilde{\nu}_e}{\bar{\nu}} = 1 + \frac{1}{3}\cos 2(\omega t + \phi_2) \tag{180}$$

is obtained from Equations 171 and 172.

281. By introducing a change in the time-variable from t to $\tilde{t}$ defined by

$$\frac{\partial \tilde{t}}{\partial t} = 1 + \frac{1}{3}\cos 2(\omega t + \phi_2) \tag{181}$$

or

$$\omega \tilde{t} = \omega t + \frac{1}{6}\sin 2(\omega t + \phi_2) \tag{182}$$

the equation governing the wave motion becomes

$$\frac{\partial \tilde{u}_d}{\partial \tilde{t}} = \frac{\partial}{\partial z}\left[\bar{\nu}\frac{\partial \tilde{u}_d}{\partial z}\right] \tag{183}$$

which is identical to the equation governing the time-invariant eddy viscosity formulation of the wave problem, except that the time-invariant eddy viscosity in Equation 183 is based on the average shear velocity rather than the maximum shear velocity used in Part IV.

282. To solve Equation 183, it is necessary to specify the no-slip boundary condition at the bottom

$$\tilde{u}_d = \frac{-u_\infty}{u_b} = -\cos\omega t \tag{184}$$

in terms of the new time-variable, $\tilde{t}$.

283. From Equation 182, treating the factor of (1/6) in front of the cyclic term as small, the first-order relationship is that $\omega t = \omega \tilde{t}$, which may be introduced in the cyclic term to obtain

$$\omega t \simeq \omega \tilde{t} - \frac{1}{6}\sin 2(\omega \tilde{t} + \phi_2) \tag{185}$$

284. Substituting Equation 185 for ωt in Equation 184 and expanding the resulting expression around $\omega \tilde{t}$, consistent with the degree of

approximation adopted in Equation 185, yields the boundary condition to be satisfied for $z \to 0$

$$\tilde{u}_d = -\cos\left[\omega\tilde{t} - \frac{1}{6}\sin 2(\omega\tilde{t} + \phi_2)\right] = -\left\{\cos\omega\tilde{t} + \sin\omega\tilde{t}\left[\frac{1}{6}\sin 2(\omega\tilde{t} + \phi_2)\right]\right\}$$
$$= -\left[\cos\omega\tilde{t} + \frac{1}{12}\cos(\omega\tilde{t} + 2\phi_2) - \frac{1}{12}\cos(3\omega\tilde{t} + 2\phi_2)\right] \qquad (186)$$

285. The approximation to $\cos(\omega t)$ is plotted in Figure 23 along with the exact value for $\phi_2 = 30^\circ$. It is seen from the figure that Equation 186 is an excellent approximation to Equation 184 for this value of ϕ_2, which is chosen to be in the range encountered in practice.

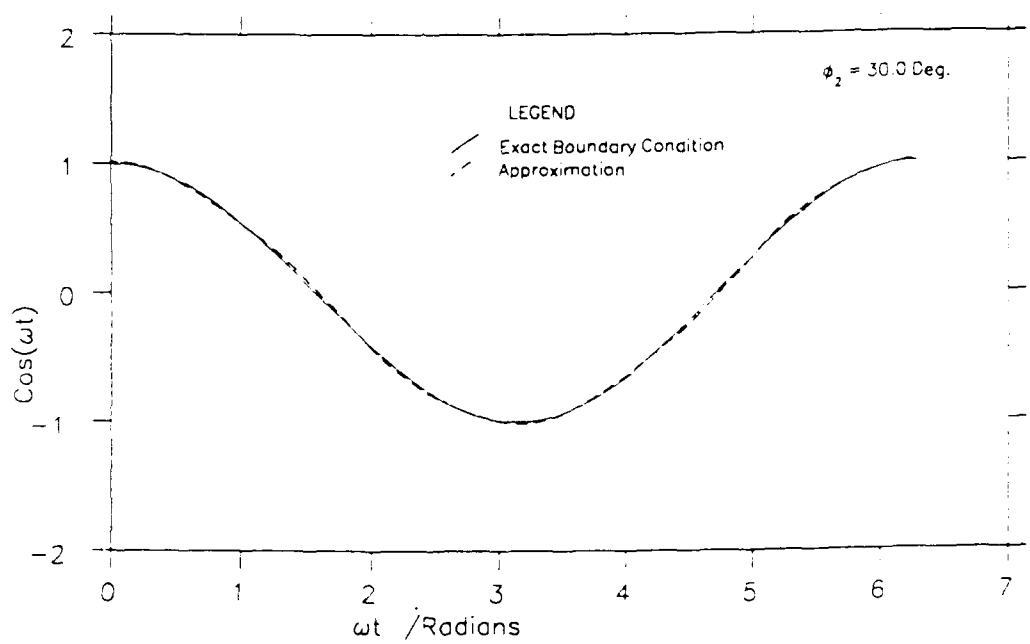

Figure 23. Comparison of the approximate boundary condition of Equation 186 with the exact value for $\phi_2 = 30^\circ$

286. The occurrence of third harmonics in the boundary condition indicates that the solution will contain this harmonic in addition to the fundamental harmonic motion. Since Equation 183 and its boundary condition Equation 186 are linear, a solution of the form

$$\tilde{u}_d = \mathrm{Re}\left[u_{d1}e^{i\omega\tilde{t}} + u_{d2}e^{i(\omega\tilde{t}+2\phi_2)} + u_{d3}e^{i(3\omega\tilde{t}+2\phi_2)}\right] \tag{187}$$

is assumed. This ensures that Equation 186 is satisfied if

$$u_{d1} = -1 \ , \quad u_{d2} = -\frac{1}{12} \ , \quad u_{d3} = \frac{1}{12} \qquad \text{at} \qquad z = z_0 \tag{188}$$

is imposed as a boundary condition on each part of the solution. The other boundary condition is

$$u_{d1} \ , \quad u_{d2} \ , \quad u_{d3} \rightarrow 0 \qquad \text{as} \qquad z \rightarrow \infty \tag{189}$$

287. Now the solution for each of the terms u_{d2} , u_{d2} , and u_{d3} can be found separately. Considering u_{d1} , it is seen that the governing equation and boundary conditions are the same as for the wave problem of the time-invariant model in Part IV. The only difference is the presence of the factor $\sqrt{2/\pi}$ in the eddy viscosity distribution. Therefore, the governing equation can be nondimensionalized as in Part IV with

$$\delta = \frac{\kappa u_{*1}}{\omega} \tag{190}$$

in this case and solved to give five simultaneous equations similar to Equations 110 and 113 to 116. The only difference will be that a factor $\sqrt{2/\pi}$ appears in the denominator of the terms inside the square root sign of Equations 110, 113, and 114 and in the numerator of those terms in Equations 115 and 116.

288. Considering the solution for u_{d2} , it is seen that the same equations are obtained as for u_{d1} with the only difference being that the first equation will have a value of -1/12 on the right-hand side instead of -1. Since the right-hand side in the other four equations is zero, cf.

Equations 113 to 116, this value merely scales the five unknown coefficients in the solution. Therefore, u_{d2} can be written as

$$u_{d2} = \frac{u_{d1}}{12} \tag{191}$$

289. Finally, it is seen that the solution for the third harmonic term u_{d3} will yield five equations similar to those for u_{d1} with a factor 3 (3ω replaces ω) appearing in the numerator of all the terms inside the square root and a value 1/12 on the right-hand side of the first equation instead of -1.

290. Therefore, after solution of these two sets of simultaneous equations the solution can be written as

$$\tilde{u}_d = \mathrm{Re}\left\{u_{d1}e^{i\omega\tilde{t}} + \frac{u_{d1}}{12}e^{i(\omega\tilde{t}+2\phi_2)} + u_{d3}e^{i(3\omega\tilde{t}+2\phi_2)}\right\} \tag{192}$$

It should be noted that the first term in Equation 192 is of zeroth order in the small parameter assumed in the expansion of the boundary condition, Equation 186, while the other two terms are of first order.

291. The result obtained so far is in terms of the variable $\tilde{t}$; therefore, the solution must be completed by transforming Equation 192 into the real-time variable t using the relationship between the variables in Equation 182. To be consistent, this reverse transformation needs to be carried out to the same order in the small parameter of Equation 185 as was used in the expansion of the boundary condition to obtain Equation 186. This means that the term $\exp(i\omega\tilde{t})$ in Equation 192 must be expanded to first order while the other two exponentials need be expanded to leading order only. These expansions result in

$$e^{i\omega\tilde{t}} = e^{i\omega t} - \frac{1}{12}e^{-i(\omega t+2\phi_2)} + \frac{1}{12}e^{i(3\omega t+2\phi_2)} \tag{193}$$

$$e^{i(\omega\tilde{t}+2\phi_2)} = e^{i(\omega t+2\phi_2)} \tag{194}$$

$$e^{i(3\omega\tilde{t}+2\phi_2)} = e^{i(3\omega t+2\phi_2)} \tag{195}$$

292. Substituting Equations 193 to 195 into Equation 192 yields

$$u_d = \mathrm{Re}\left\{u_{d1}\left[e^{i\omega t} + \frac{i}{6}\sin(\omega t+2\phi_2)\right] + e^{i(3\omega t+2\phi_2)}\left[\frac{u_{d1}}{12} + u_{d3}\right]\right\} \tag{196}$$

293. The solution of the wave problem is closed, as in the case of the time-invariant model, by defining the bottom shear stress as in Equation 128. In this case, the definition is

$$\frac{\tau_b}{\rho} = \lim_{z=z_0}\left[(\bar{\nu}+\tilde{\nu}_e)\frac{\partial \tilde{u}_0}{\partial z}\right] \tag{197}$$

294. Since the deficit velocity in Equation 196 involves first and third harmonics, the shear stress in Equation 197 will also have first and third harmonics. By writing

$$\lim_{z=z_0}\left[\frac{\partial u_{d1}}{\partial z}\right] = \left|\frac{\partial u_{d1}}{\partial z}\right|_{z=z_0} e^{i\gamma} \tag{198}$$

$$\lim_{z=z_0}\left[\frac{\partial u_{d3}}{\partial z}\right] = \left|\frac{\partial u_{d3}}{\partial z}\right|_{z=z_0} e^{i\sigma} \tag{199}$$

it then follows from Equation 196 that

$$\begin{aligned}\frac{1}{u_b}\lim_{z=z_0}\left[\frac{\partial \tilde{u}_0}{\partial z}\right] &= \lim_{z=z_0}\left[\frac{\partial u_d}{\partial z}\right] \\ &= \left|\frac{\partial u_{d1}}{\partial z}\right|_{z=z_0}\left[\cos(\omega t+\gamma) - \frac{1}{12}(\cos(\omega t+2\phi_2-\gamma) - \cos(\omega t+2\phi_2+\gamma))\right. \\ &\quad \left. + \frac{1}{12}\cos(3\omega t+2\phi_2+\gamma)\right] + \left|\frac{\partial u_{d3}}{\partial z}\right|_{z=z_0}\cos(3\omega t+2\phi_2+\sigma)\end{aligned} \tag{200}$$

295. This expression can be substituted into Equation 197 along with the expression for the eddy viscosities from Equation 180 to obtain an expression for the bottom shear stress. Let the first and third harmonic shear stresses be denoted by τ_1 and τ_3, respectively. Then, after carrying out the substitution in Equation 197 and separating the first and third harmonics while retaining only those terms of the first order in the small parameter, the shear stresses are obtained as

$$\frac{1}{u_b}\frac{\tau_1}{\rho} = \sqrt{\frac{2}{\pi}}\kappa u_{*1}\left|\zeta\frac{\partial u_{d1}}{\partial\zeta}\right|_{z=z_0}$$
$$\left[\cos(\omega t+\gamma) + \frac{1}{12}(\cos(\omega t+2\phi_2+\gamma) + \cos(\omega t+2\phi_2-\gamma))\right] \tag{201}$$

296. Now τ_1 and u_{*1} are related by

$$\frac{\tau_1}{\rho} = u_{*1}^2\cos(\omega t+\phi_2) \tag{202}$$

297. By rearranging the term giving the time variation in Equation 201, it is seen that

$$\cos(\omega t+\gamma) + \frac{1}{12}[\cos(\omega t+2\phi_2+\gamma) + \cos(\omega t+2\phi_2-\gamma)]$$
$$= \cos(\omega t+\phi_2)\left[\cos(\gamma-\phi_2) + \frac{1}{6}\cos\gamma\cos\phi_2\right]$$
$$- \sin(\omega t+\phi_2)\left[\sin(\gamma-\phi_2) + \frac{1}{6}\sin\phi_2\cos\gamma\right] \tag{203}$$

298. From Equation 202, the time variation of τ_{w1} is given as proportional to $\cos(\omega t+\phi_2)$. Therefore, the second term in Equation 203 must vanish for all t . This leads to

$$\phi_2 = \tan^{-1}\left[\frac{6}{5}\tan\gamma\right] \tag{204}$$

and the closure equation, i.e., Equation 201, can be written as

$$\frac{u_{*1}}{u_b} = \sqrt{\frac{2}{\pi}}P\kappa\left|\zeta\frac{\partial u_{d1}}{\partial\zeta}\right|_{z=z_0} \tag{205}$$

with

$$P = \cos(\gamma-\phi_2) + \frac{1}{6}\cos\gamma\cos\phi_2 \tag{206}$$

299. Equation 205 is an implicit equation for u_{*1} and can be solved by iteration. For small μ it is seen that this equation differs from the closure equation of the time-invariant model only in the presence of a factor $\sqrt{2/\pi}P$ in Equation 205. From Equations 204 and 205, it is found

that $P = 1.12$ for $\gamma = 30^\circ$ which is a typical value in practice. This results in the extra factor in the closure equation having a value of 0.89.

300. As a result of this similarity in the closure equations, it can be expected that the wave solution from the time-varying model will be close to that of the time-invariant model. This can be seen in Figure 24, which compares the wave friction factor for a pure wave motion obtained from the two models. It is apparent that the friction factors differ by only about 9 percent.

301. It should be noted that the wave friction factor for the time-varying model plotted in Figure 24 is defined using the magnitude of the first harmonic of the bottom shear stress, i.e., by

$$\tau_1 = \frac{1}{2}\rho f_w u_b^2 \tag{207}$$

and not by the maximum bottom shear stress. In the time-invariant model, the assumption of a constant eddy viscosity resulted in the bed shear stress containing only a first harmonic component, which meant that the maximum bed shear stress was equal to the magnitude of that component.

302. Furthermore, since the near-bottom eddy viscosity is scaled by u_{*1}, the only effect of a current (i.e., $\mu \neq 0$) on the wave problem will be to impose a linear variation of the eddy viscosity above the level $\zeta = \sqrt{\frac{2}{\pi}} a_1/\mu$ instead of the constant value used in the pure wave problem (i.e., when $\mu = 0$). The wave friction factor in the presence of currents, f_{wc}, is plotted against A_b/k_n in Figure 25 for several values of μ. It is seen that f_{wc} is only very weakly dependent on μ. However, the symbol f_{wc} will still be used to denote the presence of a current.

303. Similarly, after substitution into Equation 197 the third harmonic shear stress can be written as

$$\frac{1}{u_b}\frac{\tau_3}{\rho} = \sqrt{\frac{2}{\pi}}\kappa u_{*1}\left[\left|\zeta\frac{\partial u_{d1}}{\partial\zeta}\right|_{z=z_0}\frac{1}{4}\cos(3\omega t+2\phi_2+\gamma) + \left|\zeta\frac{\partial u_{d3}}{\partial\zeta}\right|_{z=z_0}\cos(3\omega t+2\phi_2+\sigma)\right] \tag{208}$$

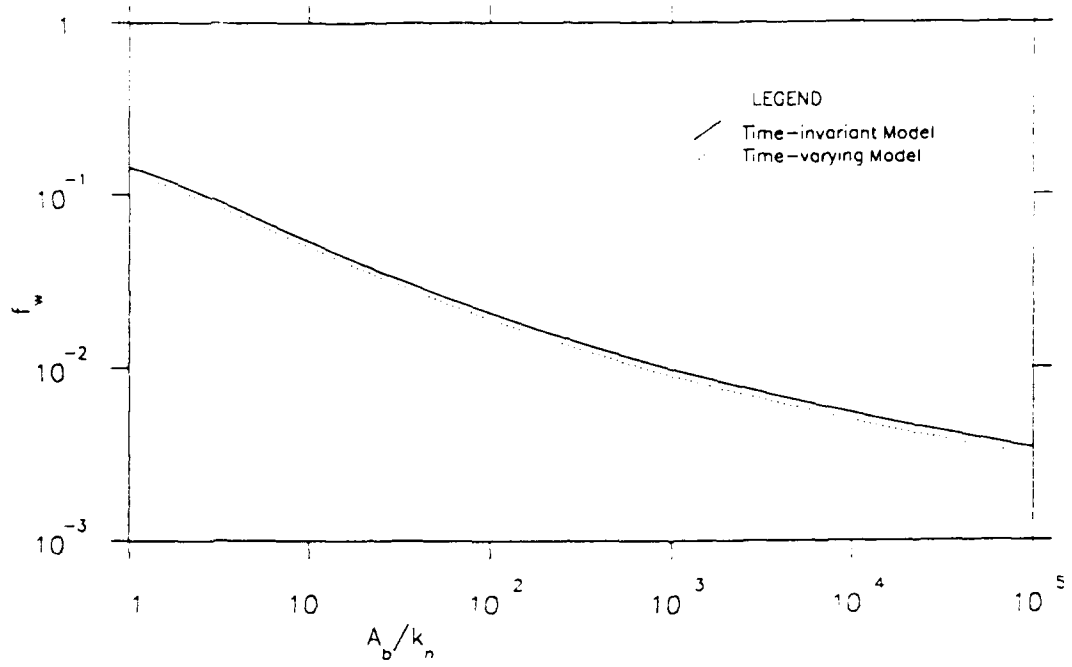

a. Wave friction factor diagram

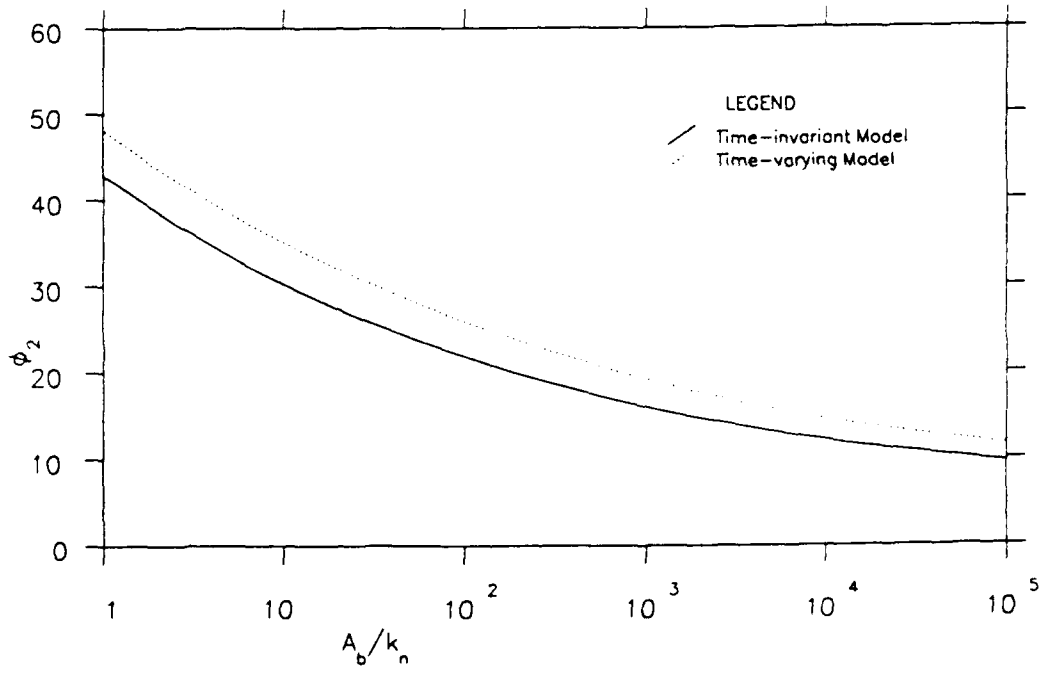

b. Phase lead of the bottom shear stress

Figure 24. Comparison of the wave friction factor and phase lead of the bottom shear stress obtained from the time-invariant and time-varying models

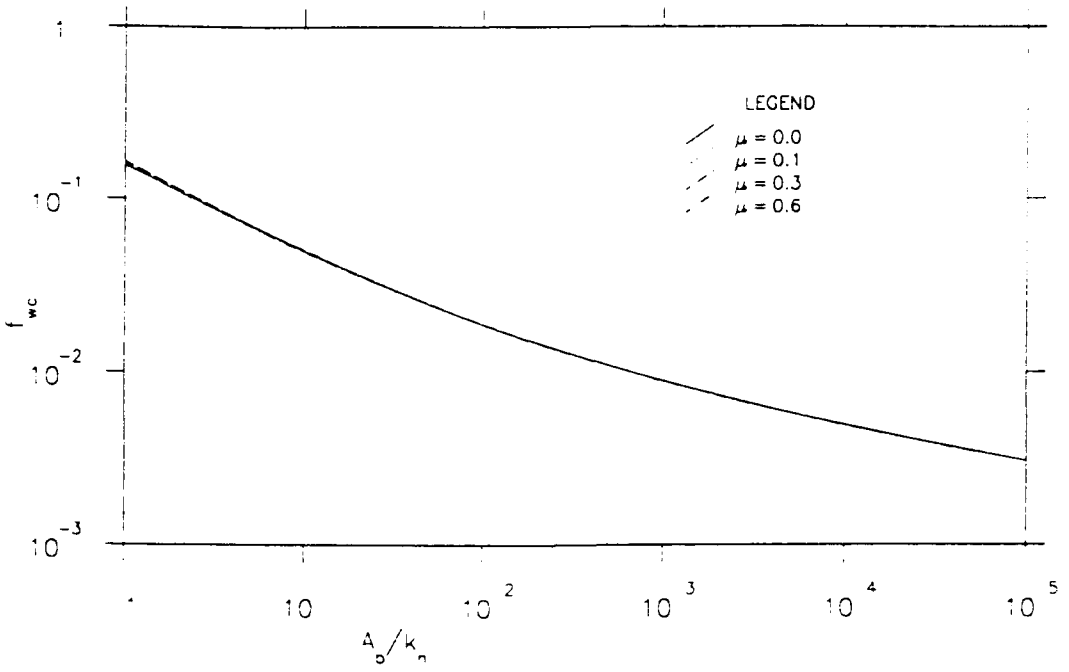

a. Wave friction factor diagram

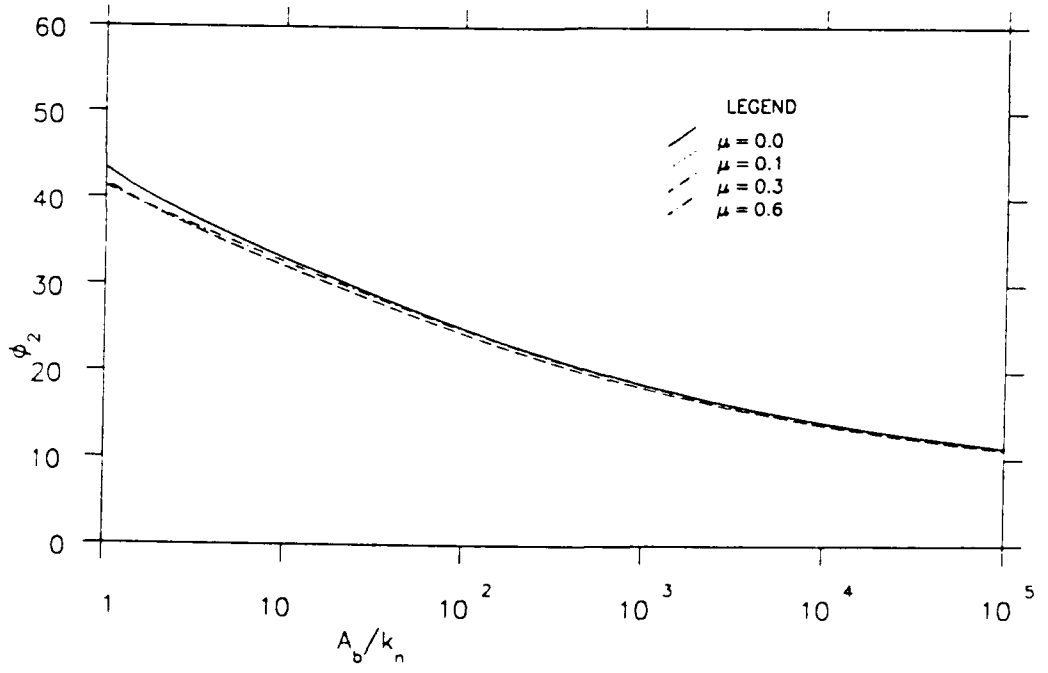

b. Phase lead of the bottom shear stress

Figure 25. Wave friction factor in the presence of a current, f_{wc}, and the phase lead of the bottom shear stress, ϕ_2, against A_b/k_n for several values of μ from the time-varying model

304. After manipulating this expression as done for Equation 201, the third harmonic shear stress can be written as

$$\frac{\tau_3}{\rho} = \sqrt{\frac{2}{\pi}}\kappa u_b u_{*1} Q \cos(3\omega t + \phi_3) \tag{209}$$

where

$$\phi_3 = \tan^{-1}\left[\frac{\frac{1}{4}\left|\zeta\frac{\partial u_{d1}}{\partial\zeta}\right|_{z=z_0}\sin(2\phi_2+\gamma) + \left|\zeta\frac{\partial u_{d3}}{\partial\zeta}\right|_{z=z_0}\sin(2\phi_2+\sigma)}{\frac{1}{4}\left|\zeta\frac{\partial u_{d1}}{\partial\zeta}\right|_{z=z_0}\cos(2\phi_2+\gamma) + \left|\zeta\frac{\partial u_{d3}}{\partial\zeta}\right|_{z=z_0}\cos(2\phi_2+\sigma)}\right] \tag{210}$$

and

$$Q = \frac{1}{4}\left|\zeta\frac{\partial u_{d1}}{\partial\zeta}\right|_{z=z_0}\cos(2\phi_2+\gamma-\phi_3) + \left|\zeta\frac{\partial u_{d3}}{\partial\zeta}\right|_{z=z_0}\cos(2\phi_2+\sigma-\phi_3) \tag{211}$$

305. Therefore the magnitude of the third harmonic shear stress can be found using Equations 209-211. It is found that the ratio τ_1/τ_3 is 0.115 for $A_b/k_n = 4$ and 0.136 for $A_b/k_n = 10^6$. Furthermore, ϕ_3 was found to have almost three times the value of ϕ_2. This means that the peak shear stress will be very close to the sum of τ_1 and τ_3. In other words, the peak shear stress is about 12 percent greater that τ_1. Recalling that the value of τ_1 from the time-varying model was about 9 percent less than the maximum shear stress given by the time-invariant model, it is seen that the maximum bed shear stresses predicted by both models will be nearly identical.

306. The first and third harmonic velocities, denoted by u_{w1} and u_{w3}, can be obtained from Equation 196 as

$$u_{w1} = u_b\left\{\cos\omega t + \mathrm{Re}\left[u_{d1}\left[e^{i\omega t} + \frac{i}{6}\sin(\omega t+2\phi_2)\right]\right]\right\} \tag{212}$$

and

$$u_{w3} = u_b \mathrm{Re}\left[e^{i(3\omega t+2\phi_2)}\left[\frac{u_{d1}}{12} + u_{d3}\right]\right] \tag{213}$$

Current Problem

307. The governing equations are Equations 163 and 164. The second term in Equation 163 appears as a result of the eddy viscosity being allowed to be time-varying. From Equations 172 and 174, it is seen that

$$\tilde{\nu}_0 = \bar{\nu}\mu^2\cos\phi_{cw}\cos(\omega t+\phi_2) \tag{214}$$

and from Equation 212, it is found that

$$\frac{\partial\tilde{u}_0}{\partial z} = u_b \mathrm{Re}\left\{\frac{\partial u_{d1}}{\partial z}\left[e^{i\omega t} + \frac{i}{6}\sin(\omega t+2\phi_2)\right]\right\} \tag{215}$$

308. Let

$$\frac{\partial u_{d1}}{\partial z} = \frac{u_b}{\delta}U'(z)e^{i\phi_1(z)} \tag{216}$$

where δ is defined in Equation 190 and

$$U'(z) = \left|\frac{\partial u_{d1}}{\partial\zeta}\right| \tag{217}$$

Then

$$\frac{\partial\tilde{u}_0}{\partial z} = \frac{u_b}{\delta}U'(z)\left\{\cos[\omega t+\phi_1(z)] - \frac{1}{6}\sin\phi_1(z)\sin(\omega t+2\phi_2)\right\} \tag{218}$$

and the second term on the right-hand side of Equation 163 can be evaluated as

$$\overline{\tilde{\nu}_0\frac{\partial\tilde{u}_0}{\partial z}} = \bar{\nu}\mu^2\cos\phi_{cw}\frac{U_b}{\delta}U'(z)\frac{1}{2}\left\{\cos[\phi_1(z)-\phi_2] - \frac{1}{6}\sin\phi_1(z)\sin\phi_2\right\} \tag{219}$$

309. Substituting Equation 219 into Equation 163, dividing by $\bar{\nu}$, and integrating from z_0 to a level z gives

$$\bar{u} = \cos\phi_{cw}\left[\int_{z_0}^{z}\frac{u_{*c}^2}{\bar{\nu}}dz - \frac{\mu^2 u_b}{\delta}\int_{z_0}^{z}\frac{U'(z)}{2}\left\{\cos[\phi_1(z)-\phi_2] - \frac{1}{6}\sin\phi_1(z)\sin\phi_2\right\}dz\right] \tag{220}$$

310. Introducing the nondimensional vertical coordinate ζ, defined in Equation 61, gives

$$\bar{u} = \cos\phi_{cw}\left[\int_{\zeta_0}^{\zeta} \frac{\delta u_{*c}^2}{\bar{\nu}} d\zeta - \mu^2 u_b \int_{\zeta_0}^{\zeta} \frac{U'(\zeta)}{2}\left\{\cos[\phi_1(\zeta)-\phi_2] - \frac{1}{6}\sin[\phi_1(\zeta)]\sin\phi_2\right\} d\zeta\right] \quad (221)$$

311. This can be written as

$$\bar{u} = \cos\phi_{cw}[I_1(\zeta) - I_2(\zeta)] \quad (222)$$

with

$$I_1(\zeta) = \int_{\zeta_0}^{\zeta} \frac{u_{*c}^2 \delta}{\bar{\nu}} d\zeta \quad (223)$$

and

$$I_2(\zeta) = \int_{\zeta_0}^{\zeta} \frac{\mu^2 u_b U'(\zeta)}{2}\left\{\cos[\phi_1(\zeta)-\phi_2] - \frac{1}{6}\sin\phi_1(\zeta)\sin\phi_2\right\} d\zeta \quad (224)$$

312. Integration of Equation 164 results in

$$\bar{v} = I_1(\zeta)\sin\phi_{cw} \quad (225)$$

313. Equation 222 indicates that the equation for the component of the current velocity in the wave direction has two terms—the first due to the mean shear stress and the second due to the time-varying eddy viscosity, i.e., due to the wave motion. Equation 225, which is for the component in the direction normal to the wave motion, has only the contribution from the mean shear stress.

314. Equation 222 can be written as

$$\bar{u} = \int_{z_0}^{z} \frac{u_{*c}^2 \cos\phi_{cw}}{\bar{\nu}}[1-R(z)]dz \quad (226)$$

where

$$R(z) = \frac{\overline{\tilde{\nu}_0 \frac{\partial \tilde{u}_0}{\partial z}}}{u_{*c}^2 \cos\phi_{cw}} \tag{227}$$

315. Using Equation 214 for the relation between $\tilde{\nu}_0$ and $\bar{\nu}$ and Equation 199 for the definition of μ, Equation 227 can be written as

$$R(z) = \frac{\bar{\nu}}{u_{*1}^2} \overline{\frac{\partial \tilde{u}_0}{\partial z} \cos(\omega t + \phi_2)} \tag{228}$$

316. The function $R(z)$ gives the importance of the second term, which is related to the wave motion, to the first, which is related to the mean shear stress. In the limit as z approaches z_0 it is seen that

$$\lim_{z \to z_0} [R(z)] = \frac{1}{u_{*1}^2} \kappa \sqrt{\frac{2}{\pi}} u_{*1} \lim_{z \to z_0} \left[z \overline{\frac{\partial \tilde{u}_0}{\partial z} \cos(\omega t + \phi_2)} \right] \tag{229}$$

where the expansion for $\bar{\nu}$ from Equation 174 has been used. From the closure of the wave problem in the time-varying model in Equation 205, this can be written as

$$\lim_{z \to z_0} [R(z)] = \frac{\left[\cos(\phi_2 - \gamma) - \frac{1}{6} \sin\phi_2 \sin\gamma \right]}{2P} \tag{230}$$

where γ is defined in Equation 198 and P in Equation 206.

317. Equation 230 has been evaluated for range of values of μ and A_b/k_b. It is found that the value of $R(z)$ at the bottom lies between 0.423 and 0.428 for $1 < A_b/k_b < 10^6$ and for any value of μ.

318. The above result shows that near the bottom the mean velocity component in the wave direction, $\bar{u}$, increases less rapidly than that in the direction normal to the waves, $\bar{v}$. This means that the value of the mean velocity will be sensitive to ϕ_{cw} because the partitioning of the velocity into the two components depends on ϕ_{cw}. It is hoped that this new mechanism by which the current velocity is linked to ϕ_{cw} will lead to

results that are in better agreement with the data than the results of the time-invariant model, where this mechanism was not present.

319. The integral $I_1(\zeta)$ can be evaluated analytically using the eddy viscosity distribution given in Equation 174 to yield

$$I_1(\zeta) = \begin{cases} \frac{u_{*c}}{\kappa}\mu\sqrt{\frac{\pi}{2}}\ln\left[\frac{\zeta}{\zeta_0}\right] & \zeta_0 < \zeta < a_1 \\ \frac{u_{*c}}{\kappa}\mu\sqrt{\frac{\pi}{2}}\left[\frac{\zeta}{a_1} - 1 + \ln\left[\frac{a_1}{\zeta_0}\right]\right] & a_1 < \zeta < \frac{a_1\sqrt{\frac{2}{\pi}}}{\mu} \\ \frac{u_{*c}}{\kappa}\left[\ln\left[\frac{\zeta\mu}{a_1\sqrt{\frac{2}{\pi}}}\right] + 1 + \mu\sqrt{\frac{\pi}{2}}\left[\ln\left[\frac{a_1}{\zeta_0}\right] - 1\right]\right] & \zeta > \frac{\sqrt{\frac{2}{\pi}}a_1}{\mu} \end{cases} \quad (231)$$

where the constants of integration have been determined by requiring continuity of the velocity at the various matching levels.

320. Once the wave problem is solved, the values of $U'(\zeta)$ and $\phi_1(\zeta)$ can be found at any level, thus allowing the numerical integration of I_2. Finally, the angle between the current velocity vector and the direction of waves, ϕ_c, is given by

$$\phi_c = \tan^{-1}\left[\frac{\tan(\phi_{cw})I_1(\zeta)}{I_1(\zeta) - I_2(\zeta)}\right] \quad (232)$$

321. Equation 230 shows that near the bottom $I_2(\zeta)$ is positive and less than $I_1(\zeta)$. Therefore $I_1(\zeta)$ is greater than $I_1(\zeta) - I_2(\zeta)$, which results in $\phi_c > \phi_{cw}$ from Equation 232. In other words, the effect of the waves is to deflect the current velocity further from the wave direction than the mean shear stress. Since the second term in Equation 163 is related to the waves, it can be expected to die out near the top of the wave boundary layer. Then $I_2(\zeta)$ will reach a constant value at that level while $I_1(\zeta)$ keeps on increasing. This will result in the difference between ϕ_c and ϕ_{cw} decreasing; therefore, at large heights above the bottom, the direction of the current will approach that of the mean shear stress. This feature was not present in the time-invariant model, and its presence here is an indication that the time variation of the eddy viscosity provides a more complete representation of the problem.

322. It should be noted that when $\tilde{\nu}_0$ is defined by Equation 214, it is implied that the eddy viscosity varies with time for all values of z, whereas in Equation 174 the time variation is specified only below the level $z = \sqrt{2/\pi}(a_1/\mu)$. As discussed, the wave effects die out around the level $z = \delta$, and integral I_2 will reach a constant value. Therefore use of Equation 214 will not lead to significant error so long as the inequality in Equation 176 holds.

323. Another point to be kept in mind is that a_1 the model parameter has not been specified as yet. As in the time-invariant model, this is done by comparing the model results to the experimental data and selecting a value that gives the best agreement.

Comparison with Experimental Data

324. The results of the time-varying eddy viscosity model are compared with the experimental data used in the preceding chapter.

Waves alone

325. The first harmonic wave velocity and phase from Test 1 of Jonsson and Carlsen (1976) are compared in Figure 26 to the predictions from the time-varying model using three different values of the parameter a_1. It is seen that the predicted profiles are very similar to those from the time-invariant model, using the corresponding value of a, that are shown in Figure 15. The results for the other data sets are also very close to those from the time-invariant model and will therefore not be presented here. As shown in Figure 26 the three values of a_1 give identical results near the bottom, which are in good agreement with the data while diverging at the top of the boundary layer where the agreement with the data is not that good.

326. The third harmonic wave velocity and phase for the same experiment are compared with the predictions from the model, using the same values of a_1, in Figure 27. It is seen that the predicted maximum magnitude of the results is less than the experimental value by 60 percent or more while the shape of the velocity profile is obtained reasonably well. The theoretical phase profile of the third harmonic is similar to the experimental values but with a shift in the vertical axis. The comparison between theory and experiment for the third harmonic of Test 2 of Jonsson and Carlsen is

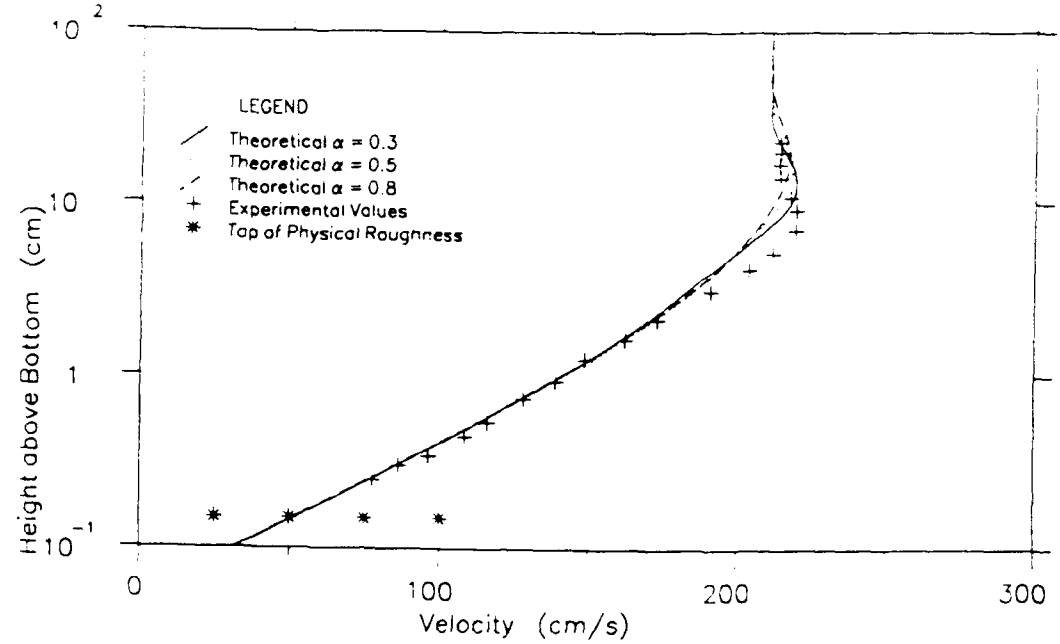

a. Wave velocity

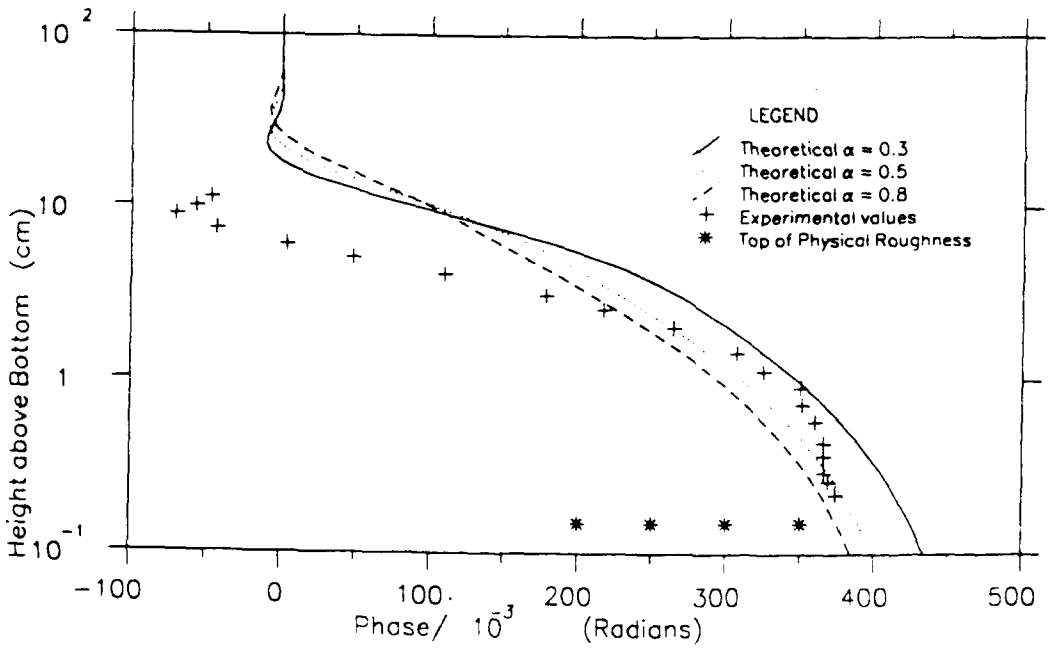

b. Phase

Figure 26. Comparison of the first wave velocity and phase profiles of Jonsson and Carlsen (1976) Test 1 with the results of the time-varying model using three different values of α_1

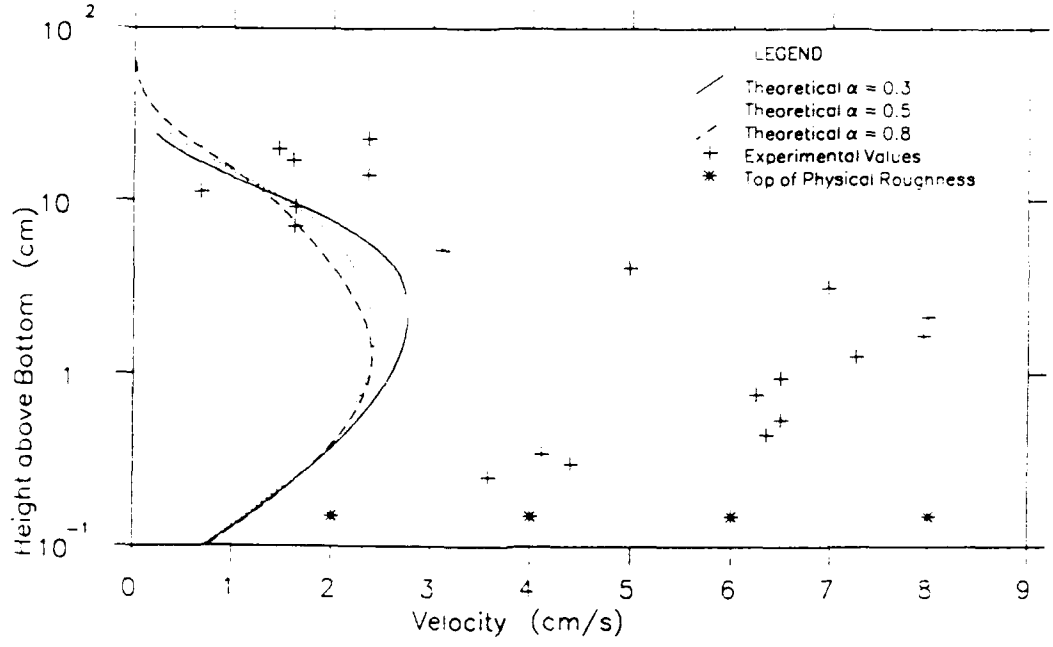

a. Wave velocity

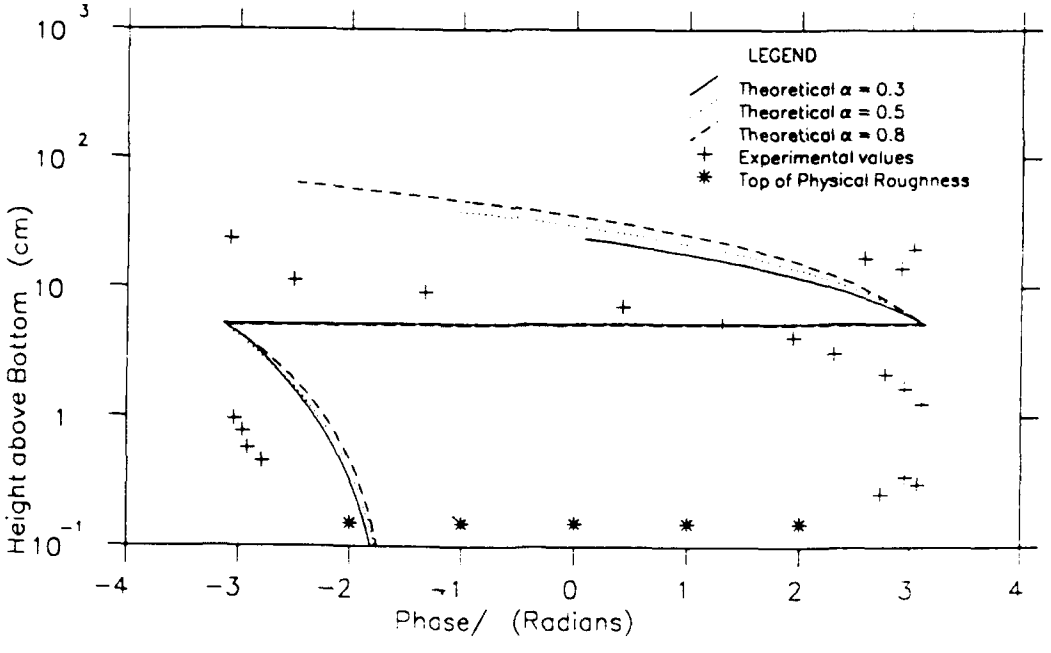

b. Phase

Figure 27. Comparison of the third harmonic wave velocity and phase profiles of Jonsson and Carlsen (1976) Test 1 with the result of the time-varying model using three different values of α_1

similar to Figure 27 and is therefore not shown. The agreement with the data shown in Figure 27 is similar to that obtained by Trowbridge and Madsen (1984a and b). The data clearly show the existence of a third harmonic component, thus justifying the inclusion of a time-varying eddy viscosity.

327. The predicted first harmonic, third harmonic, and peak shear stresses and the phase of the peak shear stress from the time-varying model are presented in Table 9 along with the peak shear stress and phase from Davies, Soulsby, and King (1988). The magnitude of the third harmonic shear stress is about 11 percent of that of the first harmonic shear stress. These two shear stresses have nearly the same phase, resulting in the peak shear stress being the sum of the two components.

328. Figure 24 indicates that the friction factor for the time-varying model was about 9 percent less than that for the time-invariant model. This friction factor was defined using the first harmonic shear stress only. However, when the sum of the two harmonics is considered, it is seen that the peak shear stress in the time-varying model is very close to the peak shear stress of the time-invariant model, which only allowed a first

Table 9

Calculated First Harmonic, Third Harmonic, and Peak Shear Stresses and the Phase of the Peak Shear Stress for the Conditions of Davies, Soulsby, and King (1988) from the Time-varying Model Compared to the Results of Davies, Soulsby, and King (1988)

	Time Varying Model Results								Davies et al.	
	Shear Stresses (Pa)						Phase of Peak Shear Stress deg		Peak Shear Stress Pa	Phase of Peak Shear Stress deg
	First Harmonic		Third Harmonic		Peak Shear Stress					
Data Set	α_1=0.5	α_1=0.8	α_1=0.5	α_1=0.8	α_1=0	α_1=0	α_1=0.5	α_1=0.8		
DVW05	9.3	9.4	1.1	1.1	10.3	10.5	39.4	35.1	8.1	28.2
DVW10	26.9	26.9	3.2	3.2	30.0	30.0	34.8	32.3	23.5	26.4
DVW10	50.3	50.1	6.0	5.9	56.3	56.0	32.9	30.8	44.3	25.2

harmonic, shown in Table 6. This agrees with the results of Trowbridge and Madsen (1984a and b).

329. As in the case of the time-invariant model, the comparison shown in Figures 26 and 27 indicates that a value of α_1 equal to 0.3 or slightly less will result in the best agreement with the data. However, the higher values of α_1 agree with the data near the bottom. Therefore, as in the time-invariant model, determination of a value for α_1 is deferred until the comparison with the experimental current velocity profile is made.

Waves and currents

330. The current velocity profiles obtained from the time-varying model using three different values of α_1 are compared with the Bakker and van Doorn (1978) data in Figure 28. The profiles obtained using $\alpha_1 = 0.8$ and $\alpha_1 = 1.0$ for the data set BVD10 are in better agreement with the data than the profile obtained with $\alpha_1 = 0.5$. Considering the set BVD20, all three values of α_1 give good results with the two higher values doing slightly better.

331. However, in these two sets, the current is specified by the velocity at a point in the upper logarithmic region; i.e., the calculated profile is required to pass through a selected data point. Since the model also uses a logarithmic profile in the outer region, this means that the calculated profile will not be very sensitive to the value of α_1 .

332. A better test for the appropriate value of α_1 is with data sets where the current is specified by the mean shear stress as in the conditions of Davies, Soulsby, and King (1988). The results for waves and currents in the same direction using $\alpha_1 = 0.5$ and $\alpha_1 = 0.8$ are compared with their results in Figure 29. It is seen that $\alpha_1 = 0.8$ gives a good fit to the data. This value of α_1 is greater than the value $\alpha = 0.5$ that was proposed for the time-invariant model.

333. There are two reasons for the different values of the model parameter obtained from the two models. First, the eddy viscosity used in the time-varying model is based on the mean shear velocity instead of the maximum shear velocity used in the time-invariant model. These two shear velocities differ by a factor of $\sqrt{2/\pi}$ as shown in Equation 172. Therefore, if it is required to have the same value of eddy viscosity in the intermediate region $\alpha_1\delta < z < \sqrt{2/\pi}\alpha_1\delta/\mu$, it seems that a value of α_1 around 0.625 should be used.

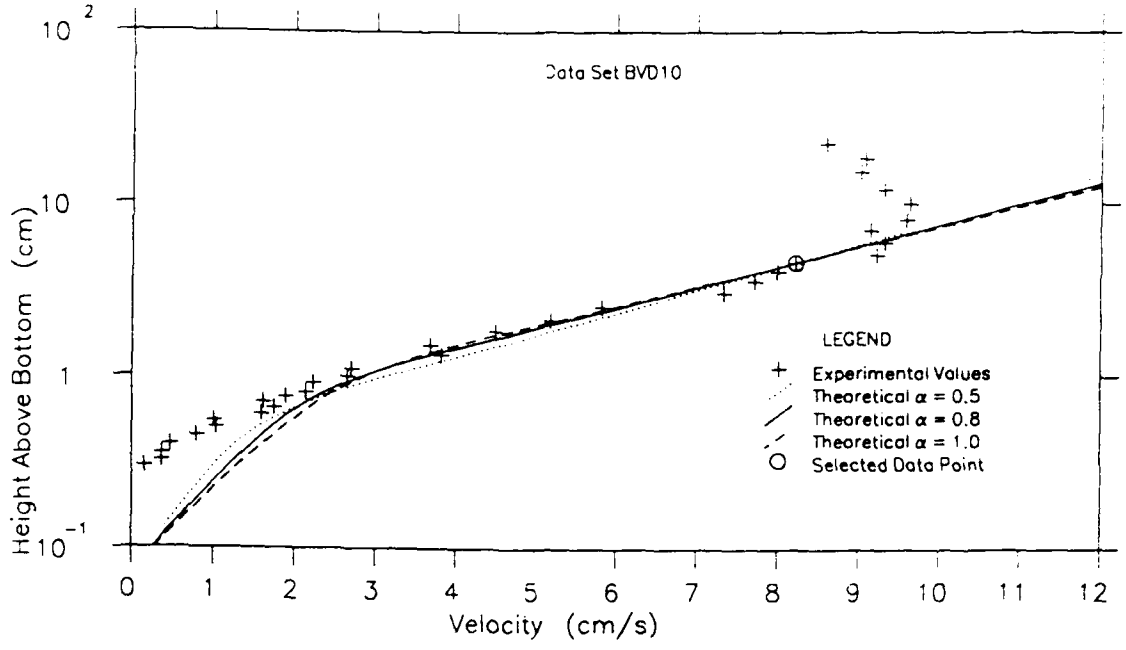

a. Data set BVD10

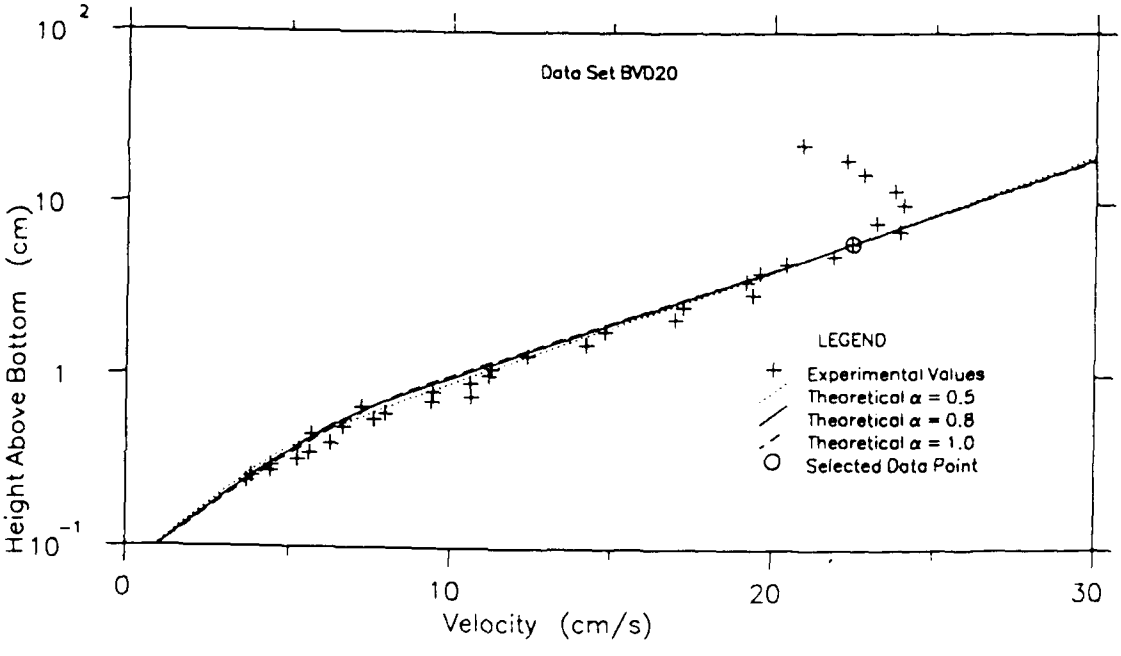

b. Data set BVD20

Figure 28. Comparison of the current velocity profiles from Bakker and Van Doorn (1978) with the results of the time-varying model $\alpha_1 = 0.5$, $\alpha_1 = 0.8$, and $\alpha_1 = 1.0$

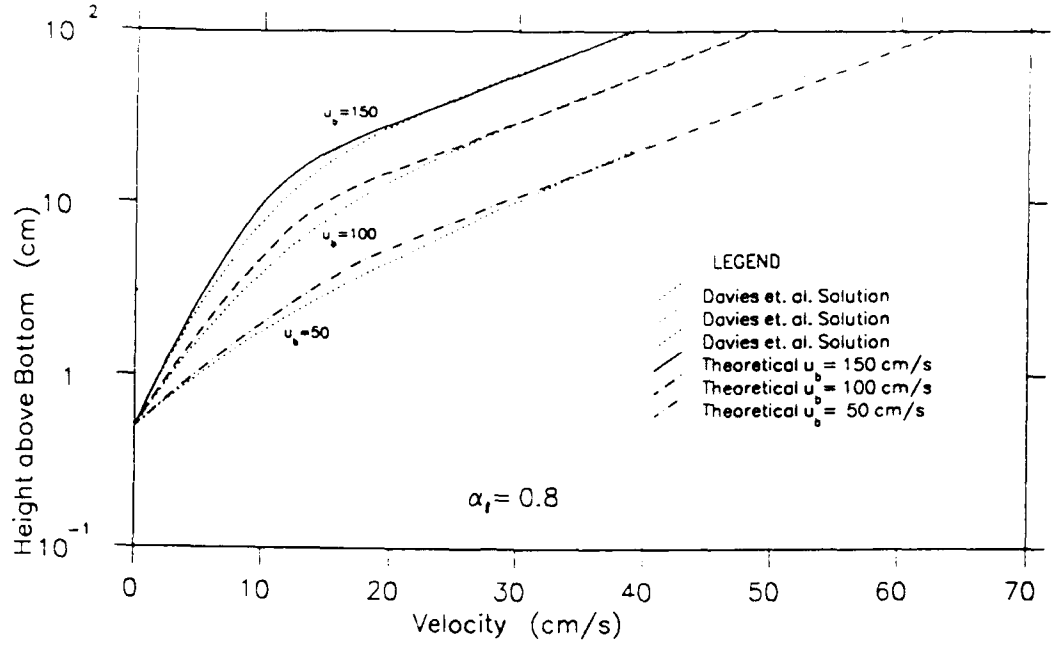

a. Comparison with $\alpha_1 = 0.8$

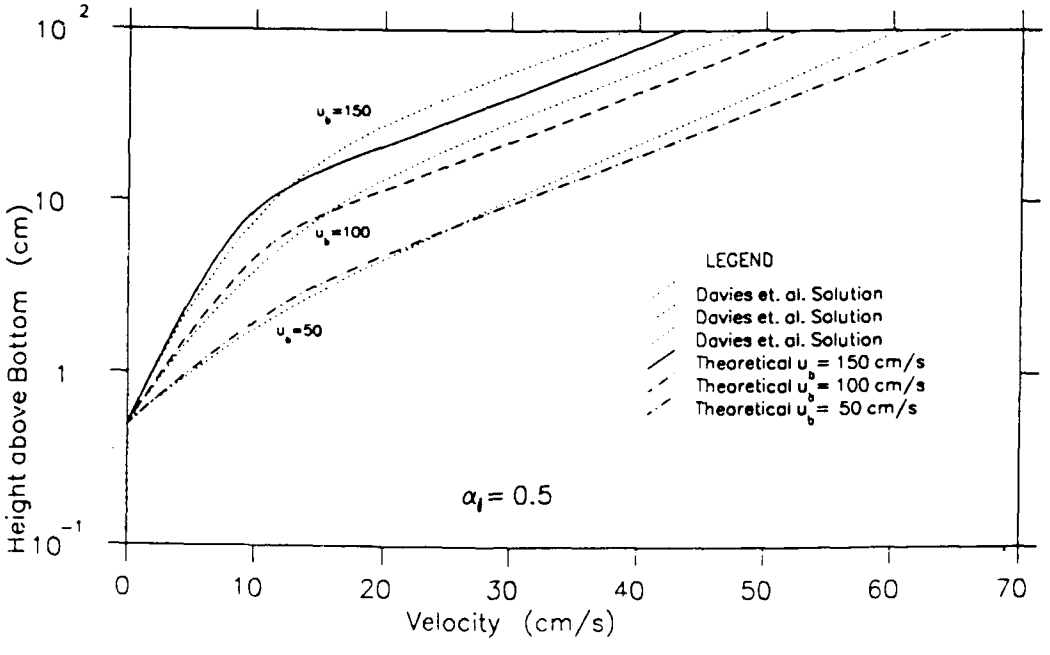

b. Comparison with $\alpha_1 = 0.5$

Figure 29. Comparison of the current velocity profiles from Davies, Soulsby, and King (1988) for waves and the current in the same direction with the results of the time-varying model with $\alpha_1 = 0.8$ and $\alpha_1 = 0.5$

334. Second, in the time-varying model, the shear velocity is based on the maximum wave shear stress rather than the maximum combined shear stress because the model is derived assuming a weak current relative to the waves ($\mu \ll 1$); therefore, the two shear stresses are assumed the same. However, the value of μ for the conditions simulated by Davies, Soulsby, and King (1988) is in the range 0.26 to 0.61 and is therefore not small. This means that the value of α_1 must increase further if the eddy viscosity profile used and therefore the current velocity profiles obtained are to be similar.

335. When conditions where μ is in fact small are considered, a value of α_1 about 0.65 gives a current profile that matches the profile from the time-invariant model using $\alpha = 0.5$. This change in α_1 can also be seen in the values of Table 10, which gives the current shear stresses obtained for the conditions of Bakker and van Doorn (1978) for the three values of α_1 along with the results of the time-invariant model with $\alpha = 0.5$. The data set BVD10 has a value of $\mu = 0.28$ while the set BVD20 has $\mu = 0.56$. It is seen that for the set BVD10, a value of α_1 between 0.5 and 0.8 gives the same result as the time-invariant model while $\alpha_1 = 1.0$ is required to obtain the same result for the set BVD20.

Table 10

Calculated Maximum and Current Shear Stresses for the Conditions of Bakker and Van Doorn from the Time-varying Model for Three Values of α_1 and the Time-Invariant Model with $\alpha = 0.5$

	Current Shear Stress (Pa)				Maximum Shear Stress (Pa)			
	Time-Varying model			Time-Invariant Model	Time-Varying Model			Time-Invariant Model
Data Set	α_1=0.5	α_1=0.8	α_1=1.0	α=0.5	α_1=0.5	α_1=0.8	α_1=1.0	α=0.5
BVD10	0.17	0.21	0.23	0.19	3.0	3.1	3.1	3.0
BVD20	0.67	0.72	0.74	0.74	3.3	3.4	3.4	3.5

336. The results for waves and the current at an angle are compared with the results of Davies, Soulsby, and King in Figure 30 for $\alpha_1 = 0.5$ and $\alpha_1 = 0.8$. The figure shows that the time-varying model shows much greater sensitivity to the angle between the waves and the current than the time-invariant model shown in Figure 21. The velocity difference between $\phi_{cw} = 0$ and $\phi_{cw} = 90$ in the upper region is found to be 5.2 cm/sec as compared with 2.5 cm/sec from the time-invariant model.

337. This improvement is a result of the additional term in the equation for the current velocity in the wave direction, i.e., in Equation 163. It shows that there is more resistance to the mean flow in the wave direction than in the direction normal to the wave motion. In the time-invariant model the angle between the waves and the current, ϕ_{cw} , only comes in in Equation 119, which relates the combined shear stress to the wave and current shear stresses. The only effect ϕ_{cw} has on the velocity profile is to make u_{*cw} take on different values which results in only a small change in the profiles unless μ is very large.

338. Another result of the time-varying model using two equations from the two components of the mean velocity is that when $0 < \phi_{cw} < 90^\circ$, the direction of the mean velocity vector changes with height above the bottom as given in Equation 232. The results for the case $\phi_{cw} = 45^\circ$ are compared with those of Davies, Soulsby, and King in Figure 31. As expected from the form of Equation 92, the model predicts that the current velocity is at a greater angle to the wave direction than the mean shear stress. However, the predicted value of this increase is less than the data by about 4°, while the shape of the curve agrees with the data.

339. The comparisons of the current profiles with the experimental data strongly suggest that $\alpha_1 = 0.8$ be selected as the value of the model parameter. The comparison with the pure wave data suggests a value of $\alpha_1 = 0.3$ be used. As in the time-invariant model, the model parameter will be selected so as to give the best agreement with the current profile because the resulting relatively poor agreement with the pure wave data is only at the top of the wave boundary layer, a region that is not of great importance in likely applications of the theory.

340. Therefore $\alpha_1 = 0.8$ is taken as the model parameter. There is, however, an indication that a smaller value of α_1 (around 0.65) will be more suitable in cases where μ is small. Nevertheless, Figures 28, 29,

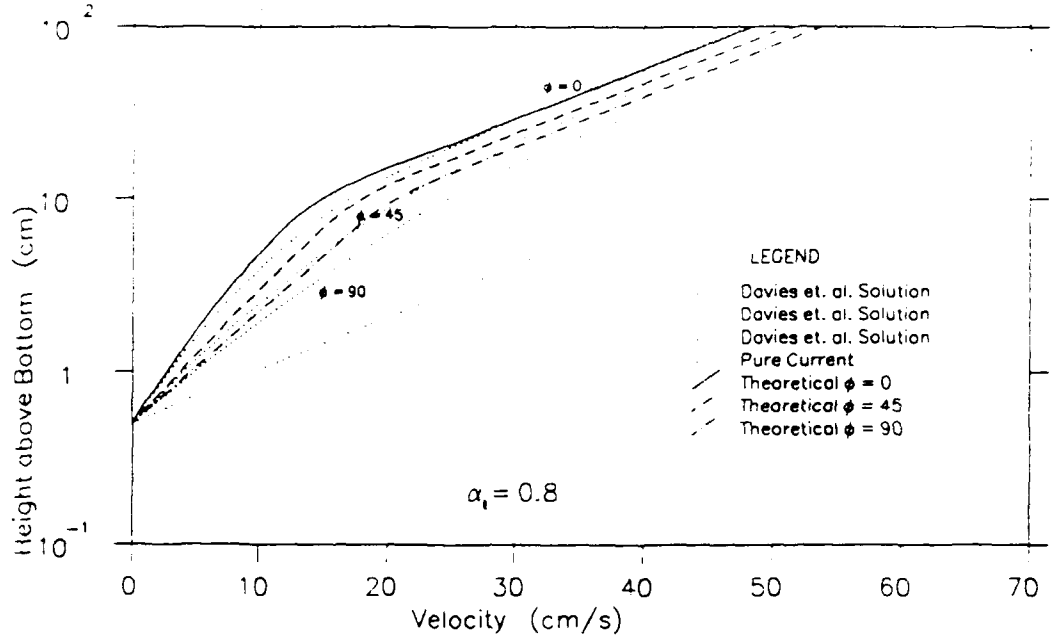

a. Comparison with $\alpha_1 = 0.8$

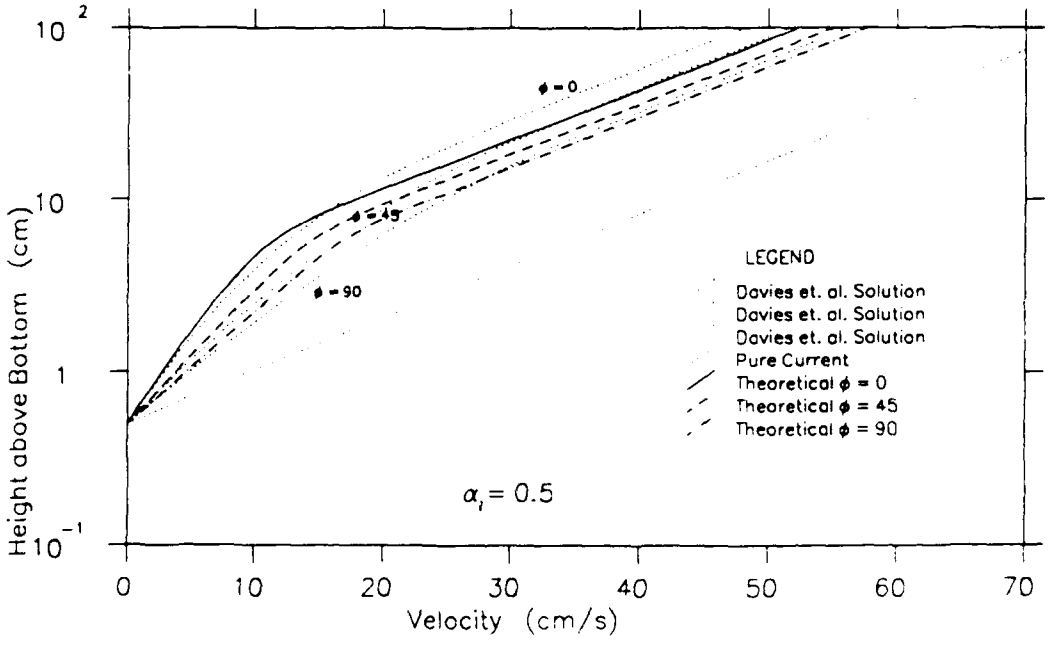

b. Comparison with $\alpha_1 = 0.5$

Figure 30. Comparison of the current velocity profiles from Davies, Soulsby, and King (1988) for waves and the current at an angle with the results of the time-varying model with $\alpha_1 = 0.8$ and $\alpha_1 = 0.5$

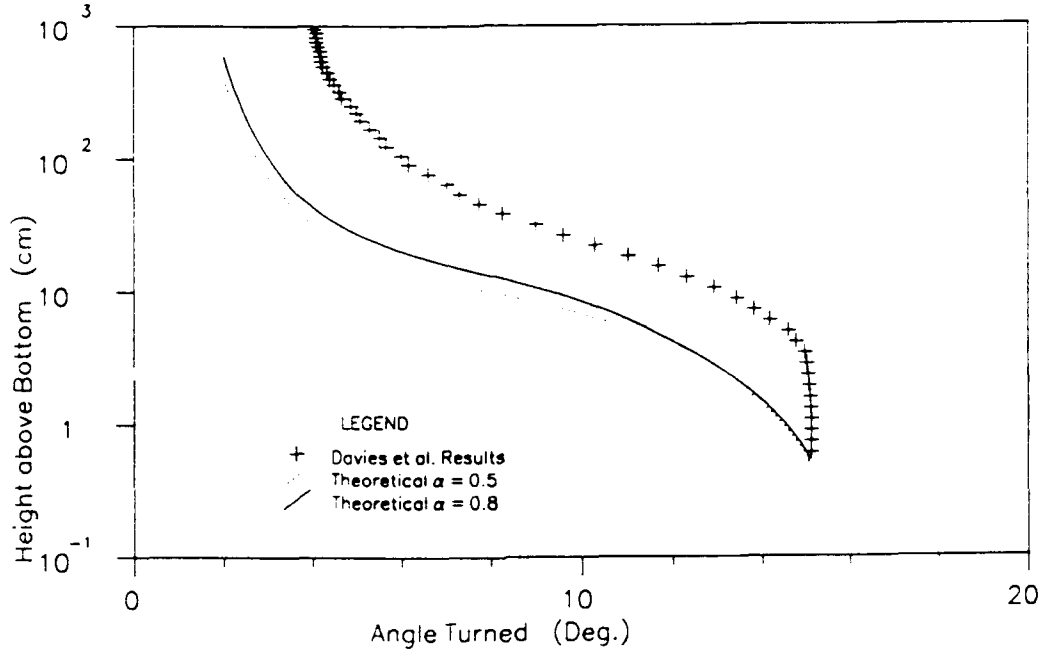

Figure 31. Comparison of the angle that the current velocity vector is deflected from the direction of the mean shear stress for the case ϕ_{cw} = 45° of Davies, Soulsby, and King (1988) with the results of the time-varying model with a_1 = 0.5 and a_1 = 0.8

and 30 show that a_1 = 0.8 give good agreement for conditions with μ ranging from 0.25 to 0.6. This is seen as sufficient evidence to adopt that value for the model.

Simplification of Current Problem

341. The time-varying model presented in this chapter is able to represent the wave-current interaction better than the time-invariant model. This improvement was gained at the cost of requiring a numerical integration to obtain the current velocity profile. If a simple analytic form of this integral can be obtained, the solution of the current problem

of this model will be no more complicated than that of the time-invariant model.

342. As given in Equation 226, the current velocity in the wave direction can be written as

$$\bar{u} = \int_{\zeta_0}^{\zeta} \frac{u_{*c}^2 \cos\phi_{cw}}{\bar{\nu}} [1 - R(\zeta)] d\zeta \tag{233}$$

with $\bar{\nu}$ defined by Equation 174 and δ by Equation 190. Equation 229 indicates that the value of $R(\zeta)$ is between 0.423 and 0.428 at $z = z_0$. $R(\zeta)$ represents the effect of the wave motion on the current profile and can be expected to die out at a height above the bottom that is scaled by the wave boundary layer thickness.

343. Therefore, the simplest approximation for $R(\zeta)$ will be a linear variation from a value of 0.425 at $z = z_0$ to zero at $z = \delta$ with the value being zero for $z > \delta$. In terms of the nondimensional vertical coordinate ζ, this can be written as

$$R(\zeta) = \begin{cases} A + B\zeta & z \leq \delta \\ 0 & z > \delta \end{cases} \tag{234}$$

where

$$A = \frac{0.425}{1 - \zeta_0} \tag{235}$$

and

$$B = -\frac{0.425}{1 - \zeta_0} \tag{236}$$

Then $\bar{u}$ can be written as

$$\bar{u} = \cos\phi_{cw} [I_1(\zeta) - I_2(\zeta)] \tag{237}$$

where $I_1(\zeta)$ has been evaluated and is given by Equation 231. The integral $I_2(\zeta)$ is given by

$$I_2(\zeta) = \int_{\zeta_0}^{\zeta} \frac{u_{*c}^2 \cos\phi_{cw} \delta (A + B\zeta) d\zeta}{\bar{\nu}} \tag{238}$$

with A and B from Equations 235 and 236.

344. Using $\bar{\nu}$ from Equation 174, this can be evaluated analytically. The form of the solution depends on whether the level $z = \delta$ is above or below the level $z = (\delta\sqrt{2/\pi}a)/\mu$. As mentioned in the discussion following Equation 174, the theory developed so far can be considered justified so long as Equation 176 holds, i.e., $(\sqrt{2/\pi}a_1)/\mu > 1$ holds. Since $a_1 = 0.8$ has been selected for the time-varying model this reduces to $\mu < 0.64$.

345. When this condition is satisfied, the solution for $I_2(\zeta)$ can be obtained by carrying out the integration in Equation 238 and obtaining the constants by requiring a solution to be continuous across the level $z = a_1\delta$. $I_2(\zeta)$ is found to be

$$I_2(\zeta)=\begin{cases}\dfrac{u_{*c}}{\kappa}\sqrt{\dfrac{\pi}{2}}\mu\left[A\ \ln\left[\dfrac{\zeta}{\zeta_0}\right]+B(\zeta-\zeta_0)\right] & \zeta<a_1\\ \dfrac{u_{*c}}{\kappa}\sqrt{\dfrac{\pi}{2}}\mu\left[A\left(\dfrac{\zeta}{a_1}-1\right)+\dfrac{B}{2}\left[\dfrac{\zeta^2}{a_1}-a_1\right]+A\ln\left[\dfrac{a_1}{\zeta_0}\right]+B(a_1-\zeta_0)\right] & a_1<\zeta<1\\ \dfrac{u_{*c}}{\kappa}\sqrt{\dfrac{\pi}{2}}\mu\left[A\left[\ln\left[\dfrac{a_1}{\zeta_0}\right]+\dfrac{1}{a_1}-1\right]+\dfrac{B}{2}\left[a_1+\dfrac{1}{a_1}-2\zeta_0\right]\right] & \zeta>1\end{cases} \qquad (239)$$

where it has been assumed that $a_1 < 1$.

346. Therefore Equations 231 and 239 can be used to find the current velocity profile without the need of numerical integration. The solution for the conditions of Davies, Soulsby, and King (1988) using Equations 231 and 239 is compared with that obtained by numerical integration in Figure 32. Equation 239 is a very good approximation to the exact value of $I_2(\zeta)$. It has been found that the approximation is good for a large range of μ and A_b/k_b; so Equation 239 can be used with confidence in the current solution.

Summary

347. An eddy viscosity model that included time variation was considered in this Part. The assumption of a weak current relative to the waves was made in order to obtain simplified approximate equations for the wave and current motions. The wave problem was similar to the wave problem of the time-invariant model.

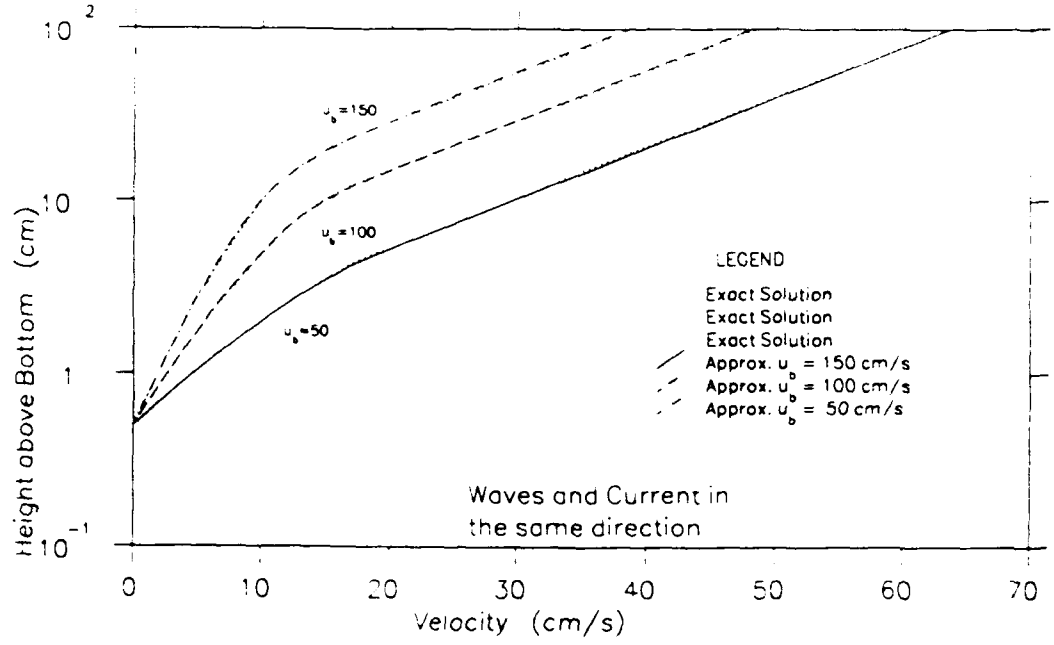

a. Comparison for waves and current in the same direction

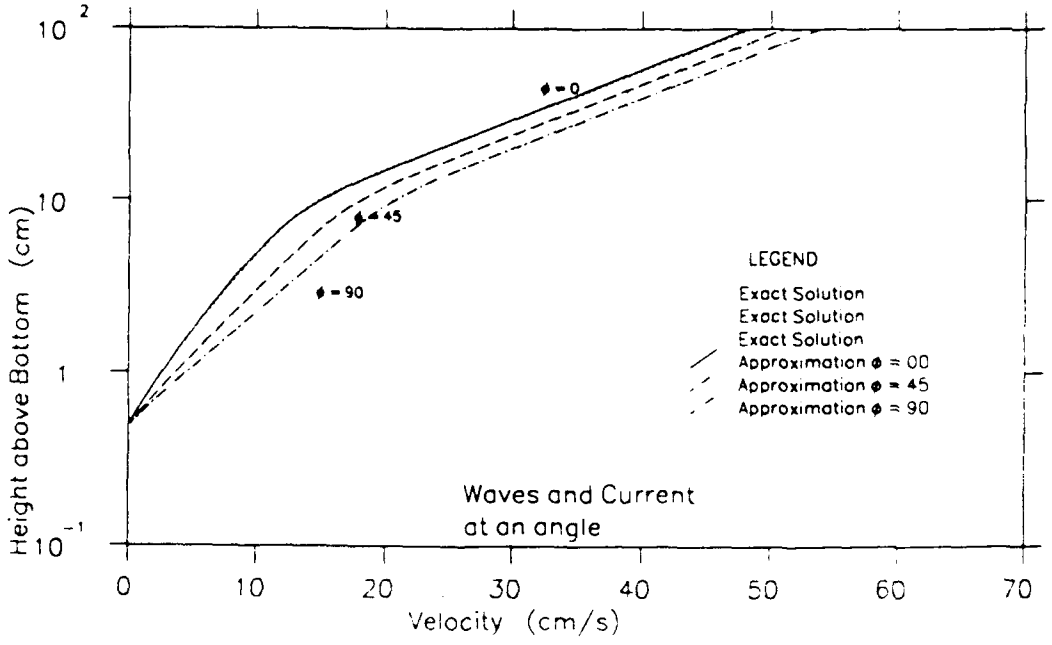

a. Comparison for waves and current at an angle

Figure 32. Current velocity profiles for the conditions of Davies, Soulsby, and King (1988) obtained from the numerical integration of Equation 224 and using the approximation given in Equation 239

348. The approximate equations for the current showed that the component of the mean velocity in the wave direction is governed by a different equation from that which governs the mean velocity in a direction normal to the wave motion. This results in a significant increase in the sensitivity of the current velocity profile to ϕ_{cw}, the angle between the waves and the current, in agreement with experimental evidence. Another feature is the variation with height of the direction of the mean velocity when $0^\circ < \phi_{cw} < 90^\circ$ —a feature that was not present in the time-invariant model but was indicated by the sophisticated numerical models.

349. However, the time-varying model is derived only for small values of μ and bases its eddy viscosity on the wave shear stress only. This results in the shear velocity used in the time-varying model, unlike the time-invariant model, being insensitive to the magnitude or the direction of the current. When μ is small, this effect is negligible, but it may be significant for stronger currents.

350. Thus, the time-varying model includes a sensitivity to ϕ_{cw} that is not present in the time-invariant model while neglecting an effect that could be important at higher values of μ. It should also be remembered that the solutions obtained are expected to be good only for $\mu < \sqrt{2/\pi}\alpha_1$.

351. These objections notwithstanding, comparisons with the experimental data indicate that the selection of $\alpha_1 = 0.8$ gives good agreement with all the data sets. The agreement for waves and the current in the same direction is as good as from the time-invariant model while the agreement for waves and the current at an angle is much better than that from the time-invariant model. A value of α_1 around 0.65 is indicated as more suitable for conditions with smaller (< 0.1) values of μ.

352. The simple analytic approximation to the integral in the current solution is very close to the numerical solution. Therefore, the time-varying model with $\alpha_1 = 0.8$ and the current solution given by Equations 231 and 239 is proposed as a simple model for the problem of a current in the presence of waves.

PART VI: MODEL SIMPLIFICATION, APPLICATION, AND EXAMPLE CALCULATIONS

353. In this Part the problem of predicting the current velocity profile in the presence of waves, using the time-varying model, will be treated in detail. The information needed to solve the problem is specified along with the equations needed for the solution. The solution for the friction factor is then simplified to an analytic form. The solution procedure is then outlined and illustrated with two example calculations.

Problem Specification

354. To apply the wave-current theory developed in Part V, it is necessary to specify the bottom roughness in terms of its equivalent Nikuradse sand grain roughness, k_n , and the wave motion in terms of its period, T , and near-bottom orbital velocity $u_b = A_b 2\pi/T$, i.e.,

$$k_n \quad , \quad \omega = 2\pi/T \quad , \quad \text{and} \quad u_b = A_b\omega \tag{240}$$

must be known.

355. The specification of the current may either be in terms of the average bottom shear stress and its direction relative to the wave motion, i.e.,

$$\tau_c = \rho u_{*c}^2 \qquad \text{and} \qquad \phi_{cw} \tag{241}$$

or in terms of the current magnitude, at a given level, $z = z_r$, assumed to be outside the wave boundary layer and its direction relative to the waves, i.e.,

$$u_c(z = z_r) \qquad \text{and} \qquad \phi_c \tag{242}$$

356. The objective is to calculate the current velocity profile outside the wave boundary layer once the conditions given above are specified. The current velocity in the outer region is given from Equations 222 and 225 as

$$u_c = \{[I_1(\zeta) - I_2(\zeta)]^2 \cos^2\phi_{cw} + I_1(\zeta)^2 \sin^2\phi_{cw}\}^{\frac{1}{2}} \tag{243}$$

357. The value of $I_1(\zeta)$ in the outer region is given by Equation 231 as

$$I_1(\zeta) = \frac{u_{*c}}{\kappa}\left[\ln\left[\frac{\zeta\mu}{a_1\sqrt{\frac{2}{\pi}}}\right] + 1 + \mu\sqrt{\frac{\pi}{2}}\left[\ln\left[\frac{a_1}{\zeta_0}\right] - 1\right]\right] \tag{244}$$

358. The integral $I_2(\zeta)$ can be approximated in the outer region by Equation 239. Using Equations 235 and 236, this can be written as

$$I_2(\zeta) = \frac{u_{*c}}{\kappa}\sqrt{\frac{\pi}{2}}\,\mu\,\frac{0.425}{1-\zeta_0}\left[\ln\left[\frac{a_1}{\zeta_0}\right] + \frac{0.5}{a_1} - \frac{a_1}{2} - 1 + \zeta_0\right] \tag{245}$$

359. The angle between the current velocity and the waves, ϕ_c, is related to ϕ_{cw} by Equation 232, i.e.,

$$\phi_c(\zeta) = \tan^{-1}\left[\frac{\tan(\phi_{cw})\ I_1(\zeta)}{I_1(\zeta) - I_2(\zeta)}\right] \tag{246}$$

360. To illustrate the procedure to obtain the various quantities that appear on the right side of Equation 244, it is convenient to restate the definitions of these quantities defined in earlier chapters. Thus,

$$\mu = \frac{u_{*c}}{u_{*1}} \tag{247}$$

gives the relative strength of the current motion to the wave motion. The wave shear velocity is related to u_b, the near bottom wave velocity, by

$$u_{*1} = \sqrt{\frac{f_{wc}}{2}}u_b \tag{248}$$

while the values δ and ζ_0 in Equation 244 are defined by

$$\delta = \frac{\kappa u_{*1}}{\omega} \tag{249}$$

$$\zeta_0 = \frac{k_n}{30\delta} \tag{250}$$

361. The problem is closed by relating f_{wc} to the parameter A_b/k_n and μ through Equation 205. Note that a_1 is no longer a free parameter but has been selected, based on the comparisons presented in Part V, to take on the value of 0.8. However, solution of Equation 205 is complicated as it involves the solution of five simultaneous complex equations and the use of Kelvin functions. Thus, apart from the determination of f_{wc}, it is seen from the equations listed above that the remainder of the problem is in a form that can be solved using no more powerful computational tools than a hand calculator. Therefore, if a simplified form of Equation 205 can be found, the application of this theory to practical problems will be significantly facilitated.

Simplified Wave Friction Factor Determination

362. As seen in Figure 25 the wave friction factor in the presence of currents is only a very weak function of μ —the parameter that gives the strength of the current relative to the waves. Thus, for practical applications it suffices to consider

$$f_{wc} = f\left[\frac{A_b}{k_n}\right] \tag{251}$$

which means that the entire closure problem effectively collapses to a single curve in the wave friction diagram.

363. It is of interest to examine how closely this curve is represented by the GM model's closure which may be obtained from Equation 71, with A given by Equation 65, and reads

$$\sqrt{f_{wc}} = \sqrt{2}\kappa \left| \frac{\ker'(2\sqrt{\zeta_0}) + i\,\mathrm{kei}'(2\sqrt{\zeta_0})}{\ker(2\sqrt{\zeta_0}) + i\,\mathrm{kei}(2\sqrt{\zeta_0})} \right| \tag{252}$$

364. The wave friction factor obtained from the GM model, Equation 252, is compared with the wave friction factor from the time-varying model with $\alpha_1 = 0.8$ and μ arbitrarily chosen to be 0.2, in Figure 33. The figure shows that the two friction factors have very similar variations with A_b/k_n with the value from the time-varying model being less by about 9 percent.

365. Using the asymptotic expressions for Kelvin function in the limit of $\zeta_0 \to 0$, given by Abramowitz and Stegun (1972), and following the development of Grant (1977), the asymptotic form of Equation 252 becomes

$$\frac{1}{4\sqrt{f_{wc}}} + \log_{10}\left[\frac{1}{4\sqrt{f_{wc}}}\right] = \log_{10}\left[\frac{A_b}{k_n}\right] - M \qquad (253)$$

with $M = 0.17$. This expression is identical to the semi-empirical wave friction factor formula obtained by Jonsson and Carlsen (1976) when M is taken as 0.08.

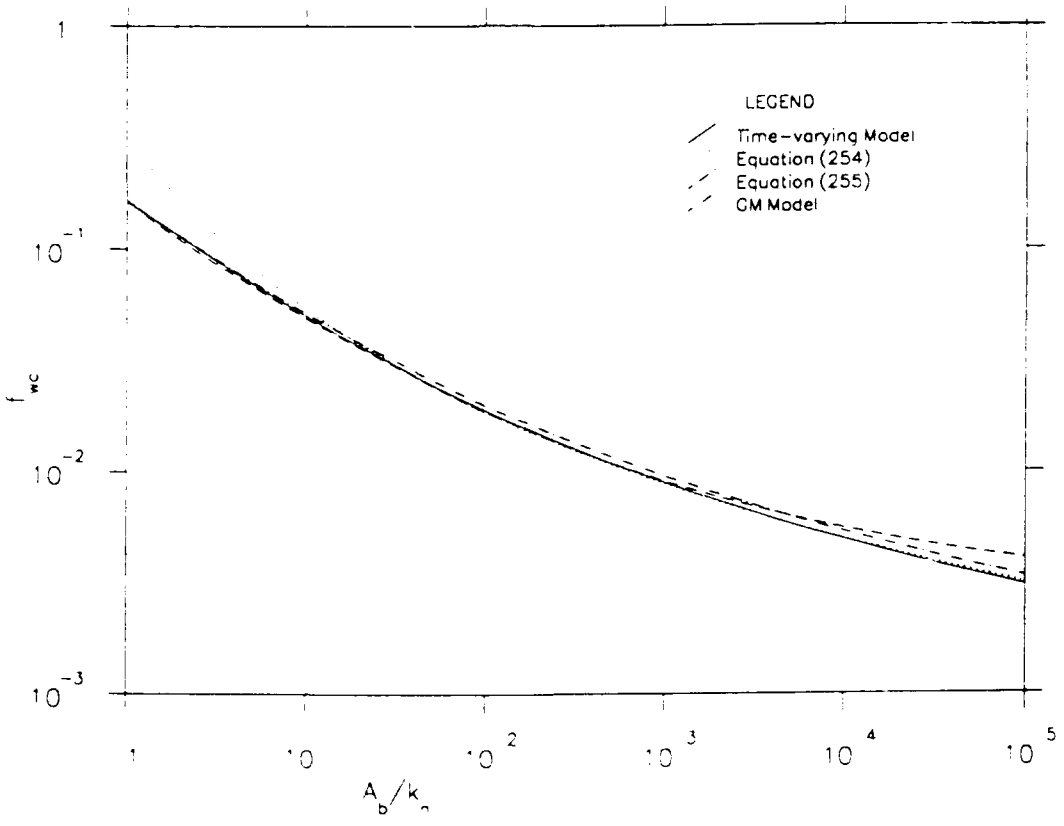

Figure 33. Wave-current friction factor from the time-varying model with $\mu = 0.2$ compared with the wave friction factor from the GM model and the approximation given by Equation 254 and 255

366. It is evident from the form of Equation 253 that the actual value of M is immaterial as A_b/k_n becomes large. Thus, rather than using the theoretical value of $M = 0.17$, a value of $M = -0.1$ in Equation 253 was found to give a better representation of the "exact" wave friction factor from the time-varying model for intermediate values while not sacrificing the accuracy for large values of A_b/k_n. For this reason, the modified friction factor may be obtained from the equation

$$\frac{1}{\sqrt{4f_{wc}}} + \log_{10}\left[\frac{1}{4\sqrt{f_{wc}}}\right] = \log_{10}\left[\frac{A_b}{k_n}\right] + 0.1 \tag{254}$$

which, for values of $A_b/k_n > 10^3$, is readily solved by iteration. The modified wave friction factors, f_{wc}, obtained from Equation 254 are compared with the exact values in Figure 33, and the agreement is seen to be excellent for values of $A_b/k_n > 1{,}000$.

367. For lower values of A_b/k_n, the accuracy of the approximation afforded by Equation 254 deteriorates. However, for the range $A_b/k_n < 1{,}000$, the modified wave friction factor may, following Swart (1974), be expressed as

$$f_{wc} = \exp\left[5.2\left[\frac{A_b}{k_n}\right]^{-0.19} - 6.1\right] - 0.24\left[\frac{A_b}{k_n}\right]^{-1.2} \tag{255}$$

which, as demonstrated in Figure 33, provides an excellent (and simple) representation of the exact formulation for $A_b/k_n < 1{,}000$.

368. Thus, the cumbersome procedure of solving five simultaneous complex equations and solving Equation 205 by iteration can, for applications, be replaced by the relatively far simpler evaluation of f_{wc} from Equation 254, for $A_b/k_n > 1{,}000$, and Equation 255, for $A_b/k_n < 1{,}000$.

Solution Procedure

369. The procedure to be followed depends on whether the current is specified by Equation 241 or by Equation 242. The procedure for each case is described in the next two sections.

Solution for a current
specified by the bottom shear stress

370. In the simplification of the wave problem described in the preceding section, the wave friction factor, f_{wc}, which was only a very weak function of the current, is assumed completely independent of the current magnitude and direction. This makes the solution straightforward. The procedure is described a step at a time:

a. Calculate the value A_b/k_n from the given wave conditions and bottom roughness.

b. Calculate f_{wc} using the appropriate equation, Equation 254 or 255.

c. Find u_{*1} using Equation 248.

d. Find μ from Equation 247 and δ from Equation 249.

371. Now all the quantities needed to evaluate the current velocity profile are known; therefore u_c and ϕ_c can be found at any height above the bottom using Equations 243-246.

Solution for the current specified
by its magnitude and direction at $z = z_r$

372. The procedure in this case is more complicated because u_{*c} and ϕ_{cw} are both unknowns to be determined as part of the solution. This requires an iterative procedure.

373. As before, the wave friction factor can be calculated first since it is independent of the current. The steps are:

a. Find A_b/k_n from the given wave properties and bottom roughness.

b. Calculate f_{wc} using the appropriate equation, Equation 254 or 255.

c. Find u_{*w}, μ, and δ from Equations 248, 247, and 249, respectively.

374. Now it can be seen that all the terms on the right side of Equations 244 and 245 are known except u_{*c}. An initial estimate for u_{*c} can be obtained by assuming that waves are not present and that the velocity is logarithmic. This leads to

$$u_{*c}^{(0)} = \frac{\kappa u_c}{\ln(z_r/z_0)} \tag{256}$$

where the superscript denotes the stage of the iteration. A good initial estimate for ϕ_{cw} is the angle between the current and the waves, i.e.,

$$\phi_{cw}^{(0)} = \phi_c \tag{257}$$

375. The next steps of the procedure are as follows:

d. Calculate values for u_c and ϕ_c, termed u_c' and ϕ_c' respectively, using Equations 243-246

e. Update the estimates of u_{*c} and ϕ_{cw} using the relations

$$u_{*c}^{(1)} = \frac{u_c}{u_c'} u_{*c}^{(0)} \tag{258}$$

$$\phi_{cw}^{(1)} = \phi_{cw}^{(0)} + (\phi_c - \phi_c') \tag{259}$$

376. Steps d and e are repeated until the values of u_c and ϕ_c converge.

Example Calculations

377. Two example calculations are presented to illustrate the procedures outlined in the preceding section, one for each method of specifying the current.

Example 1

378. The chosen wave and bottom roughness parameters are

$$u_b = 25.7 \text{ cm/sec} \quad , \quad \omega = 3.14 \text{ sec}^{-1} \quad , \quad k_n = 2.1 \text{ cm} \tag{260}$$

and the current is specified by

$$u_{*c} = 1.45 \text{ cm/sec} \quad , \quad \phi_{cw} = 0^\circ \tag{261}$$

379. From the values in Equation 260, it is found that

$$\frac{A_b}{k_n} = 3.9 \tag{262}$$

so that Equation 255 will be the appropriate equation for the wave friction factor. Use of this equation results in

$$f_{wc} = 0.077 \tag{263}$$

and from Equations 247-250, it is seen that

$$\mu = 0.28 \quad ; \quad \delta = 0.64 \text{ cm} \quad ; \quad \zeta_0 = 0.109 \tag{264}$$

380. Equation 264 along with the given value of u_{*c} can be used in Equations 243-245 to calculate the current velocity profile. The velocity at $z = 4.6$ cm is found to be 8.2 cm/sec. This shows that the solution obtained is correct because the conditions specified by Equations 260 and 261 correspond to the data set BVD10 and the value of u_{*c} given was that calculated in Part V. The current specification for the set BVD20 was $u_c = 8.2$ cm/sec at $z = 4.6$ cm, which is the same value as obtained above. If the full velocity profile is desired, it may of course be calculated from Equations 231 and 239.

Example 2

381. The chosen wave and bottom roughness parameters are

$$u_b = 100 \text{ cm/sec} \quad , \quad k_n = 15 \text{ cm} \quad , \quad \omega = 0.785 \text{ sec}^{-1} \tag{265}$$

and the current is specified by

$$u_c = 49.3 \text{ cm/sec} \quad , \quad \phi_c = 48^\circ \quad \text{at} \quad z_0 = 88.5 \text{ cm} \tag{266}$$

From Equation 265, it is seen that

$$\frac{A_b}{k_n} = 8.5 \tag{267}$$

so here too Equation 255 should be used to calculate f_{wc}. Using this equation along with Equations 247-250 results in the following parameters for the wave boundary layer

$$\delta = 8.3 \text{ cm} \quad , \quad u_{*1} = 16.3 \text{ cm/sec} \quad , \quad \zeta_0 = 0.06 \tag{268}$$

These values can be substituted in Equations 244 and 245 along with $\alpha_1 = 0.8$, $\kappa = 0.4$, and the definition of μ to express I_1 and I_2 with u_{*c} the only unknown. The equations are

$$I_1(z_r) = 2.5\, u_{*c}[\ln(1.025u_{*c}) + 0.122u_{*c} + 1] \text{ cm/sec} \quad (269)$$

$$I_2(z_r) = 0.163u_{*c}^2 \text{ cm/sec} \quad (270)$$

where u_{*c} is in cm/sec. These two expressions make steps d and e of the solution much easier to carry out. The values of u_{*c}, ϕ_{cw}, I_1, I_2, u_c', and ϕ_c' at each step of the iteration are given in Table 11. The convergence is fairly rapid.

382. The calculated value of u_{*c} is 5.92 cm/sec and $\phi_{cw} = 44.7°$, which indicate that the solution is correct because the conditions specified by Equation 265 correspond to the data set DV1045 (i.e., $u_{*c} = 5.92$ cm/sec, $\phi_{cw} = 45°$) and the specified current velocity and direction were taken from the profile generated for that data set, which is presented in Figure 30.

Table 11

Example Calculation for a Current Specified by Its Velocity and Direction at a Height $z = z_r$

Iteration Level	u_{*c} cm/s	ϕ_{cw} deg	I_1 cm/s	I_2 cm/s	u_c' cm/s	ϕ_c' deg
0	3.81	48	26.9	2.4	25.7	50.6
1	7.31	45.3	71.4	8.7	67.2	49.0
2	5.36	44.3	45.0	4.7	42.7	47.4
3	6.19	44.9	55.8	6.2	52.7	48.3
4	5.79	44.6	50.5	5.5	47.8	47.9
5	5.97	44.7	52.8	5.8	50.0	48.0
6	5.88	44.7	51.7	5.6	49.0	48.0
7	5.92	44.7	52.2	5.7	49.4	48.0

PART VII: CONCLUSIONS

383. The objective of this study was to develop a model of the interaction between the turbulent wave and current boundary layers. It was required that the model be simple enough to permit efficient analytic solutions while at the same time being able to capture the important aspects of the problem. The simple closure of the turbulence problem by an assumed eddy viscosity model was selected, and only the case of turbulent flow over a fixed, horizontal bed was considered.

384. As a first step, the development of such models for the wave and wave-current problems as given in the literature was reviewed. It was seen that many of the models proposed in the literature had not been verified by a comparison with experimental or field data. Therefore, three of the more recent models were selected and compared with experimental data from the wave and wave-current boundary layers. These models differed in the definition of the velocity scale for the eddy viscosity and in the assumed vertical structure of the eddy viscosity.

385. The comparisons indicate that the model of Grant and Madsen (1979 and 1986) is the most successful of the existing models considered in representing the available experimental data. The distinguishing features of this model are the use of the current shear velocity to scale the eddy viscosity in the outer layer, the use of the maximum shear stress to define the combined shear velocity inside the wave boundary layer, and the use of a boundary layer length scale based on the maximum shear velocity.

386. The resulting current velocity profile is logarithmic in both layers—a feature shown by the experimental data. The flow in the outer region is similar to the pure current case except that the bottom resistance is increased due to the added turbulence contributed by the wave motion within the wave boundary layer.

387. The main disadvantage of the GM model is that it uses an eddy viscosity that is discontinuous at the edge of the wave boundary layer. This formulation is not physically realistic and leads to a poor representation of the current velocity profile in the transition region between the wave boundary layer and the current boundary layer.

388. The improved model discussed in Part IV attempts to remove this drawback by using a more complicated but more realistic continuous vertical

structure of the eddy viscosity. This results in a somewhat more complex solution procedure. However, it should be noted that the model still involves only one free parameter, as does the GM model. Therefore, the fact that this model gives better agreement with the data than the GM model can be attributed entirely to the more realistic eddy viscosity formulation and not to the use of more model parameters.

389. Two different values of the free model parameter were suggested from the comparisons with the wave and wave-current experimental data. A single value ($\alpha = 0.5$) was selected as a reasonable compromise on the grounds that it gives a good representation of the current velocity profiles while not being seriously in error for the wave boundary layer.

390. The rather complicated solution of the wave problem in this model was simplified by the introduction of the modified friction factor and excursion amplitude defined in Part IV.

391. While the improved model gave excellent results for a current velocity profile with waves in the same direction, it could not adequately represent the effect of a change in the angle between the waves and the current. The deflection of the current velocity away from the direction of the mean shear stress, which was a feature of sophisticated numerical models, was also not represented by the time-invariant model.

392. These drawbacks were a result of the eddy viscosity being assumed time invariant. Therefore, a model that included time variation of the eddy viscosity was developed in Part V. The assumption of a weak current relative to the waves (small μ) was made to obtain tractable approximate governing equation for the waves and for the current. The equations thus derived for the current included an explicit dependence on the angle between the waves and the current, in contrast to the time-invariant models.

393. While the time-varying model involved much more algebra than before, the final solution for the wave problem was shown to be very similar to that from the time-invariant model. After comparison with the experimental data, the value of the free model parameter was chosen to be $\alpha_1 = 0.8$. This value provided good agreement even with data sets where the value of μ was not very small. The solution of the current problem involved numerical integration, but a simple, accurate, analytic approximation was developed that made this unnecessary. The result was a

model that allowed an analytic evaluation of the current velocity profile just as in the time-invariant model. However, as shown in Figure 30, this model is much more sensitive to the angle between the waves and the current than previous models. Therefore, this model is presented as a simple but realistic model for the problem of a current in the presence of waves.

394. The similarity of the wave friction factor diagrams from the time-varying and GM models was used in Part VI to develop analytic approximations to the friction factor, thereby avoiding the use of Kelvin function and the solution of complex simultaneous equations. A procedure was outlined whereby practical problems could be solved efficiently using a no more powerful tool than a hand calculator. This procedure can also be incorporated with ease into a computer program.

REFERENCES

Abramowitz, M., and A. Stegun, I. A., eds. 1972. Handbook of Mathematical Functions, Dover, NY.

Asano, T., and Iwagaki, Y. 1986. "Non-Linear Effects on Velocity Fields in Turbulent Wave Boundary Layer," Coastal Engineering in Japan, Vol 29, pp 51-63.

Bakker, W. T. 1974. "Sand Concentration in an Oscillatory Flow," Proceedings of the 14th International Conference on Coastal Engineering, pp 1129-1148.

Bakker, W. T., and van Doorn, T. 1978. "Near-Bottom Velocities in Waves with a Current," Proceedings of the 16th International Conference on Coastal Engineering, pp 1394-1413.

Brevik, I. 1981. "Oscillatory Rough Turbulent Boundary Layers," Journal of the Waterways, Harbors and Coastal Engineering Division, American Society of Civil Engineers, Vol 107, No. WW3, pp 175-188.

Celik, I., and Rodi, W. 1985. "Calculation of Wave-Induced Turbulent Flows in Estuaries," Ocean Engineering, Vol 12, No. 6, pp 531-542.

Christoffersen, J. B., and Jonsson, I. G. 1985. "Bed Friction and Dissipation in a Combined Current and Wave Motion," Ocean Engineering, Vol 12, No. 5, pp 387-423.

Davies, A. G., Soulsby, R. L., and King, H. L.. 1988. "A Numerical Model of the Combined Wave and Current Bottom Boundary Layer," Journal of Geophysical Research, Vol 93, No. C1, pp 491-508.

Grant, W. D. 1977. "Bottom Friction Under Waves in the Presence of a Weak Current: Its Relationship to Coastal Sediment Transport," Sc.D. Dissertation, Massachusetts Institute of Technology, Cambridge, MA.

Grant, W. D., and Madsen, O. S. 1979. "Combined Wave and Current Interaction with a Rough Bottom," Journal of Geophysical Research, Vol 84, No. C4, pp 1797-1808.

_____. 1982. "Movable Bed Roughness in Oscillatory Flow," Journal of Geophysical Research, Vol. 87, No. C1, pp 469-481.

_____. 1986. "The Continental-Shelf Bottom Layer," Annual Review of Fluid Mechanics, Vol 18, pp 265-305.

Hagatun, K., and Eidsvik, K. J. 1986. "Oscillating Turbulent Boundary Layers with a Suspended Sediment," Journal of Geophysical Research, Vol 91, No. C11, pp 13045-13055.

Hildebrand, F. B. 1976. Advanced Calculus for Applications, 2d ed., Prentice-Hall, Englewood Cliffs, NJ.

Ippen, A. T., ed. 1966. Estuary and Coastline Hydrodynamics, McGraw-Hill, New York.

Jonsson, I. G. 1963. "Measurements in the Turbulent Wave Boundary Layer," International Association for Hydraulic Research Congress, London, Vol 1, pp 85-92.

_____. 1966. "Wave Boundary Layers and Friction Factors," Proceedings of the 7th Conference on Coastal Engineering, pp 127-148.

Jonsson, I. G., and Carlsen, N. A. 1976. "Experimental and Theoretical Investigation in an Oscillatory Turbulent Boundary Layer," Journal of Hydraulic Research, Vol 14, No. 1, pp 45-60.

Justesen, P. 1988. "Turbulent Wave Boundary Layers," Series Paper No. 43, Technical University of Denmark, Lyngby, Denmark.

Kajiura, K. 1964. "On the Bottom Friction in an Oscillatory Current," Bulletin of the Earthquake Research Institute, Vol 42, pp 147-174.

_____. 1968. "A Model of the Bottom Boundary Layer in Water Waves," Bulletin of the Earthquake Research Institute, Vol 46, pp 75-123.

Lundgren, H. 1972. "Turbulent Currents in the Presence of Waves," Proceedings of the 13th International Conference on Coastal Engineering, pp 623-634.

Lyne, W. H. 1971. "Unsteady Viscous Flow over a Wavy Wall," Journal of Fluid Mechanics, Vol 50, No. 1, pp 33-48.

Nikuradse, J. 1932. "Gesetzmässigkeiten der turbulenten StrÖmung in glatten RÖhren," VDI-Forschungsheft, No. 356.

Sato, S., Mimura, N., and Watanabe, A.. 1984. "Oscillatory Boundary Layer Flow over Rippled Beds," Proceedings of the 19th International Conference on Coastal Engineering, pp 2293-2309.

Sato, S., Uehara, H., and Watanabe, A. 1986. "Numerical Simulation of the Oscillatory Boundary Layer Flow over Ripples by a k-ϵ Turbulence Model," Coastal Engineering in Japan, Vol 29, pp 65-78.

Schlichting, H. 1968. Boundary Layer Theory, 6th ed., McGraw-Hill, New York, NY.

Shum, K. T. 1988. "A Numerical Study of Vortex Dynamics and Rigid Ripples," Sc.D. Dissertation, Massachusetts Institute of Technology, Cambridge, MA.

Sleath, J. F. A. 1974. "Velocities Above Rough Bed in Oscillatory Flow," Journal of the Waterways, Harbors and Coastal Engineering Division, American Society of Civil Engineers, Vol 100, No. WW4, pp 287-304.

_____. 1976. "Forces on a Rough Bed in Oscillatory Flow," Journal of Hydraulic Research, Vol 1, No. 1, pp 33-47.

Sleath, J. F. A. 1982. "Friction Coefficients of Rippled Beds in Oscillatory Flow," Continental Shelf Research, Vol 1, No. 1, pp 33-47.

Smith, J. D. 1977. "Modelling of Sediment Transport on Continental Shelves," In: The Sea, Vol 6, Interscience, New York, pp 538-577.

Swart, D. H. 1974. "Offshore Sediment Transport and Equilibrium Beach Profiles," Ph.D. Thesis, Delft University of Technology, Delft, The Netherlands.

Tanaka, H., Chian, C. S., and Shuto, N. 1983. "Experiments on an Oscillatory Flow Accompanied with a Unidirectional Motion," Coastal Engineering in Japan, Vol 26, pp 19-37.

Tanaka, H., and Shuto, N. 1981. "Friction Coefficient for a Wave-Current Coexisting System," Coastal Engineering in Japan, Vol 24, pp 105-128.

Trowbridge, J., and Madsen, O. S. 1984a. "Turbulent Wave Boundary Layers, 1: Model Formulation and First-Order Solution," Journal of Geophysical Research, Vol 89, No. C5, pp 7989-7997.

_____. 1984b. "Turbulent Wave Boundary Layers, 2: Second-Order Theory and Mass Transport," Journal of Geophysical Research, Vol 89, No. C5, pp 7999-8007.

Van Doorn, Th. 1981. "Experimental Investigation of Near-bottom Velocities in Water Waves With and Without a Current," Report No. M1423 Delft Hydraulics Laboratory, Delft, The Netherlands.

van Kesteren, W. G. M., and Bakker, W. T. 1984. "Near Bottom Velocities in Waves with a Current: Analytical and Numerical Computations," Proceedings of the 19th International Conference on Coastal Engineering, pp 1161-1177.

Wiberg, P, and Smith, J. D. 1983. "A Comparison of Field Data and Theoretical Models for Wave-Current Interactions at the Bed on the Continental Shelf," Continental Shelf Research, Vol 2, Nos. 2/3, pp 147-162.

APPENDIX A: NOTATION

A	complex constant
A_b	excursion amplitude
A_b'	modified excursion amplitude
B	complex constant
c	wave celerity
C	complex constant
d	boundary layer thickness in TS model in Part III
D	complex constant
E	complex constant
f_w	wave friction factor
f_{wc}	wave friction factor in the presence of currents
f_{wc}'	modified wave friction factor
F	complex constant
g	acceleration due to gravity
h	flow depth
i	$\sqrt{-1}$
$I_1(z)$	integral in solution for current velocity profile in time-varying model
$I_1(z)$	integral in solution for current velocity profile in time-varying model
k	wave number
k_b	physical scale of bottom roughness
k_n	equivalent Nikuradse roughness
K'	parameter in TS model in Part III
l	mixing length
l	height of boundary layer in GM and SM models in Part III
L	length scale
p	pressure
p_w	pressure due to wave motion
p_c	pressure due to current motion
p_∞	pressure just outside wave boundary layer
P	constant in the time-varying model Equation 206
Q	constant in the time-varying model Equation 211
$R(z)$	ratio of $I_2(z)$ to $I_1(z)$

s parameter in TS model in Part III $s = d/z_h$

t time

$\tilde{t}$ transformed time variable Equation 182

u horizontal velocity in wave direction

u_b magnitude of near-bottom wave velocity

u_c current (mean) velocity

u_d complex nondimensional wave deficit velocity

$\tilde{u}_d$ complex nondimensional wave deficit velocity in time-varying model

u_{d1} component of $\tilde{u}_d$

u_{d2} component of $\tilde{u}_d$

u_{d3} component of $\tilde{u}_d$

u_w wave velocity

u_{w1} first harmonic wave velocity in time-varying model

u_{w2} third harmonic wave velocity in time-varying model

u' turbulent velocity fluctuation about the mean

u_* shear velocity

u_{*c} current shear velocity

u_{*cw} combined wave-current shear velocity

u_{*m} shear velocity based on maximum shear stress

u_{*w} wave shear velocity

u_{*1} shear velocity due to first harmonic wave shear stress in time-varying model

U velocity scale

$U'(z)$ nondimensional gradient of u_{d1} Equation 217

V horizontal velocity in direction normal to wave direction

w vertical velocity

w' turbulent fluctuation in vertical velocity

x horizontal coordinate in wave direction

y horizontal coordinate in direction normal to waves

z vertical coordinate

z_h flow depth

z_r reference level at which current is specified

z_0 bottom roughness parameter $z_0 = k_n/30$

a free parameter in improved time-invariant model

a_1 free parameter in time-varying model

β parameter in TS model $\beta = d/\delta$

γ free parameter in GM and SM models in Part III

γ argument of $\partial u_{d1}/\partial z$ at $z = z_0$ in time-varying model

δ boundary layer length scale

ϵ ratio of current shear velocity to combined shear velocity

ζ nondimensional vertical coordinate $\zeta = z/\delta$

ζ_h nondimensional flow depth

θ phase of bottom shear stress $\theta = \omega t + \phi_2$

κ Van Karman's constant $\kappa = 0.4$

μ ratio of current shear velocity to wave shear velocity

ν molecular viscosity

ν_t turbulent eddy viscosity

ρ density

τ shear stress

τ_{ij} shear stress in direction j on plane normal to direction i

τ_b bottom shear stress

τ_{bm} maximum bottom shear stress

τ_c bottom shear stress due to current

τ_w bottom shear stress due to waves

ϕ_c angle made by current velocity vector with wave direction

ϕ_{cw} angle between waves and the current

ϕ_2 phase of first harmonic bottom shear stress

ϕ_3 phase of third harmonic bottom shear stress

ω angular frequency

Re real part of a complex number

$| \; |$ modulus of a complex number

∇ horizontal gradient operator

Superscripts

- mean value of a quantity

$\rightarrow$ vector quantity

(0), (1) levels of iteration in the solution procedure of Part VI

$\sim$ time-varying portion of a quantity

Subscripts

c	concerned with the current motion
e	even harmonics of a time-varying quantity
o	even harmonics of a time-varying quantity
w	concerned with the wave motion